Advancing the Capabilities of Rapid Acquisition with Relaxation Enhancement Magnetic Resonance Imaging: Development of Novel Methodology and *in-vivo* Applications

DISSERTATION

zur Erlangung des akademischen Grades

doctor rerum naturalium

(Dr. rer. nat.)

im Fach Physik

eingereicht an der

Mathematisch-Naturwissenschaftlichen Fakultät

der Humboldt-Universität zu Berlin

von

Dipl.-Phys. Katharina Paul, geb. Fuchs

Präsident der Humboldt Universität zu Berlin

Prof. Dr. Jan-Hendrik Olbertz

Dekan der Mathematisch-Naturwissenschaftlichen Fakultät

Prof. Dr. Elmar Kulke

Gutachter/innen: 1. Prof. Dr. Thoralf Niendorf

2. Prof. Dr. Beate Röder

3. Prof. Dr. Martin Falcke

Tag der mündlichen Prüfung: 24.11.2015

Zusammenfassung

Die vorliegende Arbeit präsentiert neuartige schnelle Bildgebungstechniken für die Hoch- und Ultrahochfeld Magnetresonanztomographie (MRT) und demonstriert deren Vorteile gegenüber klinisch etablierten Techniken. Methodische Erkenntnisse und eine wachsende Anzahl neuer Anwendungsgebiete bilden die klinisch und physikalisch begründete Motivation für die Weiterentwicklung schneller Spin-Echo Techniken. Zunächst beleuchtet die vorliegende Arbeit die Grundprinzipien schneller Spin-Echo Techniken. Im Mittelpunkt steht dabei die Physik der Entstehung des Messsignals. Diese physikalischen Überlegungen bilden die Grundlage für die Entwicklung modifizierter Techniken. In einer ersten Entwicklungsstufe wird eine neue Variante der schnellen Spin-Echo Bildgebung vorgestellt. Diese Technik generiert anatomischen und funktionellen Bildkontrast innerhalb von nur einer Datenaufnahme. Dies gelang bisher lediglich in sequentiellen Bildaufnahmen. Der entscheidende Vorteil des entwickelten Ansatzes besteht in einer wesentlichen Verkürzung der Messzeit. Darüber hinaus wird eine deutliche Reduktion von Bildfehlern ermöglicht, die im konventionellen Fall häufig durch Bewegung erzeugt werden. Die Methodik des neuen Ansatzes wird erläutert und in Phantomexperimenten validiert. Eine Machbarkeitsstudie demonstriert die Vorteile der neuen Variante für die Hirnbildgebung in gesunden Probanden und Multiple Sklerose Patienten. Die zweite Entwicklungsstufe befasst sich mit der Implementierung einer schnellen Spin-Echo Technik zur Abbildung des physikalischen Phänomens der Brownschen Molekularbewegung. Dieses wird in der MRT genutzt um den funktionellen Kontrast der Diffusionswichtung zu erzeugen. Allerdings sind Diffusionsmessungen der Molekülbewegungen von nur wenigen Mikrometern durch die Überlagerung von makroskopischen Bewegungen sehr anspruchsvoll. Diese Schwierigkeit wird in der vorliegenden Arbeit methodisch überwunden, indem eine diffusionsgewichtete schnelle Spin Echo Technik implementiert wird. Die Möglichkeit damit verzerrungsfreie diffusionsgewichtete Bilder zu erzeugen wird in Phantomstudien demonstriert. Dieser methodische Vorteil wird für hochaufgelöste Bildgebung der Augen in gesunden Probanden und Patienten mit Aderhautmelanomen eingesetzt. Die dritte Entwicklungsstufe konzentriert sich auf suszeptibiltätsgewichtete schnelle Spin-Echo Bildgebung. Aus biophysikalischer Sicht ermöglichen Unterschiede in der magnetischen Suszeptibiltät Einsichten in die Gewebemikrostruktur. Herkömmliche Techniken zur suszeptibiltätsgewichteten Bildgebung sind insbesondere bei hohen Magnetfeldstärken anfällig für Artefakte, die sich in Bildverzerrungen oder in Signalauslöschungen äußern. Um dieser Herausforderung methodisch zu begegnen, untersucht diese Arbeit das Potential einer suszeptibiltätsgewichteten schnellen Spin-Echo Technik zur Charakterisierung der Mikrostruktur des Herzmuskels bei 7.0 T. Ein Ziel der in dieser Arbeit neu entwickelten schnellen Spin-Echo Methoden besteht darin, Limitierungen bestehender Techniken zu beheben. Somit kann einer Bandbreite klinischer Fragestellungen begegnet werden. Die entwickelten methodischen Neuerungen werden in Phantomstudien validiert und charakterisiert, in Probandenstudien auf ihre *in-vivo* Machbarkeit überprüft und in Pilotstudien in Patienten eingesetzt. Somit soll richtungsweisend über die Grundlagenforschung hinaus die Basis für klinische Anwendungen der entwickelten physikalischen Erkenntnisse und Methoden gelegt werden.

Abstract

This thesis presents novel fast imaging techniques for high and ultrahigh field magnetic resonance imaging (MRI) and demonstrates the advantages over conventional techniques. Rapid imaging techniques are based upon two basic principles: gradient echo and spin echo techniques. Rapid Acquisition with Relaxation Enhancement (RARE) is a variant of the latter one. An ever growing number of clinical applications along with the capabilities of novel MRI hardware render clinically and physically motivated advancement of RARE imaging necessary. To respond to this need this thesis focuses on the advancement of RARE imaging. For this purpose, the basic principle and the details of RARE imaging are introduced and examined. The generation of the measurement signal and underlying physical concepts are in the focus of these considerations and form the foundation for the development of novel RARE variants. The first part of this thesis proposes a novel RARE variant which provides simultaneous anatomical and functional contrast within one acquisition. This approach provides an alternative versus conventional RARE variants where sequential acquisitions are put to use to achieve different image contrasts. With the speed gain of the proposed approach a substantial shortening of scanning time can be accomplished together with a reduction in the propensity for motion. The underlying concept of the novel variant is introduced and validated in phantom experiments. A feasibility study in healthy volunteers and multiple sclerosis patients demonstrates the advantages of the novel variant over conventional techniques. The second part of this thesis focuses on diffusion-weighted MRI. For this purpose the physical phenomenon of Brownian motion is used. Probing diffusion on a micrometer scale is challenging because of MRI's sensitivity to bulk motion on the macro-scale. Hence, rapid imaging technology is required. Unfortunately, conventional rapid diffusion-weighted imaging techniques are prone to severe image distortions, which are pronounced at (ultra)high magnetic field strengths. Realizing this constraint, a diffusion-weighted RARE technique that affords the generation of diffusion-weighted images free of distortion is implemented. This advantage is demonstrated in phantom experiments including signal-to-noise ratio and point spread function evaluation. The methodological benefit is exploited for high spatial resolution imaging of the eyes in healthy volunteers and in patients with ocular diseases at 3.0 T and at 7.0 T. The third part of this thesis is formed around susceptibility weighted MRI. Susceptibility-weighted MRI provides functional contrast based upon magnetic susceptibility. The underlying biophysical mechanisms allow the assessment of tissue microstructure. Common susceptibility-weighted imaging techniques are prone to image artifacts which are pronounced at (ultra)high magnetic field strengths. Recognizing the challenges and opportunities of susceptibility-weighted MRI the potential of a susceptibility-weighted RARE technique is investigated with the goal to assess myocardial microstructure. The goal of the novel RARE developments introduced in this thesis is to overcome constraints of existing imaging techniques. Phantom studies characterize and validate the methodological improvements. Feasibility studies in healthy volunteers and pilot studies in patients demonstrate the *in-vivo* applicability. Consequently, the physical considerations and the novel methodology introduced in this thesis are brought beyond the scope of basic research. Moreover, the foundation for clinical applicability is created.

Index

List of Abbreviations

AC-PC	anterior commissure - posterior commissure
ACT	acoustic cardiac triggering
ADC	apparent diffusion coefficient
AFP	adiabatic full passage
AHP	adiabatic half passage
AMI	acute myocardial infarction
$\overrightarrow{B_0}$	static magnetic flux density
BIR	B_1-insensitive rotation
BMI	body mass index
BW	bandwidth
CMR	cardiovascular magnetic resonance
CPMG	Carr-Purcell-Meiboom-Gill
DIR	double inversion recovery
DMSO	dimethyl sulfoxide
DTI	diffusion tensor imaging
DWI	diffusion-weighted imaging
E	energy
ECG	electrocardiogram
EPG	extended phase graph
EPI	echo planar imaging
ESP	echo spacing
ETL	echo train length
FAISE	fast acquisition interleaved spin echo
fatSat	fat saturation
FID	free induction decay
FLARE	fast low angle refocused echo imaging
FLASH	fast low-angle shot
FSE	fast spin echo
FT	Fourier transform
FWHM	full width at half maximum
γ	gyromagnetic ratio
G	magnetic field gradient
GRE	gradient echo
$\overrightarrow{H_0}$	static magnetic field
h	Planck's constant
HCM	hypertrophic cardiomyopathy
H&E	hematoxylin and eosin
HS	hyperbolic secant

HSn	flattened hyperbolic pulse with nonlinearity factor n
$\vec{J}$	total angular momentum
j	total quantum number
k	spatial frequency
k_B	Boltzmann constant
$\vec{L}$	orbital angular momentum
l	orbital quantum number
$\vec{\mu}$	magnetic moment
$\overrightarrow{M_0}$	net magnetization
ME-GRE	multi echo gradient echo
MHD	magneto hydrodynamic
MPRAGE	magnetization prepared rapid gradient echo
MRI	magnetic resonance imaging
MS	multiple sclerosis
N_0	energy state occupied by spins aligned parallel to the external magnetic field
N_1	energy state occupied by spins aligned parallel to the external magnetic field
NMR	nuclear magnetic resonance
$\overrightarrow{\rho_0}$	spin density
PC	phase correction
PD	proton density
PINS	power independent of number of slices
POX	pulse oximetry
PSF	point spread function
pTX	parallel transmission
QSM	quantitative susceptibility mapping
RARE	rapid acquisition with relaxation enhancement
RF	radio frequency
RFPA	radio frequency power amplifier
rs-EPI	readout segmented echo planar imaging
$\vec{S}$	spin angular momentum
s	spin quantum number
SAR	specific absorption rate
SE	spin echo
SNR	signal-to-noise ratio
SPAIR	spectral adiabatic inversion recovery
SPLICE	split acquisition of fast spin echo signals
ss-EPI	single shot echo planar imaging
SSGR	slice selection gradient reversal
STA	small tip angle approximation
STE	stimulated echo
STIR	short tau inversion recovery

SWI	susceptibility weighted imaging
T	temperature
T_1	longitudinal relaxation time constant
T_2	transversal relaxation time constant
T_2^*	effective transversal relaxation time constant including magnetic field inhomogeneities and susceptibility effects
TE	echo time
TI	inversion time
TIR	triple inversion recovery
TR	repetition time
TRSE	twice refocused spin echo
TSE	turbo spin echo
UFLARE	ultra-fast low angle RARE
UHF	ultrahigh field
V	volume
$\overrightarrow{\omega_0}$	Larmor frequency
$\hat{x}, \hat{y}, \hat{z}$	unit vectors
Δz	slice thickness

1. Introduction

Imaging speed, high spatial resolution and artifact free images with diagnostic quality are of paramount relevance for medical magnetic resonance imaging (MRI). Although MRI is an established diagnostic imaging modality, advances in technology and imaging methodology are essential to meet the needs of an ever growing number of clinical indications. Innovations and developments are driven by putting the physics of magnetic resonance to good use along with explorations into biomedical engineering. These developments include novel hardware but also imaging methodology with a particular focus on rapid imaging techniques. Since the advent of MRI as a diagnostic imaging modality numerous fast imaging techniques have evolved [MANSFIELD1977b, HAASE1986, HENNIG1986].

Rapid MRI techniques comprise two main categories including gradient echo and spin echo based techniques. The latter approach – designated as Rapid Acquisition with Relaxation Enhancement (RARE) imaging [HENNIG1986] – is the focus of the developments outlined in this thesis. RARE imaging is proven to be fast, insensitive to static magnetic field inhomogeneities and provides high signal intensity. Notwithstanding this progress, the ever growing range of (bio)medical imaging constitutes the need for advancing the MR physics and (pre)clinical applications of RARE imaging. Based on this motivation, this thesis first introduces the basic principle and the generation of the measuring signal of RARE pulse sequences. The physical background is the main focus of this analysis and provides the foundation for the development of novel RARE imaging methodology.

A novel RARE variant is developed with the goal to afford the simultaneous measurement of an anatomical and a functional contrast and is presented in chapter 3. The methodology and underlying principle of the novel RARE variant is introduced and validated in phantom experiments. The feasibility for brain imaging is demonstrated in healthy subjects and in patients with multiple sclerosis with the goal to bridge the gap between basic research and clinical applicability. The *in-vivo* results underline the possibility to simultaneously generate anatomical and functional contrast which could so far only be realized using sequential acquisitions. Consequently, the novel approach implicates a substantial reduction in measurement time and decreases the propensity to motion artifacts when using conventional approaches.

Brownian motion and restricted water diffusion in tissue are (bio-)physical phenomena that can be put to good use to generate functional contrast in MR imaging. Measuring diffusion – taking place on a micrometer scale – is however prone to artifacts due to bulk motion on the macro-scale.

Hence, rapid imaging technology is required. Unfortunately, with existing methodology geometric distortions impair anatomical integrity of the images and diminish image quality with increased propensity at (ultra)high magnetic field strengths. To address this limitation a diffusion-sensitized RARE variant is implemented in this thesis with the goal to generate distortion free diffusion-weighted images at high and ultrahigh magnetic field strengths. Chapter 4 presents a comparison of the novel variant with existing imaging techniques including phantom studies and feasibility studies in healthy volunteers at high and ultrahigh magnetic field strengths ($B_0 \geq 3.0$ T). The proposed methodology is put to good use to obtain high spatial resolution diffusion-weighted *in-vivo* images of the eye. The technical innovation is applied in a pilot study in patients with uveal melanoma and retinal detachment to prove clinical feasibility. For further validation the *in-vivo* results are compared to *ex-vivo* MR microscopy and histological data.

Anatomical cardiac RARE imaging is transferred from clinically established magnetic field strengths to 7.0 T in chapter 5. This transfer is enabled by sophisticated multi-channel radiofrequency coil technology. Explorations into fat suppression and blood suppression techniques are undertaken with the goal to improve image quality. The feasibility of cardiac RARE imaging at ultrahigh magnetic field strengths is demonstrated in healthy volunteers and in a pilot study including patients with hypertrophic cardiomyopathy. Susceptibility weighting is a further functional contrast in MRI; its biophysical mechanism is considered to provide means for the assessment of tissue microstructure. It is conceptually appealing to pursue susceptibility weighted imaging at ultrahigh magnetic field strengths since magnetic susceptibility increases with magnetic field strength. State-of-the-art susceptibility weighted imaging techniques are prone to image artifacts due to increased macroscopic magnetic field inhomogeneities at ultrahigh magnetic field strengths. Unlike conventional gradient echo based susceptibility weighted techniques, RARE offers immunity to macroscopic magnetic field inhomogeneities. This methodological benefit is exploited in this thesis. The potential of a susceptibility-weighted RARE variant for the characterization of myocardial microstructure is explored.

The range of clinical applications, anatomic target regions and magnetic field strengths explored in this thesis is driven by the motivation of advancing the capabilities of RARE imaging. This driving force plays the central starting point for developing novel methodology throughout this thesis. The benefits and potential of the novel RARE variants are outlined. The clinical applicability is discussed with the goal to bridge the gap between development and practice as well as between basic research and clinical routine. The merits and limits of the proposed RARE variants are discussed together with opportunities for further improvements. A final chapter provides a glance at future directions.

2. Basic Principles of Magnetic Resonance

2.1 Nuclear Magnetic Resonance

Nuclear magnetic resonance (NMR) exploits the effect of an external magnetic field $\overrightarrow{B_0}$ on the intrinsic angular momentum (spin) of NMR active nuclei. The fundamental research building the starting point for the broad propagation of NMR commenced in the 1920's and found a rewarding peak with the award of the Nobel prize in physics for Bloch and Purcell in 1952 [GERLACH1924, RABI1938, BLOCH1946a, PURCELL1946].

The NMR concept is briefly introduced in the following sections. Its translation into magnetic resonance imaging is described to set up the basis for this thesis. The content of this chapter was compiled with the assistance of the textbooks [HAACKE1999] and [CALLAGHAN1993].

2.1.1 Behaviour of spins in an external magnetic field

NMR active nuclei possess an intrinsic angular momentum $\vec{J}$ which is equivalent to the description of nuclei having a spin unequal to zero. The angular momentum is directly proportional to the magnetic moment $\vec{\mu}$:

$$\vec{\mu} = \gamma \vec{J} \qquad [1]$$

The gyromagnetic ratio γ is the proportionality constant and is characteristic for specific nuclei. Examples for NMR active nuclei are given in Table 1.

An external magnetic field $\overrightarrow{B_0}$ will induces a precession of the spin within this magnetic field with a specific frequency according to

$$\frac{d\overrightarrow{\mu}}{dt} = \gamma \overrightarrow{\mu} \times \overrightarrow{B_{0.}} \qquad [2]$$

This equation will be further examined in section 2.1.2 when relaxation processes are considered.

Table 1: **Selected NMR active nuclei**
Five different isotopes are listed together with selected characteristics [HAACKE1999].

Isotope	Spin	γ [10^8 rad $s^{-1}T^{-1}$]	Natural abundance [%]	Resonance frequency at 3.0 T [MHz]	Resonance frequency at 7.0 T [MHz]
Hydrogen ^{1}H	1/2	2.675	99.98	127.7	298.0
Fluorine ^{19}F	1/2	2.518	100	120.2	280.5
Sodium ^{23}Na	3/2	0.707	100	33.8	78.8
Phosphorus ^{31}P	1/2	1.084	100	51.8	120.8

The quantum mechanical description of the NMR phenomenon reveals the discrete behaviour of the angular momentum. With $\overrightarrow{B_0} = (0,0,B_z)$, the z component of the angular momentum $\vec{J}$ exhibits (2I+1) possible orientations in the external magnetic field. These are

$$J_z = m_j \hbar = m_j \frac{h}{2\pi} \quad [3]$$

with h being the Plancks's constant and

$$m_j = -j, -j+1, \dots, j-1, j \quad [4]$$

where the quantum number $j = (l + s)$ is a positive integer or half-integer. The relationship

$$J^2 = j(j+1)\hbar^2 \quad [5]$$

is reduced to

$$S^2 = s(s+1)\hbar^2 \quad [6]$$

for the case that the orbital contribution $\vec{L}$ to $\vec{J}$ is neglected $(l = 0)$ and only contributions $\vec{S}$ from the intrinsic spin (s) are considered.

For the example of a hydrogen nucleus with $s = \frac{1}{2}$, two possible orientations in an external magnetic field are possible with $m_s = \pm\frac{1}{2}$.

As a consequence, discrete energy levels are observed (Figure 1):

$$E = -\vec{\mu} \cdot \vec{B} = -\mu_z B_z = -\gamma m_s \hbar B_z \qquad [7]$$

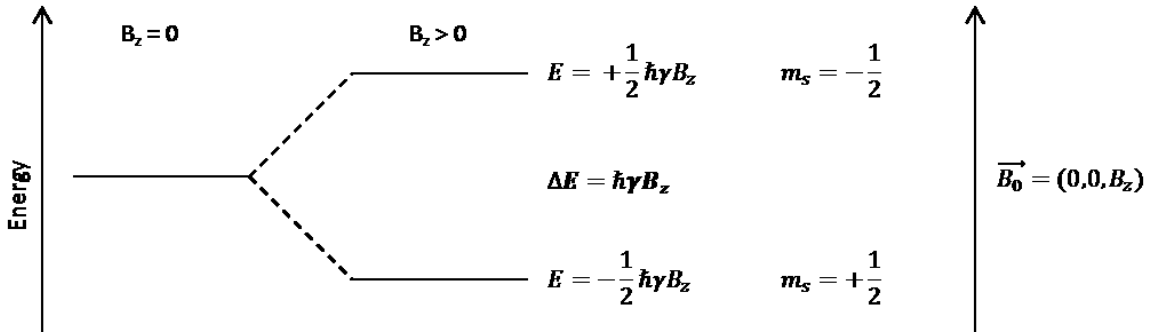

Figure 1: **Energy level diagram for spin ½ nuclei**
The energy states assigned by a spin ½ nucleus, e.g. hydrogen, are depicted without and with the impact of an external magnetic field in the specified *z* direction. Figure adapted from [HAACKE1999] (Chapter 5).

The difference in energy between these two states is directly linked to a characteristic frequency for transitions between these two states:

$$\Delta E = \frac{1}{2}\hbar\gamma B_z - \left(-\frac{1}{2}\hbar\gamma B_z\right) = \hbar\gamma B_z = \hbar\omega \qquad [8]$$

A more general and common formulation of this relationship is

$$\omega_0 = \gamma B_0. \qquad [9]$$

The Larmor frequency ω_0 belonging to the transition between the lower and the upper energy state in the picture above is also the precession frequency of the magnetic moment and thereby connects the quantum mechanical description with the classical description of the NMR phenomenon.

The population of both energy states is neither identical nor static. The ground state N_0 $\left(m_s = +\frac{1}{2}\right)$ is slightly more occupied than the excited state N_1 $\left(m_s = -\frac{1}{2}\right)$; the ratio follows the Boltzmann distribution

$$\frac{N_1}{N_0} = e^{-\frac{\Delta E}{k_B T}} \qquad [10]$$

with ΔE being the difference in energy between the two states (equation [8]), with k_B being the Boltzmann constant and T the absolute temperature.

Due to the higher population of the ground state, a net magnetization $\overrightarrow{M_0} = (0,0,M_z)$ (also called equilibrium magnetization) is existent which will be used for further considerations.

In general, the magnetization, defined for a voxel with volume V is basically the sum of all magnetic moments present in the respective voxel:

$$\vec{M} = \frac{1}{V} \sum_{\substack{protons \\ in\ V}} \vec{\mu}_i \qquad [11]$$

It is useful for further observations to differentiate between longitudinal $\left(\overrightarrow{M_{\parallel}}\right)$ and transversal $\left(\overrightarrow{M_{\perp}}\right)$ magnetization with respect to the external magnetic field $\overrightarrow{B_0} = (0,0,B_z)$.

$$M_{\parallel} = M_z \qquad [12]$$

$$\overrightarrow{M_{\perp}} = M_x\hat{x} + M_y\hat{y} \qquad [13]$$

The considerations discussed so far consider a stationary reference frame, the laboratory frame of reference *(x,y,z)* in which the magnetization rotates with the Larmor frequency around the axis of the external static magnetic field. For the following, it is essential to introduce the rotating frame of reference *(x',y',z')* that rotates with the Larmor frequency around B_0. When observing $\vec{M}_0$ from the rotating frame of reference, it is stationary. This helps to understand the complex behavior of $\vec{M}_0$ when further radiofrequency fields are added to the experiment in the next section.

2.1.2 Relaxation processes

The first major component of the NMR experiment, the external magnetic field, and its effect on NMR active nuclei has been illustrated in the previous section. The next component, namely the application of a radiofrequency field exhibiting the Larmor frequency (equation [9]) is introduced in this paragraph. Therefore, it is important to consider interactions between spins which is not covered by the relationship given in equation [2].

Figure 2a illustrates equation [11] and outlines the meaning of the magnetization vector $\vec{M}$. The transmission of radiofrequency (RF) with the Larmor frequency (Figure 2b) leads to the excitation of the system and hence the tipping of the equilibrium magnetization out of the *z* direction. If enough energy is administered, the longitudinal component becomes zero while the transversal part reaches a maximum in Figure 2c.

Following an excitation of the system, return to the equilibrium state (Figure 2) takes place. The longitudinal magnetization builds up via interactions of protons with the surrounding according to

$$M_z(t) = M_z(0)e^{-\frac{t}{T_1}} + M_0\left(1 - e^{-\frac{t}{T_1}}\right). \qquad [14]$$

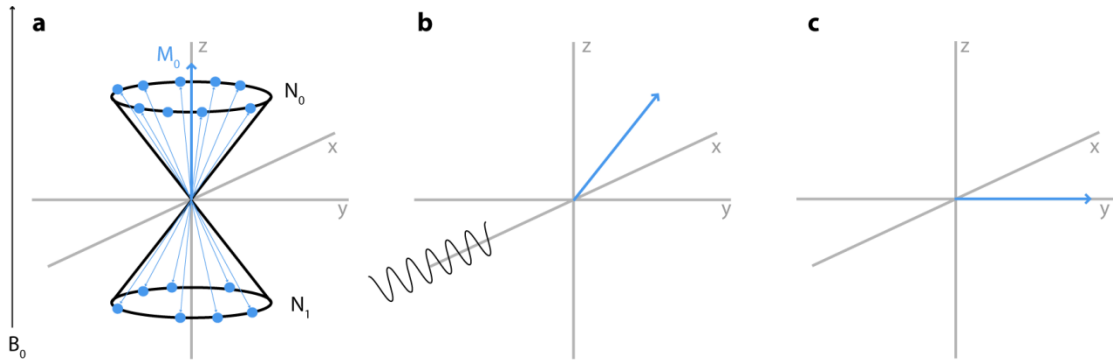

Figure 2: **Magnetization under the effect of an additional RF field**
(a): The net magnetization results from the sum of all magnetic moments distributed in two energy states for a spin ½ nucleus. **(b):** The transmission of an RF field with the Larmor frequency excites the system and tips the initial magnetization away from the longitudinal direction. **(c):** The system is thus far excited that the longitudinal component is zero. Figure adapted from [HAACKE1999] (Chapter 4).

This holds true for the general assumption that the external magnetic field $\overrightarrow{B_0}$ is aligned along the *z* direction and that $\vec{M}_0$ is the magnetization corresponding to the original state. The constant T_1 is the spin-lattice or longitudinal relaxation time. It varies for different tissue types and is magnetic field strength dependent.

In addition to the rebuilding of longitudinal magnetization, the transversal magnetization decays due to spin-spin interactions:

$$\vec{M}_\perp = \vec{M}_\perp(0)e^{-\frac{t}{T_2}} \qquad [15]$$

The spin-spin or transversal relaxation time T_2 differs for various tissue types and is less magnetic field strength dependent. The relaxation time T_2 is much shorter than T_1.

Spin-spin interactions are equivalent to a loss of phase coherence between spins. Due to locally varying magnetic fields caused by neighboring spins, spins are affected variably and consequently the net magnetization dephases. There is an additional dephasing caused by external magnetic field inhomogeneities which accelerates the decay described by the relaxation time T_2'. The combined relaxation time is T_2^*. T_2^* strongly depends on the magnetic field strength (linear relationship) due to the pronounced external magnetic field inhomogeneites at higher magnetic fields.

$$\frac{1}{T_2^*} = \frac{1}{T_2} + \frac{1}{T_2'} \qquad [16]$$

The mechanisms described in equations [14] and [15] are combined in the Bloch equation [BLOCH1946b] which governs the magnetization as a function of time:

$$\frac{d\vec{M}}{dt} = \gamma\vec{M} \times \vec{B}_{ext} + \frac{1}{T_1}(M_0 - M_z)\hat{z} - \frac{1}{T_2}\vec{M}_{\perp} \qquad [17]$$

2.2 Magnetic Resonance Imaging

The concept of NMR was transferred to MRI in 1973 by Lauterbur and Mansfield who were awarded with the Nobel Prize in Physiology or Medicine in 2003. The basic idea was to apply a spatially varying magnetic field (gradient) to implement spatial encoding. The underlying concepts are briefly introduced in this chapter.

2.2.1 Spatially varying magnetic fields

To correlate NMR signal with a specific position within an object, three-dimensional spatial encoding is needed. Therefore, spatially varying magnetic fields or so called magnetic field gradients are applied in three orthogonal directions within the MR experiment. In this section, it is assumed that the additional magnetic field is applied along the *x* direction. Notwithstanding this simplification, the relations holds true for the general case.

A linearly varying magnetic field that is superimposed in *x* direction to the static magnetic field results in a spatially varying *x* component of the effective magnetic field:

$$B_x(x,t) = B_0 + xG_x(t) \qquad [18]$$

G_x is the linear gradient of the added magnetic field:

$$G_x = \frac{\partial B_x}{\partial x} \qquad [19]$$

As a consequence, the Larmor frequency depends on the position of the spins (Figure 3) with:

$$\omega_x(x,t) = \omega_0 + \omega_G(x,t) = \omega_0 + \gamma x G_x(t) \qquad [20]$$

This relationship is exploited for frequency and phase encoding as well as for slice selection in 2D imaging. These concepts are briefly described in the following sections.

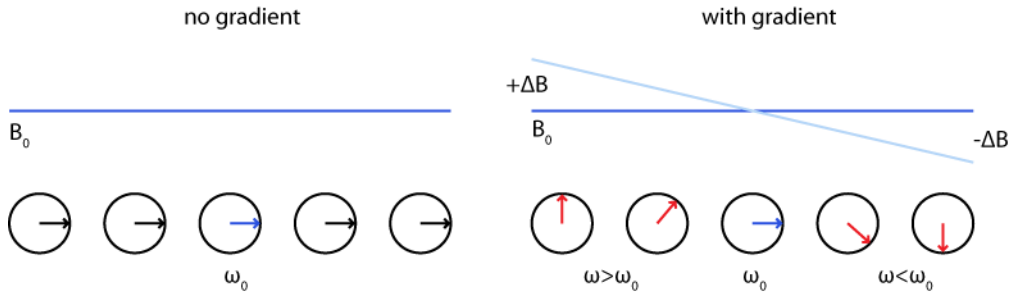

Figure 3: **Spatially varying magnetic fields**
Left: Five spins are depicted exemplary exhibiting equivalent Larmor frequency in case of a static magnetic field. **Right:** An extra linearly varying magnetic field (gradient) introduces spatial encoding of the effective magnetic field and the precession frequency. Figure adapted from [HAACKE1999] (Chapter 10).

2.2.2 Slice selection

For 2D imaging, an RF pulse is applied together with a magnetic field gradient along the slice selection direction, commonly denoted with *z*. The goal is to excite – in the ideal case – a rectangular shaped slice. Sinc-shaped RF pulses deliver nearly rectangular slice profiles and are therefore commonly used for slice selection.

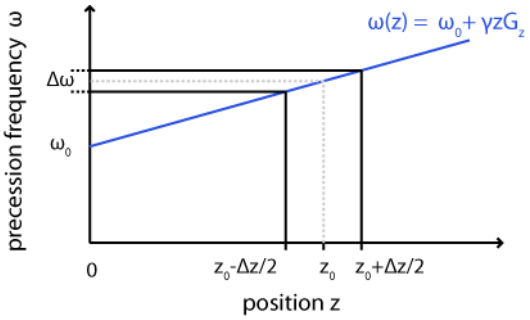

Figure 4: **Slice selection**
The spin precession frequency is linearly dependent on the position *z*. The slice thickness *Δz* is directly linked to the range of precession frequencies *Δω* defined by the bandwidth of the RF pulse which is applied in conjunction with the slice selection gradient. Figure adapted from [HAACKE1999] (Chapter 10).

The dependence of the spin precession frequency on the position *z* is illustrated in Figure 4. The width *Δz* of the selected slice centered on z_0 defines the range of precession frequencies *Δω*. This is directly linked to the bandwidth *BW*, i.e. the frequency range of the applied RF pulse:

$$BW = \Delta\omega = \gamma G_z \Delta z \qquad [21]$$

With this, the slice thickness can be determined from pulse sequence specific parameters:

$$\Delta z = \frac{BW}{\gamma G_z} \qquad [22]$$

To ensure that all spins within the excited slice have zero phase after slice encoding, a slice selection gradient is commonly accompanied by a rephasing gradient of reversed polarity and half first moment, i.e. the product of amplitude and duration.

2.2.3 The k-space concept

The overall goal of an MR experiment is to determine the spin density *ρ* of the nucleus of interest. This measure is included in the signal that is acquired in the simplified 1D case:

$$s(t) = \int dx \rho(x) e^{-\Phi_G(x,t)} \quad [23]$$

ρ(x) is the 1D spin density specified in equation [24] and $\Phi_G(x,t)$ constitutes the accumulated phase due to an applied gradient in *x* direction.

$$\rho(x) = \int \int dy dz \rho(\vec{r}) \quad [24]$$

Moving to a representation in dependence on the spatial frequency *k=k(t)*, the acquired signal can be written as:

$$s(k) = \int dx \rho(x) e^{-i2\pi kx} \quad [25]$$

The spatial frequency is dependent on the applied gradient *G*:

$$k(t) = \gamma \int_0^t dt' G(t') \quad [26]$$

For the simple case of a constant gradient, the spatial frequency is $k=\gamma Gt$.

Equation [25] describes the Fourier transform of the 1D spin density *ρ(x)*. This implies that the spin density can be calculated from the acquired signal via inverse Fourier transform:

$$\rho(x) = \int dk\, s(k) e^{+i2\pi k} \quad [27]$$

In other words, the image space *x* is linked with the data space *k* via inverse Fourier transform. The application of a linear gradient, in this example along *x*, implicates a Fourier encoding along *x*.

2.2.4 Spatial encoding

To resolve the spin density in three dimensions, the already described slice selection (*z*) is accompanied by two Fourier encoding directions: frequency (k_x) and phase (k_y) (see Figure 5 for directions).

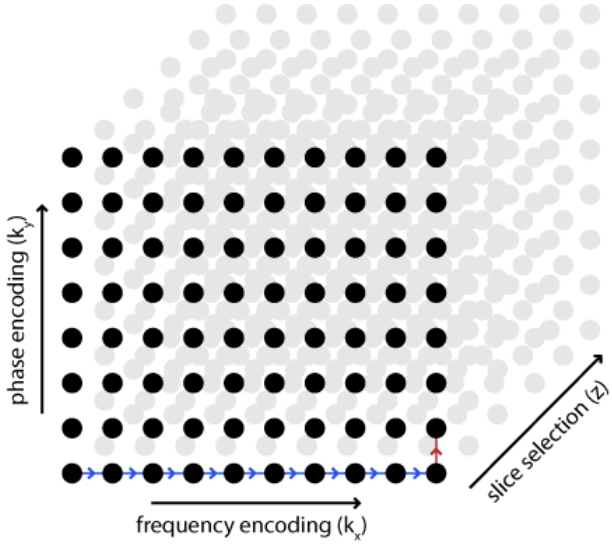

Figure 5: **Three-dimensional schematic k-space illustration**
Slice selective excitation in *z* direction extracts a two-dimensional space of the object. Frequency encoding (k_x) and phase encoding (k_y) resolve the data space in the missing two directions. Figure adapted from [HAACKE1999] (Chapter 10).

A linear gradient along *x* reveals spatial information along one line k_x in k-space according to equation [20] (blue line in Figure 5). Stepwise increasing of linear gradients along *y* lead to an increment in k-space along the phase encoding direction k_y (red line in Figure 5) and enables the acquisition of further k_x lines.

The encoding in k_x and k_y direction is based on phase differences between spins due to linearly spatially dependent precession frequencies. Therefore the terms frequency and phase encoding are slightly confusing. However, they are going to be used throughout this thesis.

To put the described concepts in a more practical concept, namely a pulse sequence, Figure 6 summarizes slice selection, frequency and phase encoding and data acquisition in a basic pulse sequence diagram. The numbers in brackets denote different steps in the imaging process: (1) slice selection; (2) phase encoding; (3) frequency encoding preparation; (4) frequency encoding; (5) data acquisition. These stages are visualized in chronological order. This basic scheme applies to all 2D imaging techniques.

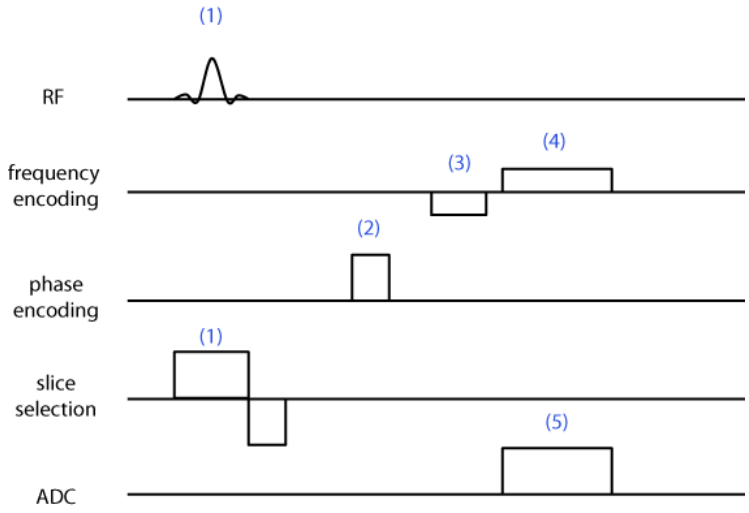

Figure 6: **Pulse sequence diagram illustrating spatial encoding steps**
A typical MR pulse sequence diagram showing the radiofrequency (RF), frequency and phase encoding as well as slice selection gradients and the acquisition part (ADC: analog-to digital converter). Different parts of the imaging process are denoted with numbers: (1) slice selection; (2) phase encoding; (3) preparation of frequency encoding; (4) frequency encoding; (5) data acquisition. The horizontal axis displays the time.

2.2.5 Basic magnetic resonance imaging techniques: Spin echo and gradient echo

All MR pulse sequences can be classified into two sequence types: spin echo and gradient echo techniques. In doing so, the first matter to clarify is the question what an echo is. Spins dephase while they are in the transversal plane and as a result the net transversal magnetization decreases.

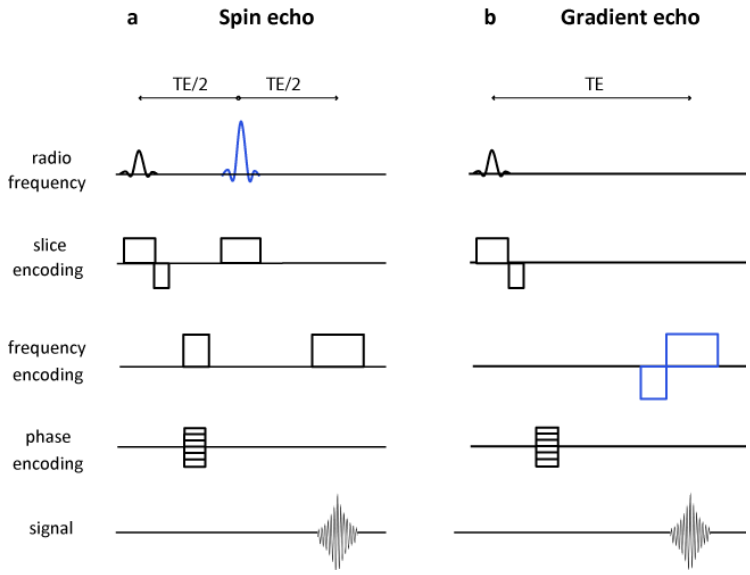

Figure 7: **Basic MR pulse sequences: spin echo and gradient echo**
(a): A refocusing pulse (marked in blue) following the excitation leads to the rephasing of the dephased spins and hence to the generation of the echo in the spin echo sequence. **(b):** For the gradient echo case, a combination of two gradients in frequency encoding direction (marked in blue) rephases the spins and generates the echo.

Rephasing of the spins leads to the generation of an echo. In the case of a spin echo rephasing is induced by a refocusing RF pulse (Figure 7a) [HAHN1950]. To form a gradient echo, a magnetic field gradient along the frequency encoding direction rephases the spins and leads to an echo (Figure 7b) [MANSFIELD1977b]. In fact, the spin echo is a combination of spin and gradient echo since a magnetic field gradient along the frequency encoding direction is applied to encode the echo (Figure 7a).

In both cases, the echo time (TE) defines the time between the excitation and the echo occurrence. TE is a highly relevant sequence parameter that defines the contrast in images. A further parameter, namely the repetition time (TR) defining the time between two consecutive excitations is equally important for the image contrast. Setting TE short and TR long represses the effect of transversal relaxation and creates proton density (PD) contrast since the nearly fully recovered longitudinal relaxation is dependent on the proton density of tissue (Figure 8). Prolonging TE and keeping TR long changes the contrast to T_2 since the effect of transversal relaxation comes to the fore. Choosing a short TE and short TR suppresses the effect of proton density as well as transversal relaxation and results in T_1 contrast.

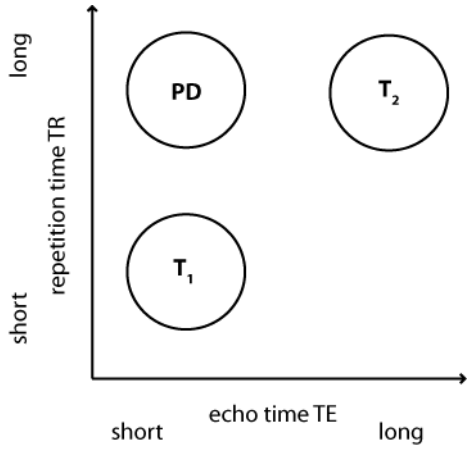

Figure 8: **Image contrast in dependence on TE and TR**
A short TE together with a short TR generates a T_1 contrast since T_2 effects are cancelled out. Contrariwise, a long TE joined by a long TR freezes T_1 effects and generates a T_2 contrast. For PD contrast, T_1 and T_2 effects need to be discarded and hence a short TE and long TR are needed.

For the following, the focus is set on the spin echo sequence since this concept plays a central role in this thesis. Figure 9 schematically depicts the generation of a spin echo following an excitation and a refocusing.

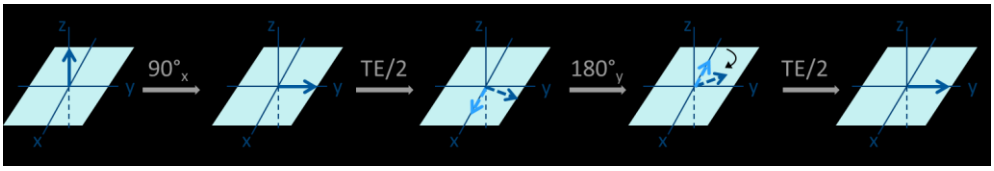

Figure 9: **Schematic illustration of the spin echo generation**
The net magnetization along the z direction is brought into the transversal plane by a 90° excitation RF pulse. During the time period TE/2, the spins dephase since they precess with different frequencies depending on their position. A 180° RF pulse flips the total transversal magnetization. The spins keep their direction and frequency of precession. As a result, after TE/2 they are again aligned along the y direction and form a spin echo. Figure adapted from [HAACKE1999] (Chapter 8).

2.2.6 Signal-to-noise ratio calculation

One important criterion for image quality in MRI is signal-to-noise ratio (SNR). Various methods for measuring SNR in MRI images have been proposed [HENKELMAN1985, CONSTANTINIDES1997, SIJBERS1998, KELLMAN2005]. For fully sampled magnitude images SNR measurement is commonly performed using the background as noise estimation [HENKELMAN1985, CONSTANTINIDES1997]:

$$SNR = c \cdot \frac{\bar{S}_{ROI\ (object)}}{\sigma_{ROI\ (outside\ object)}} \qquad [28]$$

$\bar{S}_{ROI(object)}$ is the mean value of signal intensity within a region of interest (ROI) placed in a region with homogeneous signal. The standard deviation $\sigma_{ROI(outside\ object)}$ derived from a ROI placed in the background provides an estimate for noise within the image. The correction factor c accounts for the probability density distribution of noise, which is a Rician distribution. Positive and negative variations of noise become positive in magnitude reconstructed images, causing a slight underestimation of σ [HENKELMAN1985]. The correction factor depends on the number of receiver RF coil elements since the reconstruction algorithm for multi-channel RF coil arrays changes the probability density distribution of noise. c has been calculated for a single-element receiver RF coil and equals 0.655 [HENKELMAN1985]. The concept has been expanded by [CONSTANTINIDES1997]. The correction factor is 0.703 for a 12-element RF coil employed for measurements presented in this thesis.

2.3 Rapid Acquisition with relaxation enhancement (RARE)

2.3.1 Basic principle

In the 1980s, when MR was translated into early clinical applications, long acquisition times constituted severe constraints for clinical imaging due to image artifacts caused by patient motion. These constraints prompted explorations into fast imaging techniques. In 1985 FLASH (Fast Low-

Angle Shot) imaging was introduced [HAASE1986]. The free induction decay (FID) generated by a low angle RF pulse is detected as a gradient echo. The repetition of this succession enables the acquisition of an image in few seconds. Approximately at the same time a further fast imaging method was proposed. Contrary to FLASH this approach primarily builds on spin echo imaging and was designated as Rapid Acquisition with Relaxation Enhancement (RARE) [HENNIG1984, HENNIG1986, HENNIG1988b]. RARE is based on the principle of echo imaging [MANSFIELD1977a] and employs independent phase encoding for each echo in a train of equidistant echoes. The echo train approach results in a drastic reduction in scan time versus conventional spin echo imaging which was up to then commonly used for anatomical imaging.

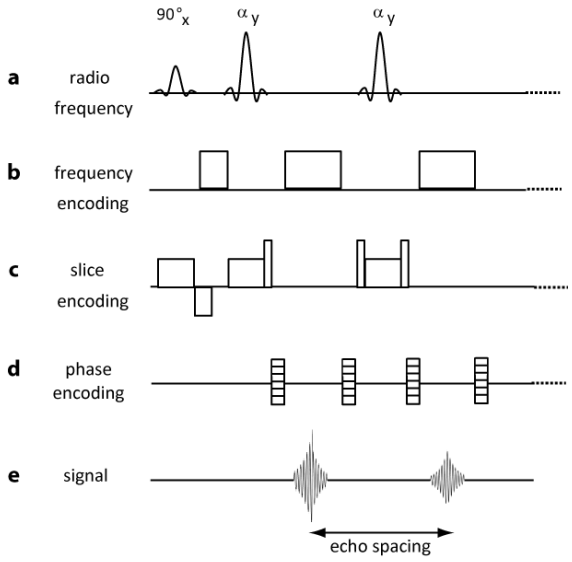

Figure 10: **Basic RARE sequence diagram**
The RF pulse train, frequency encoding, slice encoding and phase encoding gradients are shown along with the corresponding signal. The incremental phase encoding gradients illustrate the different encoding steps within the echo train.

Figure 10 shows the basic RARE sequence diagram. After a slice selective excitation RF pulse a train of refocusing RF pulses is applied whereby a series of echoes is generated. The original publication employed 180° refocusing RF pulses [HENNIG1986]. A RARE variant called FLARE (Fast Low Angle Refocused Echo imaging) uses refocusing RF pulses with smaller flip angles [HENNIG1988a] . UFLARE (Ultra-Fast Low Angle RARE) is a single-shot variant of FLARE [NORRIS1991].

In basic RARE sequences, the phase of the refocusing RF pulses is commonly offset by 90° from the phase of the excitation RF pulse (Figure 10a) to meet the Carr-Purcell-Meiboom-Gill (CPMG) condition for multi-echo pulse sequences [CARR1954, MEIBOOM1958]. For the same reason the timing needs to be periodic, i.e. the refocusing RF pulses are all separated by a constant length of

time, the echo spacing (ESP) and the time between the excitation RF pulse and the first refocusing RF pulse is exactly half of the ESP [MEIBOOM1958]. Furthermore, the CPMG condition assumes that the phase accumulated between two refocusing RF pulses is equal for each echo spacing. This is realized via symmetric crusher gradients in slice encoding direction surrounding the refocusing RF pulses with the exception of the first one, where the left crusher gradient is combined with the slice reversal gradient of the excitation RF pulse (Figure 10c). For the same reason, each phase encoding gradient is followed by a gradient exhibiting the same absolute first moment but reversed polarity (Figure 10d). To prepare the magnetization prior to the first refocusing RF pulse a dephasing gradient featuring exactly half of the first moment of the frequency encoding gradient is included after the excitation RF pulse (Figure 10b). By fulfilling all these requirements it is ensured that an echo is generated after each refocusing RF pulse exactly at the center frequency. The following sections are going to reveal that each echo is composed by different echo types and further clarify the importance of the above described requirements in the design of RARE sequences.

The contrast of RARE images is mainly dominated by T_2 relaxation and given by the effective TE (TE_{eff}), which is the time between the excitation RF pulse and the acquisition of the k-space line with zero phase encoding. By changing the position of the zero phase encoding line within the echo train T_2 weighting can be modified [MULKERN1990, MULKERN1991]. The most commonly used so called center-out phase encoding scheme is visualized in Figure 11. Here, a case employing minor T_2 weighting is shown since the signal belonging to the first echo is stored in the center of k-space. Assuming an ESP of 8 ms, TE_{eff} equals 8 ms for this example. To increase the extent of T_2 weighting, not the first but one of the subsequent echoes would need to be positioned in the center of k-space. For the previous example TE_{eff} would be 32 ms in case of the fourth echo being placed in the k-space center. The echo train length (ETL) gives the number of refocusing RF pulses after an excitation RF pulse and hence determines the number of excitations needed for a given matrix size. In the example depicted in Figure 11, the ETL is four, meaning that 32 excitations are needed for a matrix of 128 phase encoding steps. As a result, 32 echoes arising from the first echo spacing are available which are all stored in the center segment (dark gray) visualized in the schematic k-space in Figure 11. All later echoes are distributed symmetrically to positive and negative frequencies resulting in segments containing 16 lines each for the given example.

RARE can be combined with other k-space sampling techniques like spiral or radial acquisitions [BLOCK1997, PIPE1999] and can furthermore be carried out as a 3D pulse sequence. This thesis concentrates on the 2D RARE using the described center-out Cartesian phase encoding scheme though.

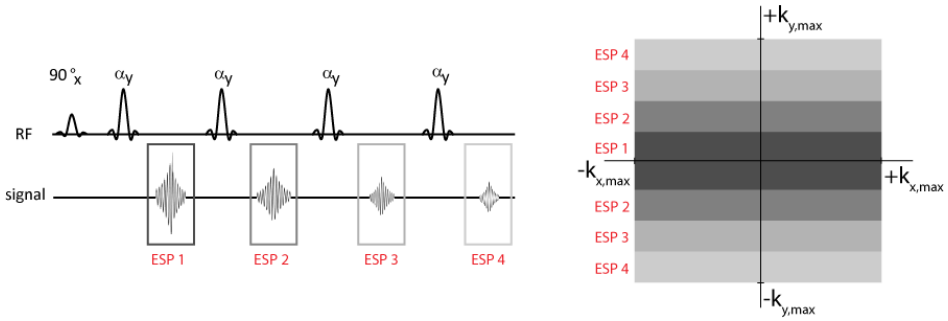

Figure 11: **Center-out Cartesian phase encoding scheme**
RARE sequence with an ETL of 4 showing the RF pulses and the corresponding signal (**left**). Schematic k-space visualizing the center-out phase encoding scheme (**right**). The different shades of gray represent signals from different echo spacing each exhibiting particular T_2 weighting.

Various alternative names arose for the original RARE sequence including FAISE (fast acquisition interleaved spin echo, [MELKI1991]), FSE (fast spin echo, [CONSTABLE1992a, JONES1992]) and TSE (turbo spin echo, [SEELOS1993]) and were taken over by different MR scanner manufacturers. For reasons of consistency the generic pulse sequence name RARE will be used throughout this thesis.

2.3.2 Arbitrary radiofrequency pulses

In the ideal and simplified perspective 180° refocusing RF pulses are used within the echo train of RARE sequences. 180° refocusing RF pulses provide the most complete refocusing of transverse magnetization and hence the maximum available signal. However, the real situation is different. Even for nominal 180° RF pulses, perfect refocusing is hampered by RF pulse imperfections and by slice profiles deviating from an ideal rectangular shape. As a result of this, arbitrary flip angle RF pulses need to be regarded.

The effect of an RF pulse with flip angle α around a specified axis (in this exemplary case x) can be described as a three dimensional rotation of the magnetization vector $\vec{M}^-$ prior to the RF pulse, resulting in $\vec{M}^+$ directly after the RF pulse:

$$\vec{M}^+ = R_x(\alpha)\vec{M}^- \qquad [29]$$

The rotation matrix $R_x(\alpha)$ is thereby described as

$$R_x(\alpha) = \begin{pmatrix} 1 & 0 & 0 \\ 0 & cos\alpha & sin\alpha \\ 0 & -sin\alpha & cos\alpha \end{pmatrix} \qquad [30]$$

For the three elements of the rotated magnetization vector the following relations apply:

$$M_x^+ = M_x^- \quad [31]$$

$$M_y^+ = M_y^- cos\alpha + M_z^- sin\alpha \quad [32]$$

$$M_z^+ = -M_y^- sin\alpha + M_z^- cos\alpha \quad [33]$$

The complex magnetization F and its complex conjugate F^*, representing transversal magnetization are defined as

$$F = M_x + iM_y$$
$$F^* = M_x - iM_y \quad [34]$$

Combining equations [31]-[33] with equation [34] provides the subsequent description of magnetization directly after a RF pulse:

$$F^+ = F\, cos^2\frac{\alpha}{2} + F^* \sin^2\frac{\alpha}{2} + iM_z sin\alpha \quad [35]$$

$$M_z^+ = M_z \cos^2\frac{\alpha}{2} + M_z \sin^2\frac{\alpha}{2} + \frac{1}{2} i(F - F^*) sin\alpha \quad [36]$$

Based on equations [35] and [36] the effect of an arbitrary flip angle RF pulse can be exemplified. In general, the effect of an RF pulse can be considered as a linear combination of 180°, 90° and 0° rotations of the magnetization vector around the specified axis of the RF pulse [HAHN1950, WOESSNER1961], which is illustrated in Figure 12.

- For transverse magnetization prior to the RF pulse, the 0° rotation results in a part of magnetization which continues to evolve in the transverse plane (first term in equation [35]). Longitudinal magnetization affected by the 0° part stays longitudinal and T_1 relaxation towards M_0 continues (first term in equation [36]). The effective amplitude of the 0° component is $\cos^2(\alpha/2)$ (solid lines in Figure 12).
- Transverse magnetization experiencing the 90° component is tipped to the longitudinal axis, thereby one half keeps the accumulated phase unchanged while the other half inverts it (third term in equation [36]). Prior longitudinal magnetization, either fresh or stored, is brought to the transversal plane (third term in equation [35]). The quantity of the 90° effect is $\sin(\alpha)$, in which this part is divided into two fractions for the prior transverse magnetization (dashed lines in Figure 12).
- The third component, 180°, inverts the phase of transverse magnetization (second term in equation [35]) and inverts longitudinal magnetization (second term in equation [36]) with an effective amplitude of $\sin^2(\alpha/2)$ (dash-dotted lines in Figure 12).

With the help of these considerations, the development and also the amplitude of different echoes in a multi-pulse experiment can be observed. This will be surveyed in more detail in the following section.

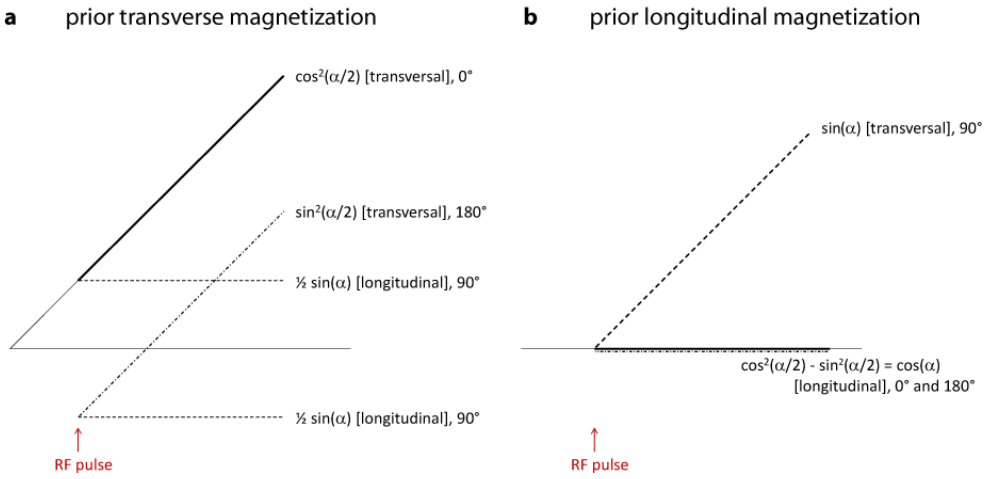

Figure 12: **Effect of an arbitrary flip angle RF pulse on magnetization**
An arbitrary flip angle RF pulse branches prior transverse magnetization (**a**) into four parts and prior longitudinal magnetization (**b**) into three parts. (adapted from [HAACKE1999], p.492). The amplitude reduction is given for each new branch after the RF pulse together with the type of magnetization (either transversal or longitudinal).

2.3.3 Extended phase graph algorithm

The extended phase graph (EPG) algorithm has been developed to provide a tool that describes multi-pulse experiments [HENNIG1991a, HENNIG1991b, WEIGEL2015]. It goes back to former considerations on diffusion-weighted spin echo NMR experiments [WOESSNER1961, KAISER1974]. When describing a multi-pulse experiment, two facets are of interest: the location of echoes and their amplitudes. These would be hard to determine if one would try to follow each single isochromat. Therefore, in the picture of the EPG algorithm, groups of isochromats are considered which are affected in the same manner by RF pulses and develop a phase between RF pulses due to free precession. These groups, also called spin configurations, are represented by spin phase pathways. Whenever the phase crosses the abscissa, it marks the occurrence of an echo. The term extended phase graph arose since the algorithm does not use the common description of magnetization using three orthogonal terms M_x, M_y and M_z but four states F_n, F_n^*, Z_n, Z_n^*. These states specify the isochromats' extent of dephasing.

A three-pulse experiment, visualized schematically in Figure 13, is used as an example to outline the EPG algorithm. First, it is important to note that the phase evolution between RF pulses is merely due to free precession. T_1 relaxation of longitudinal magnetization and T_2 decay of

transverse magnetization is not considered at this point. Second, no imaging gradients are taken into account for now, but will play an essential role later on. Different spin configurations are depicted by individual lines in the EPG. Longitudinal magnetization is represented by horizontal lines, transversal parts by upward lines. RF pulses split each spin configuration: four branches are created from prior transversal magnetization and three branches from beforehand longitudinal magnetization. Taking this into account, it becomes obvious that five different echoes are generated by a series of three arbitrary RF pulses.

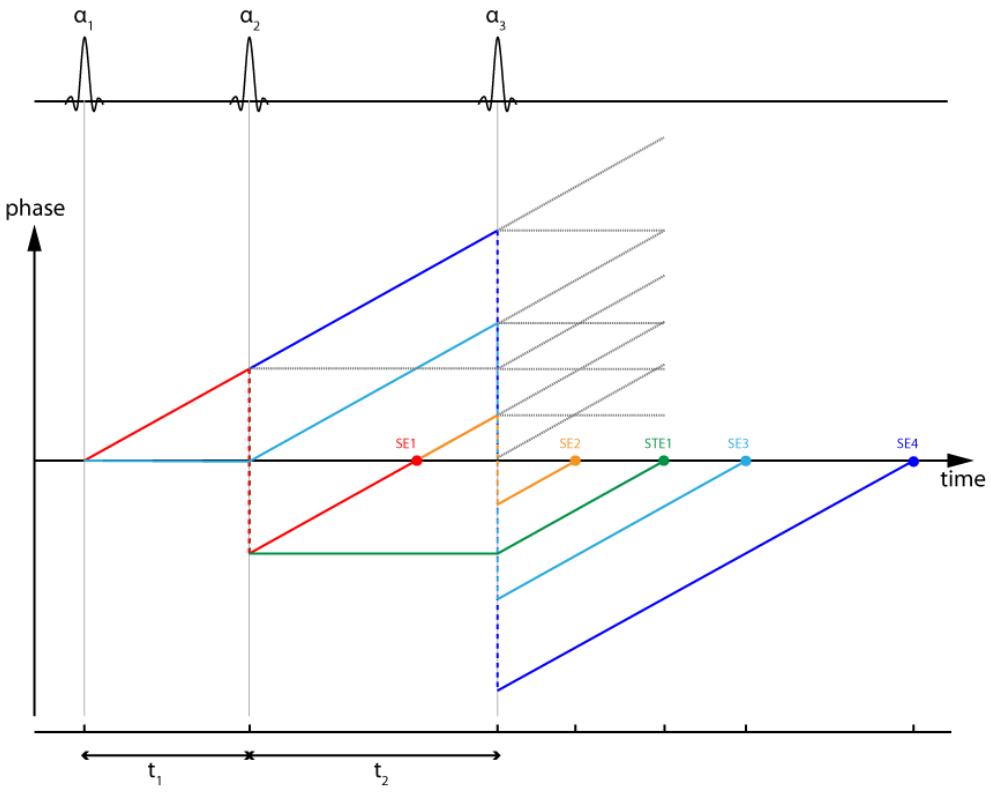

Figure 13: **Extended phase graph diagram for a three-pulse experiment**
The phase evolution of different spin configurations is shown over time. Vertical gray lines represent RF pulses which fork each longitudinal configuration into three parts and each transversal configuration into four parts. Five echoes are generated by three arbitrary RF pulses. These are depicted in different colors. It is important to note that the echo which ranks third in time (green line) is a stimulated echo, meaning that the magnetization has been stored along the longitudinal axis during at least one ESP. Spin configurations that do no lead to an echo within the three-pulse experiment are marked in gray.

The first question concerning multi-pulse experiments, namely the position of all occurring echoes, is now answered. Simply following the different spin phase pathways in the EPG reveals that information. For determining the amplitudes of the five echoes in the three-pulse experiment it is helpful to go back to Figure 12 on page 19 where the effect of an arbitrary flip angle RF pulse has been discussed. To illustrate the calculation of echo amplitudes, SE4 (Figure 13) is taken as an example. Starting with longitudinal magnetization, the first RF pulse α_1 flips $\sin(\alpha_1)$ of the initial

magnetization into the transversal plane. At the branching point of the second RF pulse $\cos^2(\alpha_2/2)$ of this part continues to dephase. With the third RF pulse the phase of $\sin^2(\alpha_3/2)$ of the current magnetization gets inverted. As a result, the echo SE4 occurs at the time $2(t_1 + t_2)$. Table 2 summarizes the amplitudes of all five echoes occurring in a three-pulse experiment. Assuming perfect 180° refocusing RF pulses in a RARE experiment with two refocusing RF pulses (i.e. a three-pulse experiment with $\alpha_1 = 90°$, $\alpha_2 = \alpha_3 = 180°$), the echo SE4 would not occur, since α_2 rephases the complete magnetization and no part of it continues to dephase (equation [41] in Table 2). For $\alpha_2 \neq 180°$ and/or $\alpha_3 \neq 180°$ while keeping $\alpha_1 = 90°$ the magnetization pathway resulting in the echo SE4 is populated and the echo is generated with an amplitude depending on the exact flip angle of α_2 and α_3.

The five echoes resulting from the three-pulse experiment can be divided into two groups. One is the echo family of spin echoes (SE), the second one is the family of stimulated echoes (STE), a classification introduced by Hahn [HAHN1950]. Table 2 reveals that four SEs and one STE are formed in the three-pulse experiment. A simple feature to distinguish between SE and STE is the fact, that the magnetization forming a STE has been stored along the longitudinal axis for at least one ESP, depicted exemplary by the horizontal green line in Figure 13.

Table 2: **Amplitudes of echoes in a three-pulse experiment**
The amplitudes of the five echoes occurring in an arbitrary flip angle three-pulse experiment are summarized.

Echo	Amplitude	
SE1	$sin\alpha_1 \sin^2\frac{\alpha_2}{2}$	[37]
SE2	$sin\alpha_1 \sin^2\frac{\alpha_2}{2} \sin^2\frac{\alpha_3}{2}$	[38]
STE1	$\frac{1}{2} sin\alpha_1 sin\alpha_2 sin\alpha_3$	[39]
SE3	$cos\alpha_1 sin\alpha_2 \sin^2\frac{\alpha_3}{2}$	[40]
SE4	$sin\alpha_1 \cos^2\frac{\alpha_2}{2} \sin^2\frac{\alpha_3}{2}$	[41]

2.3.4 Echo formation

Combining the concepts described in the previous sections permits the description of signal formation within RARE. The EPG in Figure 14 additionally includes dephasing due to frequency encoding gradients; in comparison to the graph in Figure 13 where solely free precession has been considered. Including the frequency encoding gradients in the following considerations

emphasizes the fact that the signal in RARE is not merely a spin echo/stimulated echo signal but also contains gradient echo parts.

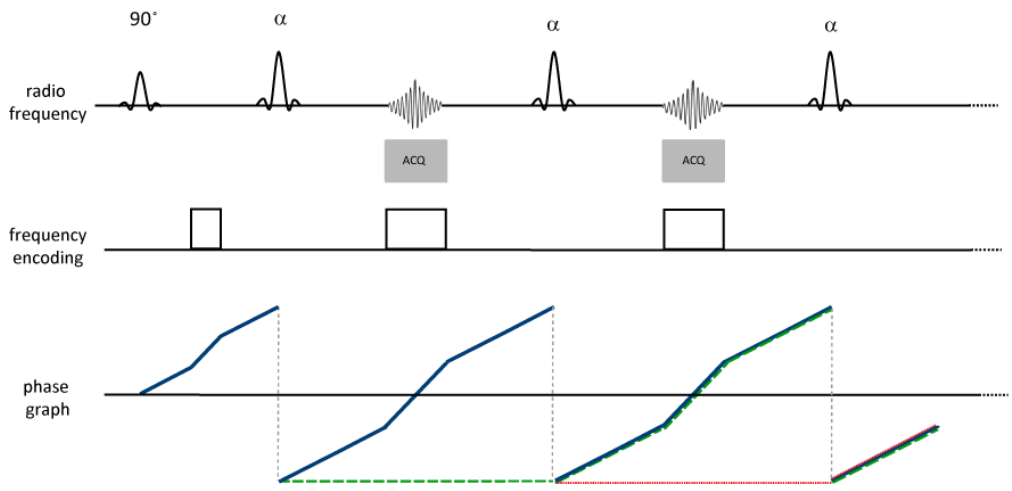

Figure 14: **Signal formation in RARE sequences**
Radio frequency pulses together with the signal in the acquisition period are shown alongside the frequency encoding gradients and the phase graph showing only selected pathways. It is important to note that the phase graph here includes dephasing due to free precession (smaller slope) as well as due to frequency encoding gradients (larger slope). T_1 and T_2 relaxation are not considered.

The perfect trimming of the dephasing gradient after the excitation RF pulse to exactly half of the moment of the readout gradients in between the refocusing RF pulses realizes the echo positioning at the center frequency. This is illustrated in the phase graph in the bottom line of Figure 14 and best to understand when following the magnetization path of the primary spin echo (blue solid line, SE1 in the three-pulse experiment). Stimulated echoes contribute to the signal from the second ESP on (green dashed line, STE1 in the three-pulse experiment). The added secondary stimulated echo (red dotted line) indicates that the number of magnetization pathways, either contributing to the signal or being destroyed by further dephasing, grows rapidly with the number of refocusing signals.

Besides the classification into spin echo and stimulated echo groups a further grouping is of importance: each part of the signal belongs to either even or odd echo parity [KAISER1974, BARKER1989, NORRIS1992]. An odd echo is formed by magnetization that has spent and odd number of ESPs in the transversal plane including the one in which the echo is formed. Analogously, an even echo is formed. The assignation corresponding to the two classification attributes is visualized in Figure 15 for the case of an unbalanced dephasing gradient by which the signal is split into its subgroups. It is obvious, that the even/odd echoes come alternately from the SE/STE group.

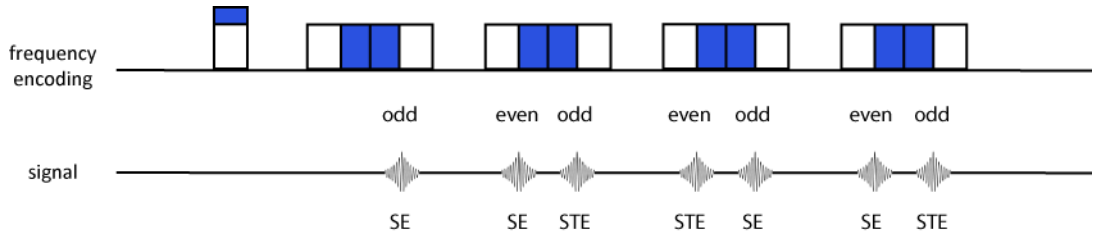

Figure 15: **Echo classification**
An imbalanced dephasing gradient in frequency encoding direction leads to signal separation into its subgroups SE and STE, belonging alternately to odd/even echo parity (graphic adapted from [NORRIS1992]).

Since SE and STE echo groups coincide in coherent RARE, i.e. when all the requirements on the pulse sequence design described in the previous sections are fulfilled, it is important that both groups exhibit approximately the same amplitude. To reach this situation, dummy RF pulses are applied prior to the actual data acquisition. It has been shown that a set of eight dummy RF pulses leads to sufficient signal adjustment [HENNIG1988a, NORRIS1992]. This is an approximation. In case of very low refocusing RF pulse angles for instance, the number of dummy RF pulses should be increased.

2.3.5 Rapid acquisition with Relaxation Enhancement variants

Coherent RARE has already been introduced in the previous section. However, it is worth repeating the conditions for coherent RARE. First, the dephasing gradient in the frequency encoding direction needs to be perfectly trimmed against the readout gradient. Second, the CPMG conditions must be met to avoid interferences. In general, these prerequisites are fulfilled and the RARE sequence can be applied without further special measure. Various situations can occur, in which coherent RARE (Figure 16a) is not appropriate. T_2^*-weighted RARE is one important example as well as diffusion-weighted RARE. Both share in common that extra phase shifts are introduced. T_2^* sensitization is introduced via an evolution time τ inserted after the excitation RF pulse (Figure 16, top line). Thus, additional and unknown phase shifts are accrued due to microscopic B_0 inhomogeneities which are not rephased but carried along the echo train and reflecting the extent of T_2^* weighting. In the case of diffusion-weighted imaging, a net phase is accrued for non-stationary spins via the application of a dephasing diffusion sensitization gradient followed by a rephasing gradient. In both cases, the additional phase leads to destructive interference between odd and even echoes and therefore needs to be accounted for. Displaced RARE (Figure 16c) applies additional gradients along the frequency encoding direction to remove one echo from the acquisition window and subsequently circumventing destructive interferences between echoes of different parity [NORRIS1992]. The reduction to only half of the available signal intensity is one recognized drawback of displaced RARE. An imbalanced dephasing gradient in frequency

encoding direction is put to use in SPLICE (split acquisition of fast spin-echo signals for diffusion imaging) [SCHICK1997] (Figure 16b). This RARE variant generates two complete raw data sets: the first one containing only odd echoes and the second one only even echoes. Both data sets are reconstructed independently and added afterwards. Thus, interferences are avoided while the full available signal is acquired at the cost of a reduced spatial resolution versus coherent RARE using the same matrix size. A third method to account for incoherent interferences due to additional phase shifts in the echo train is the phase-cycling technique [TURNER1984, ZUR1987, BARKER1989, NORRIS1992]. Two measurements are performed with the phase of the refocusing RF pulses being varied in the second experiment. By combining them, the signal from one echo parity is maintained while contributions from the other parity are cancelled.

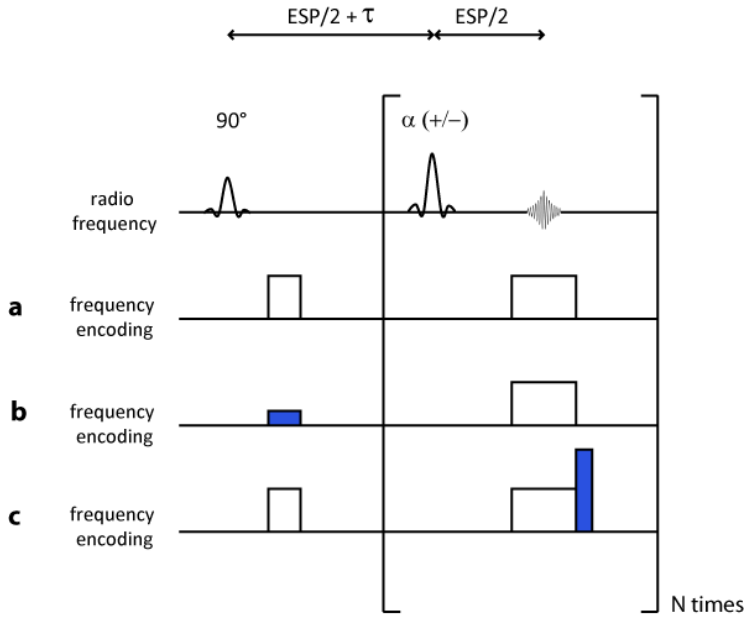

Figure 16: **RARE variants**
T_2^* weighting is introduced into RARE by adding an evolution time τ after the excitation RF pulse. Coherent RARE (**a**) will lead to destructive interference and severe image artifacts in this case. Split-echo RARE (**b**), displaced RARE (**c**) and phase-cycled RARE (denoted by +/- in the top line) are variants to account for the additional unknown phase shifts accrued during the evolution time (graphic adapted from [NIENDORF1999]).

2.4 Methodology of diffusion-weighted imaging

2.4.1 Basic principle

Diffusion-weighted magnetic resonance imaging (DWI) is an approach for probing self-diffusion or restricted diffusion. Diffusion-sensitization of water molecules is of paramount interest for functional human imaging. Self-diffusion describes the movement of molecules within a medium and constitutes a model for Brownian motion which is driven by thermal energy. Hahn [HAHN1950]

described for the first time that the magnetic resonance signal is affected by diffusion. This observation was further detailed by Carr and Purcell [CARR1954]. The original Bloch equations [BLOCH1946a] were expanded by a diffusion term [TORREY1956]:

$$\frac{d\vec{M}}{dt} = \gamma\left(\vec{M} \times \overrightarrow{B_0}\right) + \begin{pmatrix} \frac{M_x}{T_2} \\ \frac{M_y}{T_2} \\ \frac{M_0 - M_z}{T_1} \end{pmatrix} + D\nabla^2\vec{M} \qquad [42]$$

Torrey added the third term which results from considerations of Fick's laws of diffusion [FICK1855]. The diffusion term states the relationship between the diffusion coefficient *D* and the concentration of the diffusive medium which is in this case the magnetization $\vec{M}$. The effect of diffusion on the magnetic resonance signal dependent on the diffusion coefficient *D* of the relevant medium is well expressed in the solution to the Bloch-Torrey-Equation for transversal magnetization:

$$M_x + iM_y = M_{xy} = M_0 e^{-\frac{t}{T_2}} e^{-bD} = S(0)e^{-bD} \qquad [43]$$

The strength of diffusion sensitization is given by the factor *b*. This factor depends on the amplitude (*G*) and duration (*t*) of diffusion sensitizing gradients as well as on the general diffusion sensitization design [PRICE1997, GÜLLMAR2005]:

$$b = \gamma^2 \int_0^{\tau} \left(\int_0^{t} G(t')dt' \right)^2 dt \qquad [44]$$

Stejskal and Tanner [STEJSKAL1965] proposed the application of time-dependent magnetic field gradients for spin diffusion measurement. The Stejskal-Tanner diffusion sensitization sequence applies a pair of diffusion sensitizing gradients placed around a refocusing RF pulse in a spin-echo preparation module. The first gradient induces dephasing of spins depending on the duration and the amplitude of the applied gradient. The accumulated phase is reversed by the second gradient which is applied after the refocusing RF pulse and which exhibits the same amplitude and duration. Complete rephasing only holds true for stationary spins for which the pair of diffusion sensitizing gradients does not induce any net dephasing. Moving spins accumulate net phase dependent on the extent of displacement during the diffusion sensitization time and on the diffusion weighting (b-value, [s/mm^2]). As a result of the phase accrual the acquired signal is attenuated versus the signal without any diffusion sensitization *S(0)* (equation [43]).

For the Stejskal-Tanner preparation experiment the b-value is governed by

$$b = (\gamma G \delta)^2 \left(\Delta - \frac{\delta}{3}\right) \quad [45]$$

The diffusion coefficient *D* can be calculated pixel wise from two MR measurements: one without any diffusion weighting and the second one exhibiting diffusion sensitization given by the respective b-value.

$$D = -\frac{1}{b} ln\left(\frac{S(b)}{S(0)}\right) \quad [46]$$

In human tissue water diffusion is not truly random because of natural barriers like cell membranes, muscle fiber tracts and myelin sheaths. With this phenomenon the diffusion constant D is altered to an apparent diffusion coefficient (ADC).

In 1985, the Stejskal-Tanner preparation was combined with MRI [LE BIHAN1985]. First diffusion-sensitized *in-vivo* images were presented for the brain [LE BIHAN1986]. The spectrum of *in-vivo* applications increased rapidly with the combination of diffusion-sensitized Stejskal-Tanner preparation with an echo planar imaging module [TURNER1990].

Information on the three dimensional process of diffusion can be obtained by diffusion tensor imaging (DTI) [BASSER1994a, BASSER1994b, LE BIHAN2001]. In a simple implementation a 3 x 3 matrix (tensor) is calculated from images with diffusion weighting applied in at least six different directions which are necessary to determine the full tensor. In many applications the number of directions in drastically increased to improve the robustness of the calculations. Two parameters of interest can be deduced from this tensor: the main diffusivity gives information about the extent of diffusion, meaning how much the water molecules move, and the fractional anisotropy reveals to which extent diffusion is depending on a specific direction. A large number of DTI applications evolved since its invention and this number is constantly growing. However, DTI exceeds the scope of this thesis and hence, further considerations concentrate on diffusion-weighted imaging applying diffusion sensitization in one or at maximum three directions.

2.4.2 DWI pulse sequences

Diffusion-weighted MR techniques are sensitive to microscopic but also macroscopic and bulk motion including rigid motion or pulsation due to blood flow. As a result, bulk motion induced unknown phase shifts are acquired which can lead to severe image artifacts. In the case of single-shot sequences the whole k-space is filled after a single excitation. Phase shifts due to macroscopic motion affect all k-space lines and the overall image quality is not degraded. This is

one of the reasons why single-shot EPI (ss-EPI) is nowadays the method of choice for the acquisition of diffusion-weighted images in clinical routine. Single-shot EPI comes with a very fast data readout whereby sensitivity to rigid motion is minor, and offers high SNR. Single-shot EPI constitutes a major shortcoming however, which is due to its propensity to geometric distortions. Distortions are mainly caused by magnetic field inhomogeneities resulting in off-resonance effects which are particularly pronounced at air-tissue interfaces due to severe changes in the magnetic susceptibility. In the case of ss-EPI eddy current induced distortions reinforce the impediment. ss-EPI is specifically affected since all k-space lines are filled sequentially and phase shifts due to off-resonance effects accumulate during the readout. Geometric distortions are pronounced when moving to high magnetic field strengths ($B_0 \geq 3.0$ T), when using long echo trains together with long inter-echo spacing for high spatial resolution imaging or in target regions covering air-tissue interfaces. A ss-EPI alternative that offers immunity to image distortions but imaging speed and SNR competitive with ss-EPI is conceptually appealing for the pursuit of anatomically accurate DWI.

Single-shot RARE offers the advantage that the application of the train of refocusing RF pulses renders it insensitive to off-resonance effects [ALSOP1997]. Single-shot RARE runs the caveat of being prone to blurring artifacts induced by PSF broadening which limits the effective spatial resolution. Diffusion weighting disturbs the CPMG condition in RARE which induces destructive interferences between even and odd echo groups. Strategies for the prevention of destructive interferences between even and odd echo groups come at the cost of a SNR loss.

By moving from a single-shot to a multi-shot RARE or EPI approach, images exhibiting higher spatial resolution can be obtained. This approach prolongs scan time and poses the challenge of increased motion sensitivity. Non-Cartesian k-space trajectories are less sensitive to shot-to-shot phase variations and have been favored over Cartesian k-space sampling for diffusion-weighted imaging. Projection reconstruction, also called radial techniques offer inherent 1D navigator phase correction since the k-space center is covered with each spoke [GLOVER1992]. Different versions of diffusion-weighted radial sequences have been applied for brain imaging [GMITRO1993, TROUARD1999, SEIFERT2000]. PROPELLER [PIPE1999] acquires a blade of k-space after each excitation using periodic refocusing RF pulses and offers inherent 2D navigator phase correction. A further advancement of this technique – Turboprop [PIPE2006] – features additional EPI acquisitions placed in between refocusing RF pulses of a RARE sequence. This approach offsets SAR constraints and reduces scan times.

It has been shown, that parallel imaging [SODICKSON1997, GRISWOLD1999, PRUESSMANN1999], segmented EPI [PORTER2009] and inner-volume EPI (zonal EPI, zoomed imaging [FEINBERG1985, MANSFIELD1988]) can reduce image distortions and increase the achievable spatial resolution in EPI images [JEZZARD2012]. A sophisticated segmented EPI technique was suggested for diffusion-weighted imaging. This approach combines readout-segmented EPI (rs-EPI) with a 2D navigator based reacquisition. It provides high spatial resolution diffusion-weighted images of the brain at 3.0 T and at 7.0 T with largely reduced susceptibility artifacts [PORTER2009, HEIDEMANN2010]. The reduced sensitivity to geometric distortions results from the significant reduction in duration of the readout gradient due to the small coverage of k_x for each shot. The echo spacing is drastically reduced so that susceptibility and T_2^* effects are significantly decreased. Furthermore, the total echo train length is shortened which is supported by parallel imaging based undersampling strategies.

2.4.3 Diffusion sensitization parameters

In addition to the type of data readout, the diffusions sensitization preparation experiment can be customized to mitigate off-resonance effects and image distortion. The design of the diffusion sensitizing gradients determines sequence timing and the b-value, i.e. the degree of diffusion weighting.

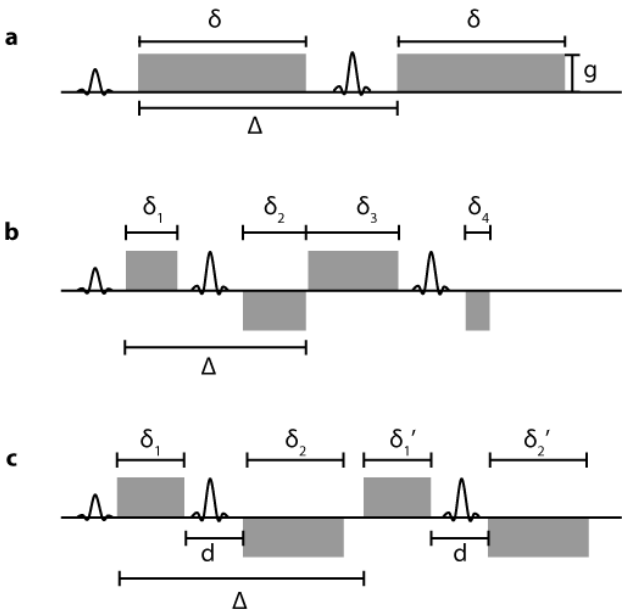

Figure 17: **Diffusion sensitization schemes**
(a): Standard Stejskal-Tanner diffusion sensitization gradients [STEJSKAL1965], **(b):** TRSE scheme proposed to reduce the sensitivity to eddy currents with $\delta_1+\delta_2 = \delta_3+\delta_4$ [FEINBERG1990, REESE2003] and **(c):** a modified TRSE scheme compensating eddy currents of different time constants with $\delta = \delta_1+\delta_2 = \delta_1'+\delta_2'$ [FINSTERBUSCH2010].

The standard Stejskal-Tanner diffusion preparation (Figure 17a) provides highly efficient diffusion weighting without extensively prolonging the echo time. Due to the two large sensitization gradients and the long diffusion time, the imaging sequence becomes sensitive to motion and eddy current distortions. Alternatively, bipolar gradients can be incorporated to reduce the sensitivity to motion [HONG1992]. A twice refocused spin echo (TRSE) diffusion sensitization gradient scheme has been proposed to reduce eddy current induced distortions [FEINBERG1990, REESE2003] (Figure 17b). Recently, a modified TRSE scheme was proposed ([FINSTERBUSCH2010], Figure 17c), that compensates for eddy currents of different time constants. The latter two approaches are outlined here since the ss-RARE and ss-EPI variants used as reference methods in this thesis feature those diffusion sensitization schemes.

The b-value for the TRSE scheme and the modified TRSE design is calculated according to equations [47] and [48]. In equation [47] the first and the third term take the weighting induced by the first two gradients into account while the second and the fourth term link all single gradients. For the modified TRSE scheme the first and third as well as the second and fourth gradient are identical. The first term in equation [48] represents the weighting of each of the two pairs of gradients ($\delta = \delta_1+\delta_2 = \delta_1'+\delta_2'$) while the second and the third term take their interference into account. Alongside with the advantages of these more sophisticated diffusion sensitization designs come some impediments. First, the preparation time and hence TE is prolonged since the individual gradients within the TRSE designs are longer versus the Stejskal-Tanner method to achieve a specific b-value. Second, concomitant gradient fields caused by asymmetric diffusion sensitization gradients surrounding refocusing RF pulses can occur and may lead to extra phase accruals that corrupt the data.

$$b = \gamma^2 g^2 \left[\delta_1^2(\Delta - \delta_2 - \delta_1) + (\delta_1 + \delta_2 - \delta_3)^2(\Delta - \delta_4 - \delta_3) + \frac{2}{3}(\delta_1 + \delta_2)^3 - \frac{1}{3}(\delta_1 + \delta_2 - \delta_3 - \delta_4)^3\right] \quad [47]$$

$$b = \gamma^2 g^2 \left[\delta^2\left(\Delta - \frac{1}{3}\delta\right) + d(\delta_2^2 + \delta_2'^2) - 2d\delta\delta_2\right] \quad [48]$$

2.4.4 DWI applications

Today's most relevant clinical DWI application is the detection of acute ischemic stroke. It has been shown that ischemic regions in the brain show hyperintense signal on diffusion-weighted images. This manifests itself in a decreased ADC before any other MRI contrast or MRI parameter shows alterations [MOSELEY1990, WARACH1995]. In the aftermath of the acute ischemia the ADC increases and results in a slightly elevated ADC in the chronic state compared to healthy tissue. This ADC behavior helps to distinguish between acute and chronic infarction based on

diffusion-weighted images. Brain pathologies like intracranial masses, infections like herpes encephalitis or Creutzfeldt-Jakob disease, trauma and demyelination in the case of multiple sclerosis have been investigated using DWI [SCHAEFER2000]. DWI is not restricted to brain applications. Emerging applications include DWI of the heart and of the eye which are in the focus of this thesis.

In 1994, the first *in-vivo* diffusion-weighted images of the human heart obtained from stimulated-echo EPI were presented [EDELMAN1994]. Most of the following work on this topic focuses on DTI to reveal information about myocardial microstructure. Cardiac motion and myocardial strain are managed by adapting the diffusion gradient design, by using cardiac triggering and by adjusting the sequence timing [REESE1995, REESE1996, DOU2002, GAMPER2007]. DWI using low b-values has been applied to detect acute myocardial infarction (AMI) and to distinguish AMI from chronic myocardial infarction by exploiting ADC changes in edemas being only present in AMI [LAISSY2009, DEUX2011, RAPACCHI2011, KOCIEMBA2013]. Cardiac and respiratory motion causes tissue displacements on a macroscopic scale which are superimposed to the information of interest on a microscopic level. These physics related obstacles are aggravated by EPI related image artifacts so that the number of cardiac DWI studies is still very limited.

MRI of the spatial arrangements of the eye segments and their masses is an emerging application that is increasingly being used in basic research, (pre)clinical imaging, and diagnostic radiology [APUSHKIN2005, DE GRAAF2005, MAFEE2005, BERT2006, STRENK2006, MALHOTRA2011, ZHANG2011, BOLACCHI2012, DE GRAAF2012a, SEPAHDARI2012, ZHANG2012, BEENAKKER2013, GRAESSL2014a]. Ocular MRI holds the potential to provide guidance during the diagnosis and treatment of ophthalmological diseases [CLARK1999, WEIR2009, MALHOTRA2011, PAPADOPOULOU2012, PINELES2012, KHURANA2013, LENHART2014]. DWI has been put to clinical use for the assessment of endophtalmitis [RUMBOLDT2005], optic nerve infarction, and ischemia [CHEN2006, MATHUR2007]; for the differential diagnosis of orbital cellulitis, pseudotumor, and lymphoid lesions [KAPUR2009]; as well as for the assessment of treatment response in active graves orbitopathy [RITCHIE2014]. Diffusion-weighted imaging has also been valuable for the diagnosis of orbital abscesses [SEPAHDARI2009], characterization of retinoblastoma in pediatric patients [DE GRAAF2012b], differentiation between ocular tumors and retinal detachment [DE GRAAF2012b, SEPAHDARI2012, ERB-EIGNER2013], and the discrimination of benign from malignant ocular masses [SEPAHDARI2010, SEPAHDARI2012, SEPAHDARI2014].

3. Development of Simultaneous Dual Contrast Weighting Using Double Echo RARE Imaging

RARE imaging is frequently applied in clinical practice and biomedical research. RARE is commonly used for anatomical imaging, for the diagnosis of ischemic events and for the detection of edema including a range of neuro- [OSHIO1991, TIEN1992, NEEMA2009] and cardiovascular [SIMONETTI1996, ABDEL-ATY2004, GUTBERLET2006, VERHAERT2011] applications. T_2^*-sensitized RARE has been applied for first pass bolus perfusion imaging [NORRIS1993b], for functional brain mapping [NIENDORF1999] and for myocardial T_2^* mapping [HEINRICHS2009]. All these clinical applications are primarily limited to a single contrast weighting.

For reasons of speed and clinical utility, it is conceptually appealing to pursue imaging techniques that are sensitive to multiple contrast mechanisms and support simultaneous generation of two or more contrasts. A single-shot double-echo EPI sequence [BÖRNERT1994] was presented offering contrast manipulations for the two generated images by changing TE, TR or the mixing time (TM) in a three-pulse stimulated echo sequence in conjunction with two EPI readouts. The simultaneous assessment of T_2 and the apparent diffusion coefficient (ADC) by selecting different pathways in a multi-pulse experiment has also been suggested [FRANCONI1994, SONG2004, ONG2005]. Combining T_2 and PD contrast by dividing the echo train into two groups with short and long echo times has been reported [HIGUCHI1991]. Generating two or even more contrasts concurrently within one acquisition offers substantial reduction of measurement time. This is of benefit in a clinical scenario, but also in preclinical studies where multiple parameters are assessed using imaging protocols with tight spatiotemporal resolution constraints [POHLMANN2013b, POHLMANN2013a]. Moreover, simultaneous acquisition of multiple contrasts obviates the need for slice co-registration when combining multiple series of images with different contrast which would be beneficial for applications dealing with bulk or physiological motion such as cardiac MRI.

A RARE approach that combines simultaneously anatomical contrast (PD) and susceptibility weighting (T_2^*) has not yet been reported. Hence, the goal is to develop a RARE variant that affords simultaneous generation of two contrasts (PD and T_2^*). For this purpose the concept of echo displacement [NORRIS1992] is put to good use, with odd and even echo parities being separated from each other instead of discarding one parity. The proposed RARE variant is referred to two-in-one RARE (2in-RARE) for reasons of brevity.

Portions of this chapter were published in [FUCHS2014b] and [FUCHS2014a]. Driven by the motivation to combat speed constraints of today's clinical imaging the fundamental idea for the technique outlined in this chapter was developed completely independently as part of the studies on the basics of RARE. The basic theory of 2in1-RARE was worked out using the phase graph approach to track the evolution of magnetization throughout an RF refocused echo train. The idea to manage the spin echo and primary stimulated echo independently was introduced independently. All of the work and experiments necessary to demonstrate the basic feasibility of 2in1-RARE was performed independently. This included careful theoretical considerations, pulse sequence development and implementation on a clinical scanner, development and validation of the reconstruction software, point spread function assessment, collection of experimental data in phantoms and benchmarking of 2in1-RARE versus conventional RARE variants commonly used in today's clinical practice. As part of the project, the applicability of 2in1-RARE was examined for brain imaging including simultaneous acquisition of proton density and T_2^*-weighted images, T_2^* mapping of the brain and a FLAIR prepared version of 2in1-RARE. A patent application on the basic concept of 2in1-RARE was filed.

3.1 Development of novel methodology and pulse sequence design

The novel RARE variant, which is referred to two-in-one RARE (2in1-RARE), adopts the concept of echo displacement [NORRIS1992] and echo separation [SCHICK1997] by dividing odd and even echo parities and using both independently. During the reconstruction process, the two echo parities are dealt with independently to create two images: one consisting of pure spin echo magnetization and the second one comprising only stimulated echo magnetization. The EPG algorithm is applied to illustrate the essential echo pathways and to illustrate the basic principle of 2in1-RARE.

3.1.1 Pulse sequence diagram

The goal of 2in1-RARE (Figure 18a), namely the generation of two images with different contrast behavior, is achieved by several modifications with respect to the original RARE sequence [HENNIG1986].

First, the dephasing gradient along the frequency encoding direction is now unbalanced to separate the echo into two groups for each ESP which resembles the split-echo RARE approach [SCHICK1997]. Thus, two individual images can be reconstructed from one single acquisition. Second, additional gradients (marked in gray in Figure 18a) are applied along the frequency direction to perform pathway selection, i.e. to eliminate stimulated echoes which are generated

starting with the third refocusing RF pulse and which are designated as secondary stimulated echoes. This concept is related to the echo displacement [NORRIS1992]. In the original displaced RARE sequence the even (odd) echo group is acquired while the odd (even) group is discarded by using additional displacement gradients. The proposed 2in1-RARE variant does not distinguish between odd and even echoes but the type of each echo (echo family according to [NORRIS1992]), namely spin echo or stimulated echo. The third modification is the contrast manipulation of the SE part. In the current implementation, an evolution time τ is inserted after the first refocusing RF pulse to introduce T_2^* weighting to the SE magnetization. Because the part of magnetization which will later form a stimulated echo is stored along the longitudinal axis during this time period, it is not affected by the evolution time τ and therefore does not experience any T_2^* weighting.

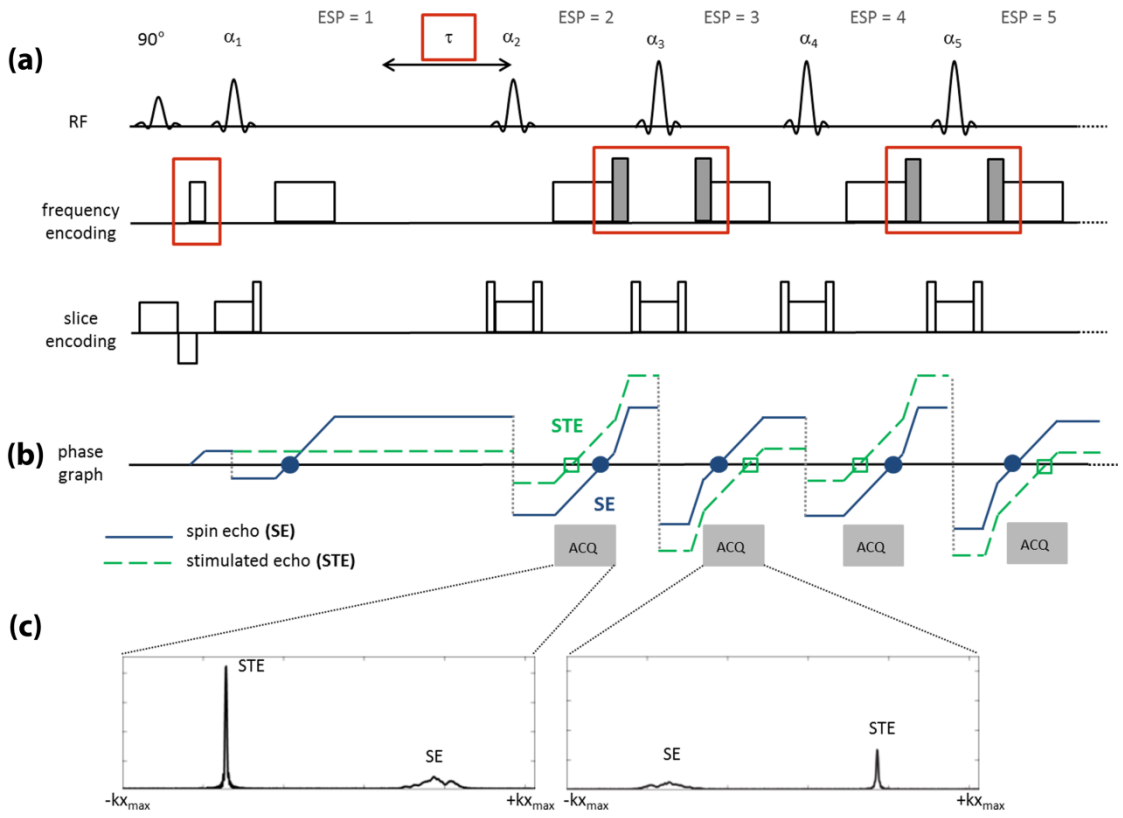

Figure 18: **2in1-RARE pulse sequence diagram**
(a): Basic scheme of the 2in1-RARE sequence showing the RF pulse train, the frequency encoding and the slice selection gradients. Phase encoding gradients are not depicted because the center-out phase encoding scheme was not altered with respect to coherent RARE. The modifications with respect to coherent RARE are marked in red: the unbalanced dephasing frequency encoding gradient, additional gradients (marked in gray) to shift secondary stimulated echoes out of the acquisition window and the evolution time τ in the first ESP to induce T_2^* weighting for SE magnetization. **(b):** The evolution of the magnetization is illustrated in the EPG together with the position of the acquisition windows. Only two pathways are shown: the primary spin echo (SE, blue solid line, filled circle) and the primary stimulated echo (STE, green dashed line, open square). **(c):** Data acquired without phase encoding is shown for the first two ESP [FUCHS2014b].

Magnetization pathways are shown in Figure 18b for the two important echo groups of 2in1-RARE. All other pathways are not shown for reasons of clarity. In comparison to the previously shown EPG diagrams, dephasing due to free precession is not visualized, since it is not the essential part of the 2in1-RARE mechanism. Frequency encoding gradients are crucial for echo separation and are therefore considered in the EPG. Basically, their effect is similar to what was described for free precession processes in the introduction of the EPG algorithm. Spin configurations in the transversal plane acquire a phase depending on the polarity and strength of the encoding gradient and are therefore depicted with rising lines. Magnetization stored along the longitudinal axis is not affected by the frequency encoding gradient field which is applied along the *x* axis. Therefore these pathways stay horizontal while the frequency encoding gradients are active. Since free precession and also longitudinal and transversal relaxation are not considered at this point, all pathways proceed horizontally, i.e. without acquiring any phase during periods where no encoding gradients are active.

One echo in the 2in1-RARE sequence is generated from the repeatedly refocused primary spin echo (blue line in Figure 18b). The second echo originates from the primary stimulated echo (green line in Figure 18b). Due to the omission of secondary stimulated echoes via the additional gradients in frequency encoding direction pure spin echoes and pure stimulated echoes can be separately acquired and individually prepared. Preferably, the magnetization is distributed equally between the SE and the STE. To achieve this balance, the flip angle of the first two refocusing RF pulses α_1 and α_2 needs to be adjusted. The intensities of the echoes SE and STE after the second refocusing RF pulse shown in Figure 18b are given by:

$$I_{SE} = I_0 \sin^2\frac{\alpha_1}{2}\sin^2\frac{\alpha_2}{2}\, e^{-\frac{ESP+\tau}{T_2}}\, e^{-\frac{ESP}{T_2}} \qquad [49]$$

$$I_{STE} = \frac{1}{2} I_0\, sin\alpha_1\, sin\alpha_2\, e^{-\frac{ESP+\tau}{T_1}}\, e^{-\frac{ESP}{T_2}} \qquad [50]$$

These equations are based on the discussion of arbitrary flip angle RF pulses (summarized in Table 2 on page 21) but include relaxation terms. I_0 is a constant depending on spin density, the initial transverse magnetization after the excitation RF pulse, and the MR systems hardware fidelity. Following equations [49] and [50], the ratio I_{STE}/I_{SE} equals one if $\alpha_1 = \alpha_2 = 110°$, assuming $T_1 = 1000$ ms and $T_2 = 80$ ms (Figure 19). Because secondary stimulated echoes are not acquired to avoid contamination of the pure spin echoes and pure stimulated echoes, refocusing RF pulse angles should be ideally 180° starting with α_3. This way, signals from secondary stimulated echoes are minimized and only a minor part of available magnetization is excluded from the acquired signal.

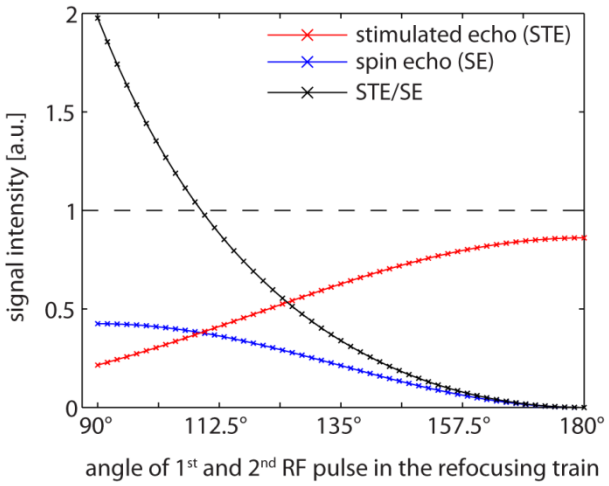

Figure 19: **Flip angle dependence of SE and STE for 2in1-RARE**
Signal intensities of the stimulated echo (red) and the spin echo (blue) after the second refocusing RF pulse in 2in1-RARE. The ratio STE/SE is shown in black. For $\alpha_1 = \alpha_2 = 110°$ the ratio equals one.

3.1.2 Phase correction

By means of the described modifications, 2in1-RARE generates two echoes per ESP originating from different echo families. Figure 18b and Figure 18c illustrate that the SE and the STE change their position with respect to the center frequency from one ESP to the next one. To reconstruct two images with different contrasts, the echoes need to be assigned to two k-space data sets: k-space$_{SE}$ and k-space$_{STE}$. By doing this, even and odd parity echoes are mixed since SE as well as STE alternately possess even or odd parity (compare Figure 15 on page 23). In case of fulfilled CPMG condition, i.e. the B_1 vector of the refocusing RF pulses is parallel or antiparallel to the initial transverse magnetization, echoes from odd and even parity add coherently, meaning they exhibit no phase difference. 2in1-RARE, being sensitive to B_0 inhomogeneities due to the inserted evolution time τ, the CPMG condition is no longer met resulting in a phase difference accrual between the two off-center echo groups [NORRIS1993a]. To avoid image artifacts when mixing odd and even echoes phase correction needs to be performed. The phase correction scheme used builds on schemes previously published for diffusion-weighted RARE imaging [ANDERSON1994, ORDIDGE1994, WAN1995, WILLIAMS1999].

For this purpose, data without phase encoding were acquired within one dummy cycle before the actual data acquisition, delivering a set of reference data containing one data line for each ESP. First, the imaging data and the reference data are inversely Fourier transformed along the frequency encoding direction to obtain the corresponding projection.

A point-by-point multiplication then delivers the corrected data set.

$$S_{corr} = S_{uncorr} \cdot e^{-angle(S_{ref})} \quad [51]$$

In doing so, it is important to choose the reference line according to the ESP number of the imaging data line.

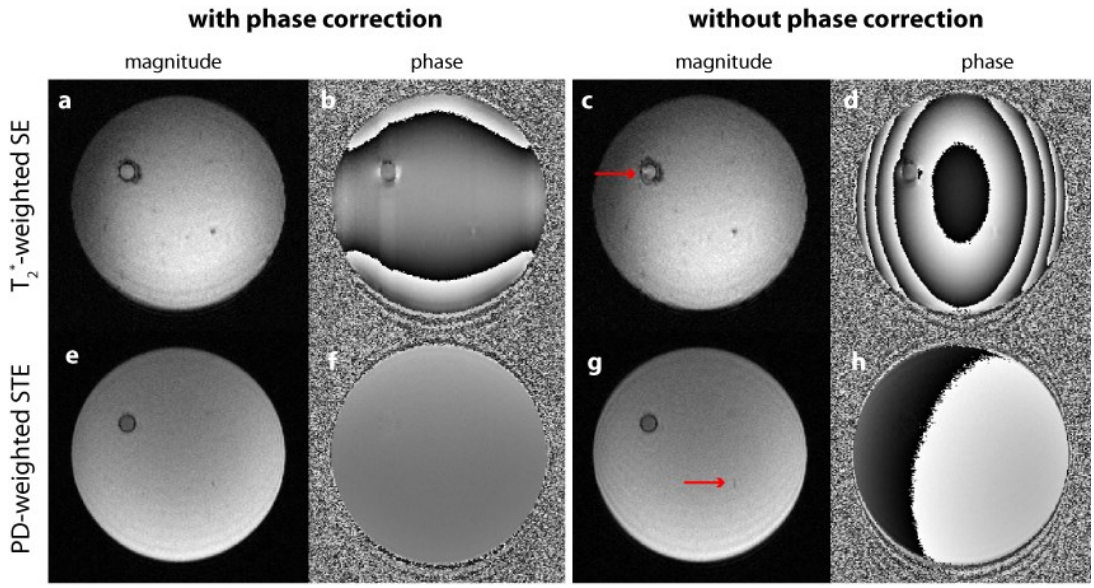

Figure 20: **Effect of the phase correction in phantom images**
T_2^*-weighted SE and PD-weighted STE magnitude and phase images reconstructed with phase correction are shown in the left part. The corresponding images reconstructed without phase correction are depicted in the right panel. Image artifacts due to phase errors between even and odd parity echoes are marked by red arrows.

The need and impact of phase correction is illustrated in Figure 20c,g using magnitude phantom images. If no phase correction is used imaging artifacts occur in the areas marked by red arrows. Large variations across the whole phantom are visible in the corresponding phase images (Figure 20d,h). Phase correction smoothens the phase across the data set (Figure 20b,f) and results in magnitude images free of phase related image artifacts (Figure 20a,e). Similar effects can be observed in *in-vivo* images. Especially regions containing subtle anatomical structures like small vessels are prone to phase related artifacts (red arrows in Figure 21) and demonstrate the added value of phase correction within 2in1-RARE.

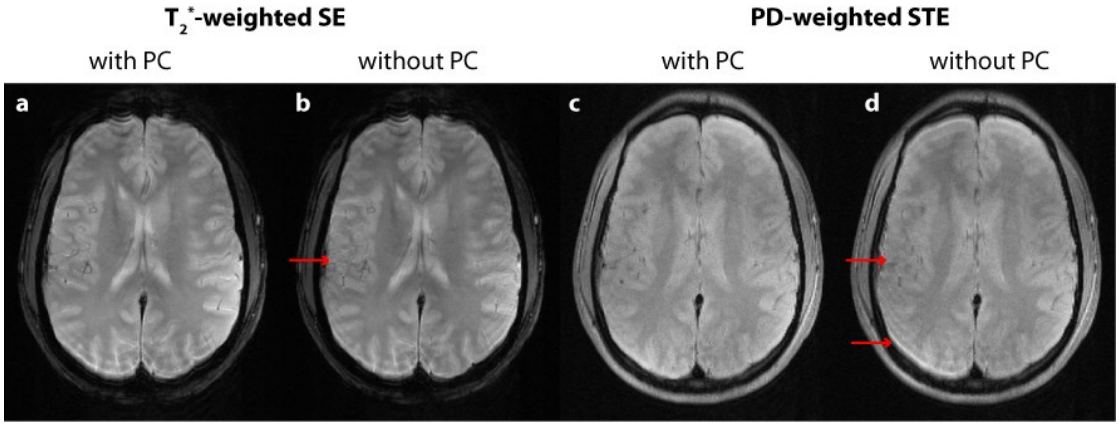

Figure 21: **Effect of the phase correction in *in-vivo* brain images**
PD-weighted STE (**a**,**b**) and T_2^*-weighted SE (**c**,**d**) images of a slice placed parallel to the anterior commissure - posterior commissure (AC-PC) line are shown with and without phase correction. Imaging parameters were: TR = 4000 ms, TE = 25 ms, ESP = 12 ms, ETL = 7, receiver bandwidth = 476 kHz, acquisition matrix = 1024x512, FoV_{read} = 250 mm, slice thickness = 5 mm, τ = 15 ms. Phase related image artifacts are marked by red arrows.

3.1.3 Data reconstruction

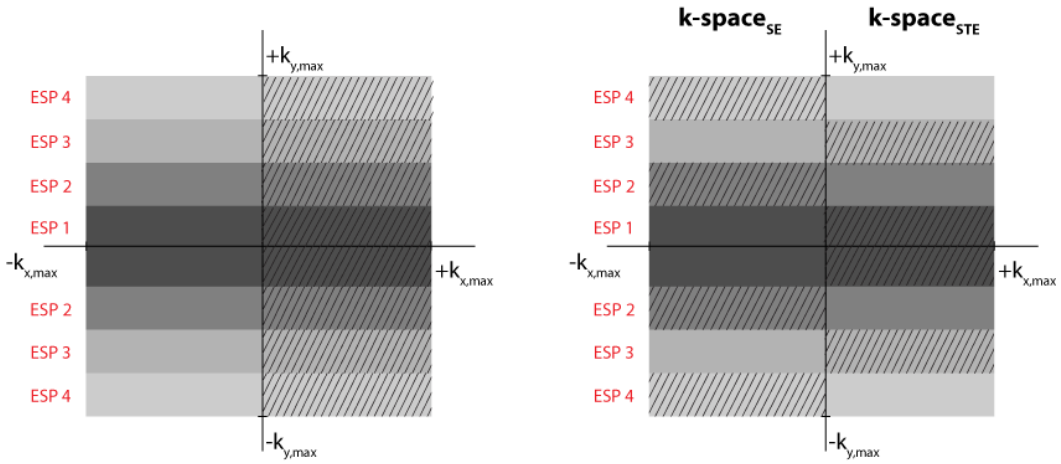

Figure 22: **Reshuffling of k-space for 2in1-RARE**
Different shades of gray code for data originating from different ESPs, demonstrating the center-out phase encoding scheme. Plain parts represent the half of data with $k_x \leq k_{x=0}$ (even parity) and the dashed part corresponds to $k_x > k_{x=0}$ (odd parity). **Left:** The original k-space resulting from a 2in1-RARE acquisition contains echoes of four different types: SE_{odd}, SE_{even}, STE_{odd}, STE_{even}. **Right:** After reshuffling of all k-space lines SEs and STEs are separated and form two individual k-spaces.

For data reconstruction raw data are transferred from the MR scanner to a MATLAB workstation and processed offline. The reconstruction algorithm halves the k_x dimension of the k-space at the center frequency and performs zero filling to restore the original matrix size for SE and STE data with respect to coherent RARE. Since SE and STE alternate their position in the acquisition window with respect to the center frequency from one ESP to the next one, reshuffling of the original k-

space is necessary. Reshuffling creates one k-space which only contains echoes originating from the primary spin echo (k-space$_{SE}$) and a second k-space which comprises refocused magnetization of only the primary stimulated echo (k-space$_{STE}$) (Figure 22).

For further reconstruction, both k-spaces are processed separately. After phase correction, inverse Fourier transformation along the phase encoding direction delivers two final images with different contrast.

The reconstruction algorithm requires only one to two seconds on a standard dual core desktop computer. This speed offers the opportunity to integrate the reconstruction algorithm into the image reconstruction system of the MR scanner to obtain the images online.

3.1.4 Further image contrast possibilities

The strict separation of SE and STE magnetization within the 2in1-RARE echo train offers further possibilities for contrast manipulation, that were not implemented within the scope of this thesis. While the STE magnetization is stored along the longitudinal axis in the first ESP, the SE part can be sensitized to diffusion. This requires periodic timing to avoid superimposed T_2^* weighting due to non-rephased phase accrual caused by B_0 inhomogeneities. One possible pulse sequence design for simultaneous generation of an anatomical image (PD- or T_2-weighted) and a diffusion-weighted image is shown in Figure 23. This approach would be of particular interest for stroke imaging, where DWI is the standard diagnostic tool. With the proposed 2in1-RARE approach, anatomical (PD- or T_2-weighted) and functional (diffusion-weighted) information would be available simultaneously.

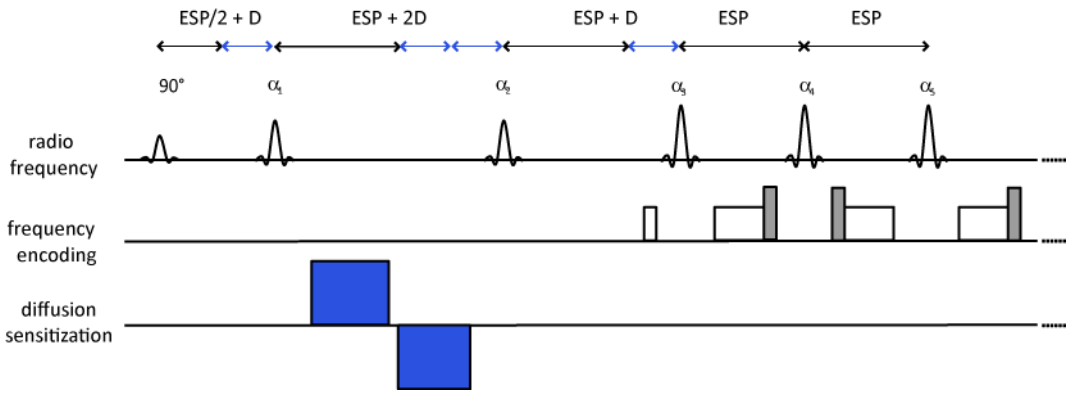

Figure 23: **Diffusion weighting within 2in1-RARE**
The timing of the pulse sequence is modified to facilitate the incorporation of diffusion sensitization gradients. To ensure periodic timing, a constant time D is inserted after the excitation RF pulse and in the second ESP, two times D is inserted in the first ESP. Thus, dephasing due to B_0 inhomogeneities is fully rephased and hence the data is not falsified by T_2^* effects. A pair of diffusion gradients (marked in blue) can be inserted in the first ESP along all three spatial axes.

In another implementation, 2in1-RARE affords the generation of two different T_2^* contrasts for the SE and STE images by inserting an evolution time τ_1 after the excitation RF pulse and τ_2 after the first refocusing RF pulse. As a result, the overall T_2^* sensitization time is τ_1 for the STE magnetization and $(\tau_1 + \tau_2)$ for the SE part. This enables the acceleration of RARE based T_2^* mapping which offers distortion free images versus GRE based T_2^* mapping techniques. Furthermore, flow sensitive bipolar gradients can be applied while the STE magnetization is stored along the longitudinal axis to encode for velocity of the SE part using the timing scheme visualized in Figure 23 but replacing the diffusion sensitization gradients by flow sensitization gradients.

3.2 Implementation and validation in phantom experiments

The applicability of 2in1-RARE was carefully examined in phantom studies before moving to *in-vivo* imaging as part of this project. For this purpose, phantom images obtained with 2in1-RARE as well as split-echo RARE techniques were evaluated including SNR and image quality assessment. Susceptibility weighting within 2in1-RARE was benchmarked against split-echo T_2^*-weighted RARE imaging and conventional multi-echo GRE imaging. Point spread function (PSF) assessment was performed for 2in1-RARE and split-echo RARE techniques to obtain a quantitative measure for image quality.

All phantom experiments described in this chapter were performed in a $CuSO_4$ doped cylindrical agarose phantom (diameter = 15 cm) including a water tube (inner diameter = 5 mm) and a small capillary filled with air (inner diameter = 0.5 mm) to induce microscopic susceptibility gradients. Relaxation parameter measurements in a region of interest not including any of the described structures resulted in $T_1 \approx 80$ ms (inversion recovery spin echo sequence with 9 inversion times (TI) ranging from 25 ms to 1600 ms) and $T_2 \approx 40$ ms (multi TE spin echo sequence with 32 echo times TE ranging from 7.5 ms to 240 ms).

3.2.1 Signal-to-noise ratio evaluation

SNR was calculated for 2in1-RARE with τ = 0 ms and τ = 15 ms including the SE image and the STE image. For comparison, SNR was determined in split-echo RARE images. Table 3 summarizes the SNR obtained for 2in1-RARE versus the split-echo RARE approaches. For 2in1-RARE with τ = 0 ms, SNR obtained for the SE image accords with SNR derived from the STE image, confirming that two images with equal intensity are generated by the pulse sequence. Equivalence in SNR of SE and STE also demonstrates that the nominal flip angle of the first two refocusing RF pulses α_1 and α_2 of 130° was chosen properly to balance the ratio between the two magnetization pathways. Inserting an evolution time τ of 15 ms into 2in1-RARE results in a clear SNR decrease for the T_2^*-weighted

SE image which is in the same range as the decrease for the T_2^*-weighted split-echo RARE image. The SNR reduction of approximately 20% obtained for the STE image is due to the short T_1 relaxation time ($T_1 \approx 80$ ms) of the phantom, by which T_1 relaxation during the mixing time reduces the signal. For tissue with longer relaxation times, e.g. brain tissue with $T_1 \approx 1$ s, the T_1 relaxation contribution during the evolution time of 15 ms is less than 1%, and hence it is fair to neglect T_1 effects for *in-vivo* imaging.

Table 3: **Comparison of SNR**
Mean SNR ($\pm$ standard deviation) obtained from phantom images are given for the analyzed methods.

Method		SNR	
split-echo RARE		54.8 ± 4.6	
2in1-RARE τ = 0 ms	SE/STE	57.2 ± 5.9	58.6 ± 4.9
2in1-RARE τ = 15 ms	SE/STE	36.3 ± 3.9	48.3 ± 4.1
split-echo RARE τ = 15 ms		31.6 ± 1.9	

3.2.2 Qualitative image assessment

Figure 24 shows proton density and T_2^*-weighted phantom images obtained with 2in1-RARE at 3.0 T. For comparison, images derived from split-echo RARE are depicted. PD-weighted (Figure 24a) and T_2^*-weighted data (Figure 24c) were acquired simultaneously within one acquisition using 2in1-RARE. Hence, this approach offers a speed gain of factor two over coherent RARE and split-echo RARE and helps to obviate the need for a second scan. The T_2^*-weighted images show a signal decrease at interfaces exhibiting microscopic susceptibility gradients. Despite the different signal composition of 2in1-RARE and split-echo RARE, PD-weighted and T_2^*-weighted images derived from the novel and the traditional approach are in accordance.

A comparison between 2in1-RARE with split-echo RARE results revealed artifacts along the phase encoding direction for 2in1-RARE presenting themselves as ring-like repetition of the phantom boundary within the image (Figure 24a,c). One reason for the artifacts might be the fast signal decay within the echo train due to the elimination of stimulated echoes. In the phantom with relatively short T_2 of about 40 ms and its sharp boundaries this effect is pronounced. For the *in-vivo* situation with soft tissue boundaries and moderate T_2 relaxation times the effect is less pronounced so that the artifacts are barely visible. Furthermore, these images were acquired with a proof-of-principle implementation of 2in1-RARE exhibiting a relatively long ESP of 12 ms which presents an elongated period for T_2 decay within the echo train. The ESP can be reduced by using shorter RF pulses which would further reduce the mentioned artifact. Beside the described minor

artifact, the image quality of 2in1-RARE is comparable to the one achieved with split-echo RARE approaches.

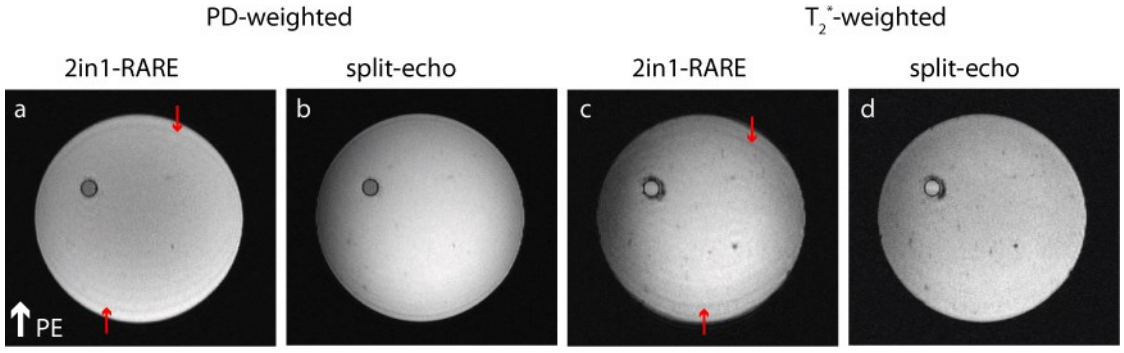

Figure 24: **2in1-RARE phantom images**
Phantom images obtained at 3.0 T comparing 2in1-RARE with the split-echo RARE approach. PD-weighted images deduced from 2in1-RARE (**a**) and split-echo RARE (**b**) are shown in the left part. T_2^*-weighted images using an evolution time of τ = 15 ms derived from 2in1-RARE (**c**) and T_2^*-weighted split-echo RARE (**d**) are depicted in the right part of the figure. The two images in (a) and (c) were acquired within one acquisition using 2in1-RARE, whereas (b) and (d) required two independent measurements. This resulted in a speed gain of factor two for 2in1-RARE. Artifacts along the phase encoding direction are marked with red arrows.

3.2.3 T_2^* weighting within 2in1-RARE

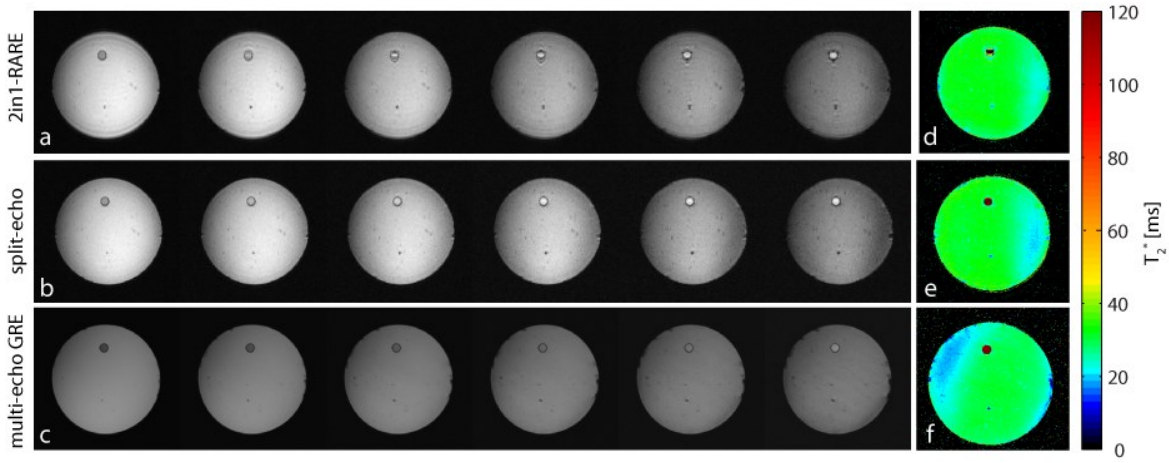

Figure 25: **Comparison of different T_2^* mapping techniques**
(**a**) Series of T_2^*-weighted images obtained with 2in1-RARE employing evolution times τ ranging from 5 ms to 30 ms. (**b**) T_2^*-weighted images resulting from split-echo RARE imaging using the same τ values as for the series in (a). (**c**) Multi-echo GRE images with TE ranging from 4.84 ms to 33.9 ms. (**d**)-(**f**) T_2^* maps resulting from the data in (a)-(c).

For the purpose of the validation of susceptibility weighting within the novel 2in1-RARE variant, a series of measurements with different evolution times τ ranging from 0 ms to 50 ms was performed using 2in1-RARE and T_2^*-weighted split-echo RARE. T_2^* maps were generated by fitting the data points to a mono exponential decay. For 2in1-RARE only the SE images were employed

for the analysis since no T_2^* weighting is applied for the STE images. For comparison, T_2^* mapping was conducted with a two-dimensional (2D) multi-echo gradient echo (GRE) technique using equidistant TEs ranging from 2.42 ms to 33.9 ms. Figure 25 summarizes the results of these experiments, showing a series of images with increasing T_2^* weighting together with the corresponding T_2^* map for each approach. Since multi-echo GRE imaging is regarded as the standard method for T_2^*-weighted imaging, it was set as a reference. Previous reports showed a good agreement between RARE based and multi-echo GRE T_2^* mapping [HEINRICHS2009]. Table 4 summarizes the results obtained for the validation of 2in1-RARE. The standard deviation of the mean value obtained in a 2cm circular ROI in the center of the phantom is 30% higher for the RARE based methods compared to the GRE approach. A reason for this might be a stronger sensitivity to B_1^+ inhomogeneities of spin echo sequences. The T_2^* map in Figure 25f underlines the advantages of RARE based T_2^* mapping methods versus GRE based techniques: The lower T_2^* relaxation times at the borders of the phantom result from poor B_0 homogeneities, an effect that is further pronounced at higher magnetic field strengths. Subsequently, the mean value calculated from the whole axial slice of the phantom is reduced for the GRE approach while the standard deviation is in the same range as for the RARE based methods. Beside these considerations the agreement between the T_2^* relaxation times obtained with 2in1-RARE and T_2^*-weighted split-echo RARE is the most important result of the validation experiments since it demonstrates the correct susceptibility weighting in 2in1-RARE and paves the way for further examinations.

Table 4: **Comparison of T_2^* relaxation times obtained from phantom imaging**
Mean T_2^* ($\pm$ standard deviation) obtained in a ROI covering the whole axial slice of the phantom and in a 2cm circular ROI in the center of the slice are compared for different methods.

Method	T_2^* [ms]	
	whole slice	2cm ROI
2in1-RARE	31.2 ± 8.9	32.1 ± 1.2
T_2^*-weighted split-echo RARE	30.8 ± 13.8	31.0 ± 1.3
multi-echo GRE	29.1 ± 13.5	30.0 ± 0.8

3.2.4 Point spread function assessment

The PSF is defined as the response of a linear and invariant imaging system to the input of an ideal point [ROSSMANN1969]. The initial point source will be blurred after passing through the imaging system (Figure 26). The smeared result – the PSF – gives information about the effective spatial resolution. The larger the PSF, the worse is the image effective spatial resolution and consequently the image sharpness.

Two criteria are important for PSF and image quality: the full width at half maximum (FWHM) of the main peak of the PSF and the occurrence (number and amplitude) of side lobes. The effects of ETL, ESP and phase encoding order on the PSF have been studied thoroughly [CONSTABLE1992a, CONSTABLE1992b]. Methods for PSF sharpening during data acquisition and thereupon improving image quality have been described [THOMAS2004, CARMICHAEL2009]. The focus of the considerations here is first the measurement of the PSF and second the comparison of PSF obtained for 2in1-RARE with PSFs deduced from conventional RARE and from split-echo RARE.

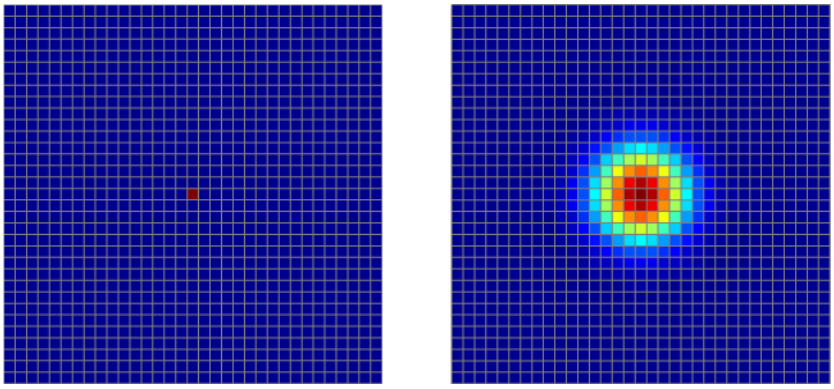

Figure 26: **Definition of the point spread function**
Ideal point which is to be imaged (**left**) and the initial ideal point after being reproduced by the imaging system (**right**) are depicted. The point is extended and blurred after being processed by the imaging system. Its underlying function is called the point spread function of the imaging system.

Figure 27a shows a k-space containing raw data acquired with coherent RARE with a matrix size $kx_{max} = 512$ and $ky_{max} = 184$. Further imaging parameters of this reference measurement were: TE = 30 ms, TR = 500 ms, ESP = 6.0 ms, ETL = 8. The corresponding k-space profile (Figure 27c) is generated by calculating the integral of every single k-space line ky with y ranging from 0 to ky_{max}. This k-space profile contains information about (i) the signal decay within the echo train due to T2 relaxation, (ii) the phase encoding ordering scheme and (iii) the phase encoding itself. To determine the PSF, the information (i) and (ii) are needed without being superposed by the phase encoding component (iii). Therefore, a measurement with the phase encoding gradients being turned off needs to be performed (Figure 27b). The effective k-space profile related to this k-space (Figure 27d) represents the filter which modulates the signal of each echo and comprises T_2 relaxation and the phase encoding scheme [CARMICHAEL2009]. The Fourier transformation (FT) of this k-space profile is the PSF.

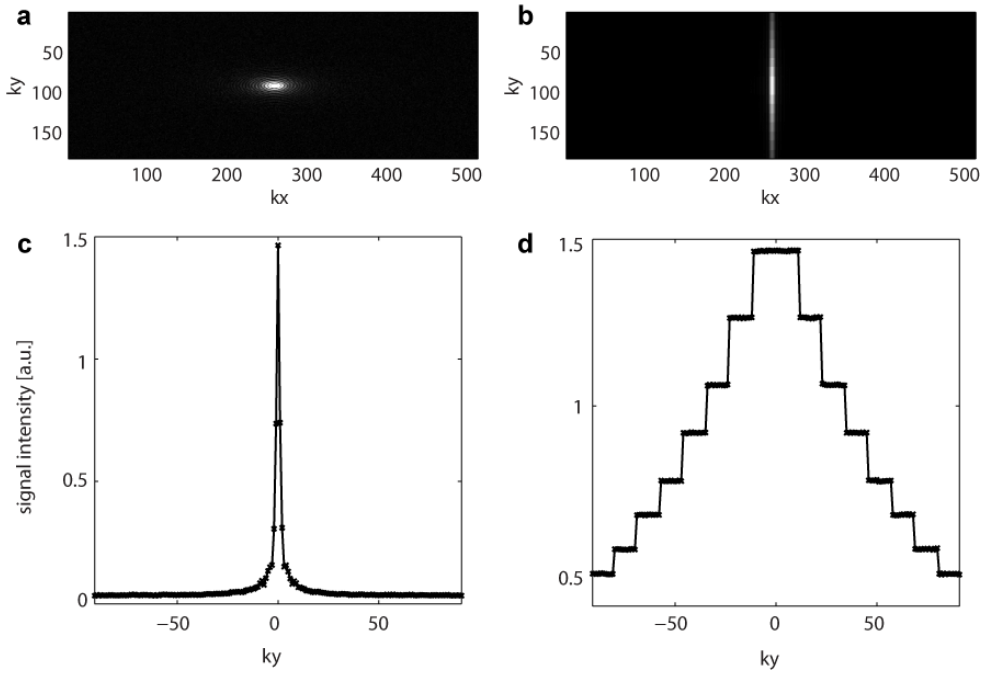

Figure 27: k-space profile

Raw data space (k-space) belonging to a standard coherent RARE measurement (**a**) and the corresponding k-space profile (**b**). k-space (**c**) and k-space profile (**d**) for the same measurement as in (a) and (c) with the phase encoding gradients turned off. Imaging parameters were: TE = 30 ms, TR = 500 ms, ESP = 6.0 ms, ETL = 8.

To clarify how the k-space profile reflects the above mentioned information, Figure 28b-d comprises three different k-space profiles resulting from measurements with one specific parameter changed with respect to the reference measurement shown in Figure 27d and Figure 28a. Prolonging the ESP (TE = 144 ms, TR = 500 ms, ESP = 28.8 ms, ETL = 8) concurrently increases TE_{eff} and results in a reduced amplitude and a faster decay of the k-space profile (Figure 28b). This is caused by increased T_2 decay between the refocusing RF pulses. The corresponding image (Figure 28f) exhibits very low signal for the $CuSO_4$ doped agarose (short T_2) phantom. The water compartment in the tube exhibits a long T_2 and provides strong signal. In case of an acquisition with the minimum TE_{eff} (Figure 28a) a centered phase encoding scheme is applied. For this scheme the first acquired echo in the refocusing train is stored in the k-space center, comprising the central k-space line with zero phase encoding. For a longer TE_{eff} (TE = 60 ms, TR = 500 ms, ESP = 6.0 ms, ETL = 8), the phase encoding is changed into a linear scheme so that a later echo is assigned to the central k-space line (Figure 28c). This changes the contrast in the image from PD-weighted (Figure 28e) to more T_2-weighted (Figure 28g). Figure 28d shows the k-space profile resulting from a measurement with only two excitations, i.e. a very long ETL (TE = 30 ms, TR = 1930 ms, ESP = 6.0 ms, ETL = 108) which results in a loss of the stepwise scheme of the k-space profile. The corresponding image exhibits T_2 blurring caused by the long echo train (Figure 28h).

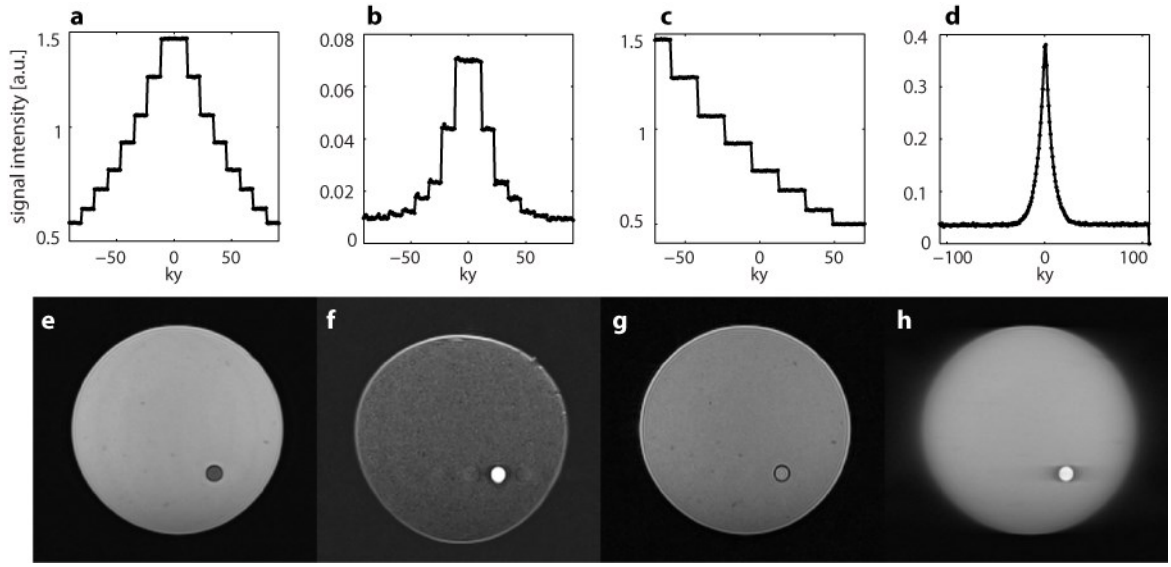

Figure 28: Effect of imaging parameters on the k-space profile and on corresponding images
k-space profiles (**a-d**) and corresponding images (**e-h**) for acquisitions with variable basic parameters. **a,e**: reference measurement: TE = 30 ms, TR = 500 ms, ESP = 6.0 ms, ETL = 8; **b,f:** prolonged ESP: TE = 144 ms, TR = 500 ms, ESP = 28.8 ms, ETL = 8; **c,g:** prolonged TE_{eff}: TE = 60 ms, TR = 500 ms, ESP = 6.0 ms, ETL = 8; **d,h:** TE = 30 ms, TR = 1930 ms, ESP = 6.0 ms, ETL = 8.

Degradation in image quality is reflected by a broadening of the PSF as it is demonstrated in Figure 29 for a comparison between the reference measurement (Figure 28a,e; blue curve) and the acquisition with the prolonged ETL (Figure 28d,h; red curve). This example shows how acquisition characteristics influence the k-space profile and hence the PSF and how this is linked to image quality: the broadened PSF results in a decreased effective spatial resolution of the image and the occurrence of blurring.

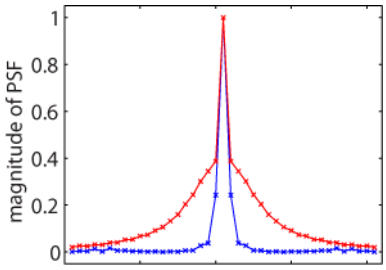

Figure 29: PSF broadening due to prolonged ETL
Normalized magnitude of the PSF for the reference measurement (blue line, TE = 30 ms, TR = 500 ms, ESP = 6.0 ms, ETL = 8) and for the acquisition with the prolonged ETL (red line, TE = 30 ms, TR = 1930 ms, ESP = 6.0 ms, ETL = 108).

The PSF formalism is put to use to assess image quality for 2in1-RARE versus coherent RARE and split-echo RARE. For this purpose phantom measurements were conducted with phase encoding gradients turned off. The top row of Figure 30 depicts the k-space profile for each approach, reflecting the signal intensity for every k_y-line. The corresponding PSF magnitude is shown in the

bottom row. k-space profile and PSF corresponding to coherent RARE are depicted in the first column (Figure 30a,f). Figure 30c illustrates the faster decay of the signal in the echo train of 2in1-RARE versus split-echo RARE (Figure 30b). This is due to the fact that secondary stimulated echoes are not included in 2in1-RARE. These occur since the refocusing RF pulses starting with α_3 are in fact defined with a nominal flip angle of 180°, but imperfections lead to smaller actual flip angles and hence these additional magnetization pathways and the resultant secondary stimulated echoes are generated. To maintain the pure spin echo and pure stimulated echo magnetization secondary stimulated echoes are omitted in 2in1-RARE. The overall signal is reduced resulting in the observed faster decay of the signal within the echo train. This manifests itself in a PSF broadening of approximately 15% (from 1.7 pixel to 2.0 pixel) for 2in1-RARE versus split-echo RARE as outlined in detail in Table 5. An evolution time τ = 15 ms results in a reduction of the main peak in the PSF from 0.9 to 0.3 for the SE part due to the faster signal decay induced by the T_2^* weighting as demonstrated in Figure 30d. This PSF alteration is equal to that of split-echo T_2^*-weighted RARE (Figure 30j). For the STE magnetization only a minor reduction caused by T_1 relaxation during the mixing time is observed which can be neglected for T_1 relaxation times prevalent in *in-vivo* tissue.

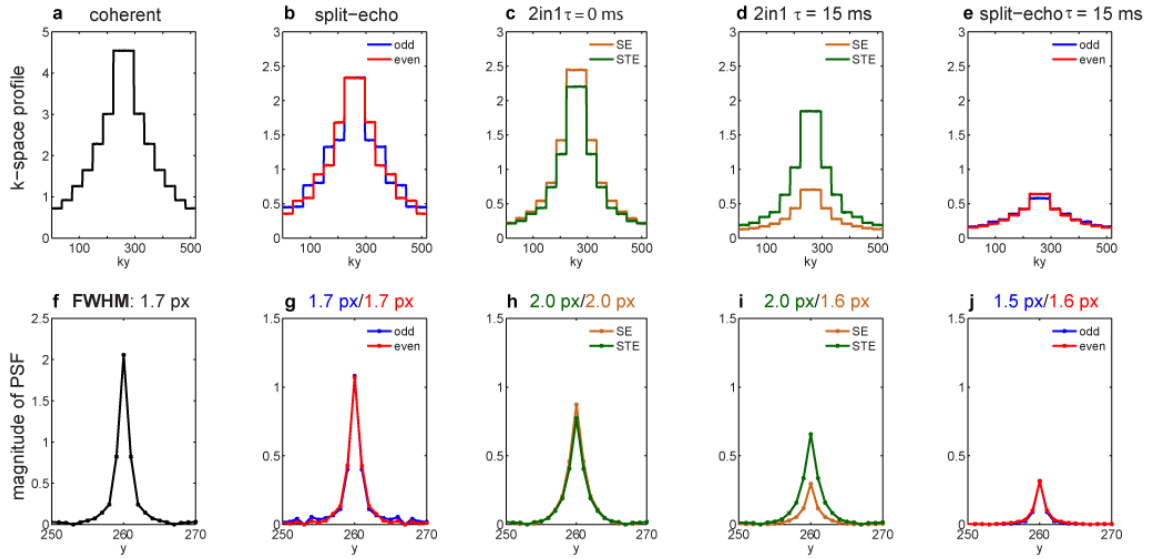

Figure 30: **PSF analysis for 2in1-RARE**

k-space profiles are depicted for coherent RARE (**a**), split-echo RARE (**b**), 2in1-RARE with τ = 0 ms (**c**), 2in1-RARE with τ = 15 ms (**d**), and split echo T_2^*-weighted RARE using an evolution time τ of 15 ms (**e**). **f-j**: The corresponding PSF for each approach is shown. For the split-echo RARE approaches, the profiles and PSFs are shown for the even (red) and the odd (blue) echo groups. SE (orange) and STE (green) curves are depicted for 2in1-RARE. The FWHM of the PSF in pixels (px) is noted as a measurement of quality [FUCHS2014b].

Table 5: **Comparison of PSF FWHM**
FWHM in pixel are given for coherent, split-echo and 2in1-RARE. For split-echo RARE odd and even echoes were reconstructed separately. In comparison, for 2in1-RARE the echo is divided into SE and STE parts.

Method	echo group	FWHM	
coherent RARE		1.7	
split-echo RARE	odd/even	1.7	1.7
2in1-RARE τ = 0 ms	SE/STE	2.0	2.0
2in1-RARE τ = 15 ms	SE/STE	1.6	2.0
split-echo RARE τ = 15 ms	odd/even	1.5	1.6

3.3 *In-vivo* proof-of-principle studies

The characteristics and performance of 2in1-RARE in phantoms paved the way for an *in-vivo* feasibility study at 3.0 T with the goal to examine the applicability of 2in1-RARE in healthy volunteers. To meet this goal split-echo RARE was used as a reference. Following the *in-vivo* study in healthy subjects 2in1-RARE was applied in multiple sclerosis (MS) patients to investigate the applicability of 2in1-RARE in a clinical scenario at 3.0 T.

3.3.1 Anatomical brain imaging in healthy volunteers

For the *in-vivo* feasibility study 10 healthy volunteers (mean age: (27 ± 2) years, 4 males, 6 females, mean BMI: (21.8 ± 2.7) kg/m^2) without any known history of disease were scanned. The study protocol comprised 2in1-RARE with an evolution time τ = 15 ms, split-echo RARE (τ = 0 ms) and T_2^*-weighted split-echo RARE (τ = 15 ms). The basic sequence parameters were kept the same for the three approaches to ensure a fair comparison: TR = 4000 ms, TE = 25 ms, ESP = 12 ms, ETL = 7, receiver bandwidth = 476 kHz, acquisition matrix = 1024x512, FoV_{read} = 250 mm, slice thickness = 5 mm. The TR of 4 s facilitated the acquisition of multiple slices and whole brain coverage. Specific absorption rate (SAR) did not constrain the number of slices for the given TR of 4 s resulting in an acquisition time of approximately 4 min for 14 slices. Figure 31 demonstrates that 2in1-RARE was performed successfully in each of the ten healthy volunteers. No major image artifacts are present in the PD-weighted STE images and T_2^*-weighted SE images which were acquired simultaneously with 2in1-RARE. The ring-like artifact observed in phantom images did not occur for the *in-vivo* scenario due to longer T_2 relaxation times in the brain and less sharp tissue boundaries. During the measurement of volunteer VIII the flip angle of the first two refocusing RF pulses (α_1 and α_2) was not adjusted properly, resulting in reduced signal in the

PD-weighted STE image. Beside this particular case, the ratio between SE and STE was balanced for all other volunteers.

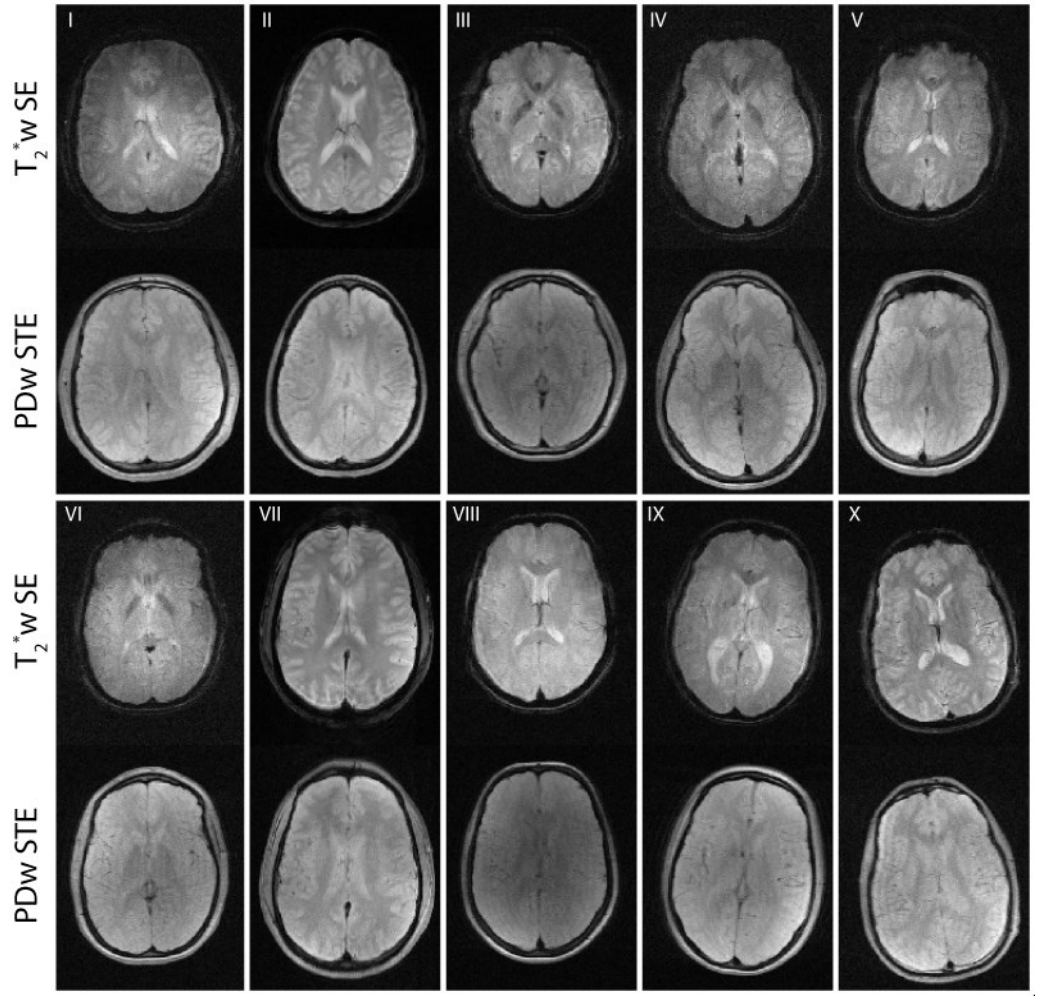

Figure 31: **Survey of the results obtained by the *in-vivo* feasibility study**
The T_2^*-weighted SE image and the PD-weighted STE image are shown for all ten volunteers. These two images are acquired simultaneously in each case.

One exemplary dataset (volunteer I in Figure 31, different slice) is depicted in more detail in Figure 32 and compared to PD and T_2^*-weighted split-echo RARE. Zoomed views of a temporal (I) and occipital (II) region of the depicted brain slice are shown. The magnified views demonstrate the capability of 2in1-RARE to depict subtle anatomical structures such as small vessels with the same fidelity as the split-echo RARE approaches. The images shown in Figure 32a and c were acquired simultaneously while the images presented in Figure 32b and d required two separate acquisitions which underscores the speed advantage of 2in1-RARE over the conventional split-echo RARE approach.

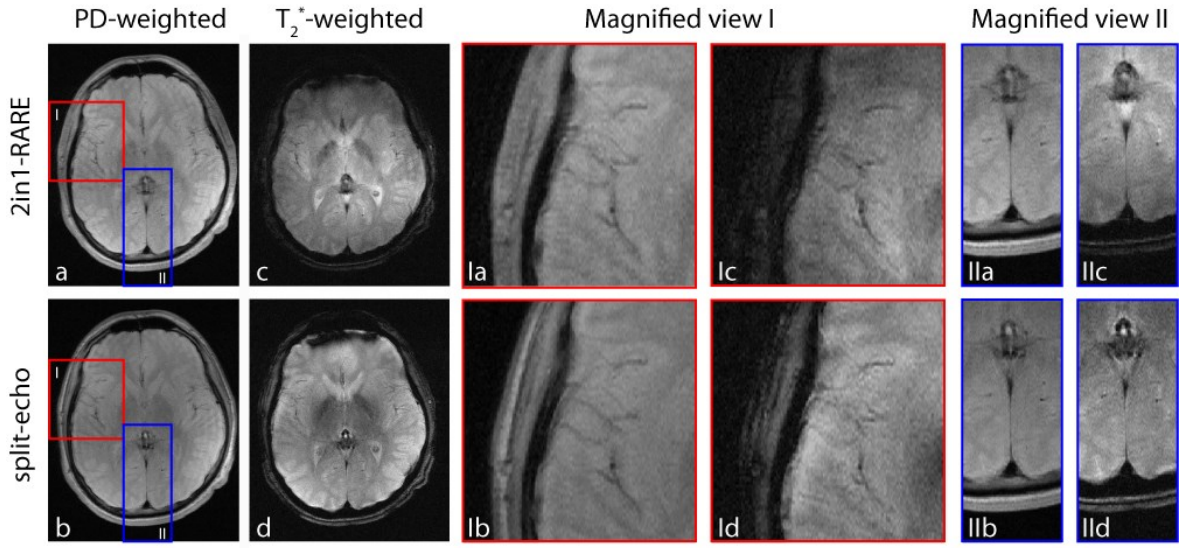

Figure 32: Comparison of *in-vivo* 2in1-RARE with split-echo RARE data for a healthy volunteer at 3.0 T
For each approach one single slice out of eight acquired slices is shown. PD-weighted images acquired with 2in1-RARE (**a**) and split-echo RARE (**b**) are shown as well as T_2^*-weighted images using an evolution time of τ = 15 ms obtained by 2in1-RARE (**c**) and T_2^*-weighted split-echo RARE (**d**). The data sets in (a) and (c) were acquired within one acquisition using 2in1-RARE, whereas (b) and (d) required two independent measurements. Magnified views of ROI I (marked in red) and ROI II (marked in blue) are shown on the right side. The magnified views demonstrate the ability of 2in1-RARE to image subtle anatomical structures that compare very well with those from split-echo RARE [FUCHS2014b].

To examine the applicability of cerebrospinal fluid (CSF) suppression in conjunction with 2in1-RARE, a Fluid Attenuated Inversion Recovery (FLAIR) preparation module was applied. Assuming T1 = 4200 ms for CSF at 3T TI was set to 1530 ms to null signal from the CSF according to [RYDBERG1995]:

$$TI_{null} = T_1 \left[ln2 - \ln(1 + e^{\left(-\frac{(TR-TE)}{T_1}\right)} \right] \qquad [52]$$

PD-weighted and T_2^*-weighted images acquired with 2in1-RARE in conjunction with a FLAIR preparation module – which might be instrumental to reduce partial volume effects in T_2^*-weighted imaging/T_2^* mapping of grey matter – are depicted in Figure 33. The suppression of CSF is clearly recognizable and the dynamic range of the image is not dictated by the high signal intensity of CSF anymore.

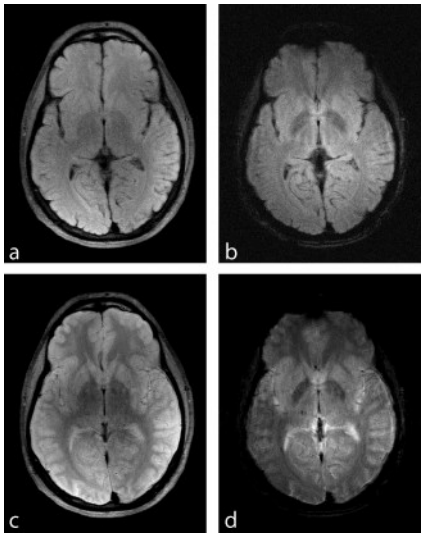

Figure 33: **2in1-RARE in conjunction with a FLAIR preparation module**
In-vivo brain images of a healthy volunteer acquired at 3.0 T with 2in1-RARE in conjunction with a FLAIR preparation module to suppress CSF signal showing one of fourteen acquired slices. The PD-weighted image reconstructed from STE magnetization **(a)** is shown together with the T_2^*-weighted image derived from the SE part **(b)**. Both images were obtained within one acquisition. Spatial resolution is (0.5 x 0.5 x 5.0) mm^3. For comparison, the corresponding images without the FLAIR preparation module are shown in **(c)** and **(d)** [FUCHS2014b].

3.3.2 T_2^* mapping of the brain with dual contrast RARE

T_2^* mapping using 2in1-RARE was performed in one volunteer to demonstrate the basic feasibility. For this purpose 13 evolution times τ ranging from 0 ms to 40 ms (equidistant increment of τ = 2.5 ms for τ = 0 ms to τ = 25 ms plus τ = 30 ms and τ = 40 ms) were employed for eight axial slices of the brain. T_2^* relaxation maps were calculated from the SE images derived from 2in1-RARE using a fit to a mono-exponential decay. The STE images which were simultaneously derived from 2in1-RARE were averaged to generate a high SNR anatomical image.

Figure 34a shows T_2^*-weighted images resulting from 2in1-RARE that were reconstructed from the SE magnetization for evolution times τ = 0-30 ms using an equidistant increment of τ = 5 ms plus τ = 40 ms. The T_2^* map generated from this series of T_2^*-weighted data is depicted in Figure 34b. For liquor an averaged T_2^* of (136 ± 38) ms was observed. ROI analysis within grey and white matter revealed $T_{2\,\text{grey matter}}^* = (42 \pm 7)$ ms and $T_{2\,\text{white matter}}^* = (45 \pm 5)$ ms. These results are 35% lower for grey matter and 15% lower for white matter in comparison to previously published T_2^* relaxation times obtained by gradient echo based imaging at 3.0 T [PETERS2007]. The proof-of-principle character of the data presented here might explain the underestimation of T_2^* versus the sophisticated reference study which provided a detailed comparison of T_2^* relaxation times at 1.5 T, 3.0 T and 7.0 T. An anatomical image resulting from the average of all STE images is shown in

Figure 34c. Signal-to-noise ratio analysis yielded a SNR of 74.4 ± 4.8 for the right thalamus and SNR = 76.6 ± 4.5 for the left thalamus with both regions representing grey matter tissue. A SNR of 69.8 ± 3.3 was observed for the splenium corpus callosum and SNR = 67.2 ± 3.1 for the genu corpus callosum, both exemplifying white matter. Whole brain SNR was determined to be 66.4 ± 11.2. The total acquisition time of 50 min in this proof of principle experiment can be shortened by using acceleration techniques [FENG2011].

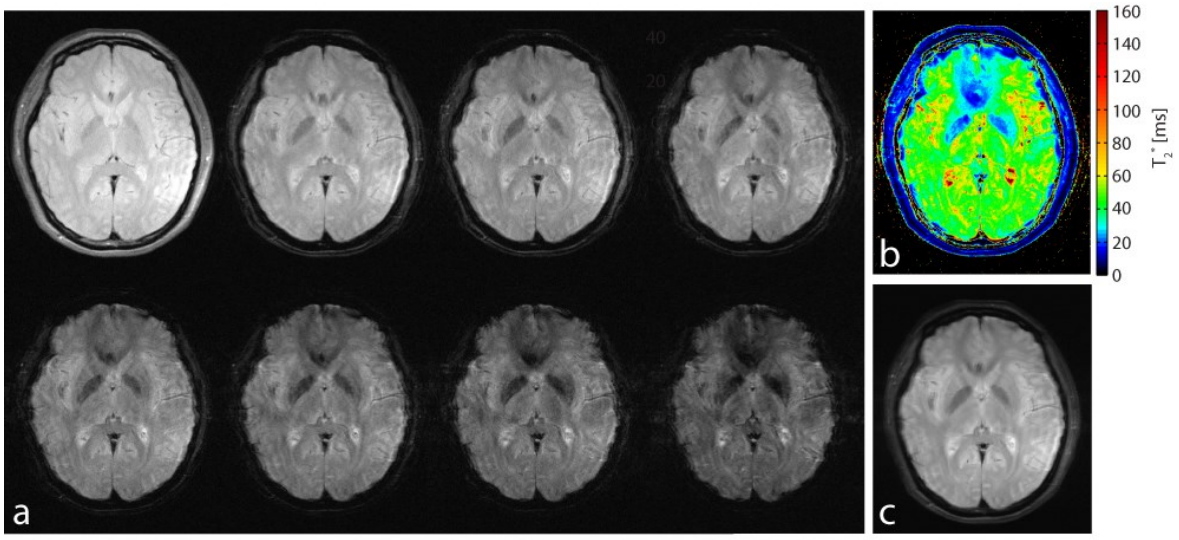

Figure 34: ***In-vivo*** **T_2^* mapping using 2in1-RARE**
(**a**) Images reconstructed for one out of eight slices from the SE magnetization applying evolution times τ = 0-30 ms using an equidistant increment of τ = 5 ms plus τ = 40 ms are shown. (**b**) A T_2^* map calculated from the series of 13 datasets with evolution times τ ranging from 0 ms to 40 ms is depicted. (**c**) Simultaneously to the T_2^*-weighted images, the pulse sequence provides PD-weighted data. PD-weighted images resulting from the 13 acquisitions are averaged to generate an anatomical image which exhibits a spatial resolution of (0.5 x 0.5 x 5.0) mm^3 [FUCHS2014b].

3.3.3 Application in patients with multiple sclerosis

The imaging protocol used in healthy subjects was transferred to a proof-of-principle patient study involving a male MS patient as a precursor to a broader clinical study in collaboration with Jens Würfel (NeuroCure, Charité, Berlin; Neuroradiology, Goettingen). 3D T_1-weighted GRE (MPRAGE) imaging was performed for anatomical reference. Figure 35 surveys the results and demonstrates the capability of 2in1-RARE to depict small MS lesions in the PD-weighted STE image as well as in the T_2^*-weighted SE image. The lesions show hypointense signal versus white matter in the anatomical reference images with a lesion/white matter contrast of 0.7. In the PD-weighted as well as in the T_2^*-weighted images the lesions appear hyperintense with a lesion/white matter contrast of 1.2 for the PD-weighted data and 1.4 for the T_2^*-weighted images. The trend of superior lesion/white matter contrast in the T_2^*-weighted images (10% higher compared to the

contrast obtained in the T_1-weighted reference data) compares well to previous studies in which T_2^*-weighted imaging has been applied to characterize MS lesions and to differentiate them from lesions linked to other pathologies [SINNECKER2012, WUERFEL2012, SINNECKER2013].

It is anticipated to include further patients with various pathologies (e.g. stroke) to widen the range of possible application scenarios of 2in1-RARE.

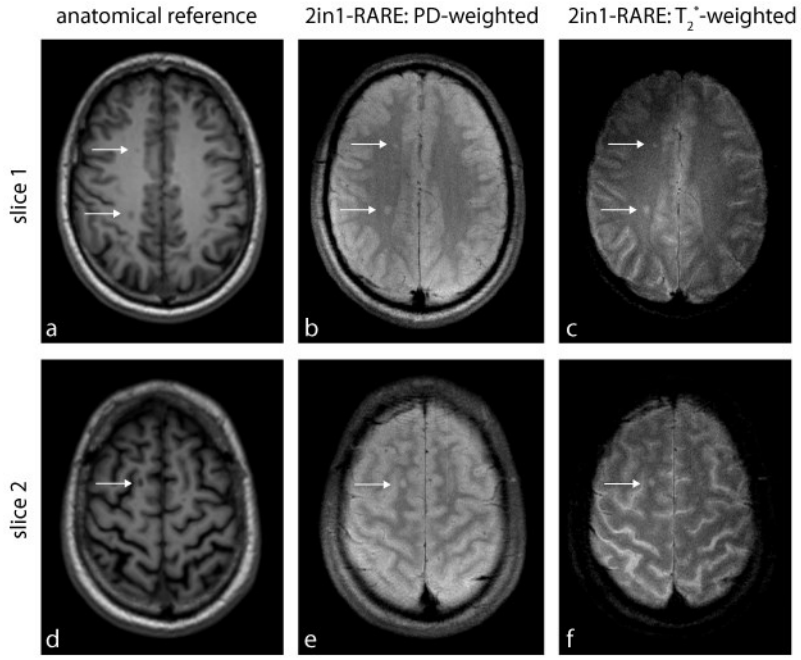

Figure 35: **2in1-RARE MS patient data**
In-vivo brain images of a multiple sclerosis patient acquired at 3.0 T comparing 2in1-RARE images with anatomical T_1-weighted GRE (MPRAGE) imaging. One slice showing lesions of different sizes (diameter between 2 mm and 5 mm) (**a**-**c**), and a second slice comprising one lesion with a diameter of approximately 5 mm (**d**-**f**) are depicted. The left column contains anatomical reference images reconstructed from the 3D T_1-weighted GRE dataset. PD-weighted images derived from 2in1-RARE are shown in the center column and T_2^*-weighted images obtained by 2in1-RARE are depicted in the right column [FUCHS2014b].

3.4 Summary and Discussion

The feasibility of the proposed 2in1-RARE sequence that facilitates simultaneous recording of two differently weighted RARE images (PD and T_2^*) within one acquisition has been demonstrated. The complete separation of spin echoes and stimulated echoes within the preparation experiment 90°-α_1-α_2 by displacing secondary stimulated echoes allows independent contrast manipulation for each echo group. The current implementation induces T_2^* weighting on the spin echo magnetization by means of the insertion of an evolution time τ during the first ESP which is the time period during which the stimulated echo magnetization is stored along the longitudinal axis. Consequently, the stimulated echo remains PD-weighted or T_2-weighted depending on the

effective TE. Hence, the proposed method combines anatomical information (PD/T_2 weighting) and functional aspects (T_2^* weighting) within one acquisition. 2in1-RARE offers a speed gain of factor two over conventional RARE approaches and thus presents a valuable alternative to sequential PD/T_2 and T_2^*-weighted RARE acquisitions. This advantage can be used for simultaneous T_2/T_2^* mapping. 2in1-RARE holds the promise to eliminate slice-misregistration artifacts frequently encountered in sequential T_2/T_2^*-weighted acquisitions due to bulk or physiological motion.

It is a recognized limitation that 2in1-RARE comes with a SNR penalty versus conventional RARE. This caveat can be relaxed by using many element RF coil arrays [ZHU2004b, SODICKSON2005, WIGGINS2006, WIGGINS2009]. Also, the proof-of-principle implementation of 2in1-RARE used here bears potential for echo spacing reduction by using shorter RF pulses which would help to preserve SNR.

A broadening in the PSF of 15% was observed for 2in1-RARE versus the split-echo RARE approach. This increase in the FWHM of the PSF is attributed to the faster signal decay within the echo train compared with split-echo RARE due to omission of secondary stimulated echoes. SNR analysis showed that 2in1-RARE performs proportionate with the split-echo RARE technique in terms of signal intensity and noise level. A key feature for meeting image quality requirements in 2in1-RARE is the RF pulse angle scheme. The first two refocusing RF pulses α_1 and α_2 ensure a balanced split of the initial transverse magnetization into two parts. Only a small amount of secondary stimulated echoes is generated in case of near 180° RF pulses from α_3 on, resulting in moderate signal decay over the echo train.

One shortcoming of the current implementation is the moderate T_2 weighting of STE magnetization resulting in rather PD than T_2-weighted images. This can be attributed to the fast decaying signal within the echo train because secondary stimulated echoes are not included. Consequently, a longer TE commonly used for T_2 weighting might result in image quality degradation. Indeed, there are various applications putting PD-weighted images to clinical use including the assessment of lesion load in multiple sclerosis patients [ROCCA2013]. It would be favorable if 2in1-RARE would offer the flexibility to also generate images with strong T_2 contrast. At lower magnetic field strengths, where 180° RF pulses are close to their nominal value, the signal decay within the echo train would be slower, and hence T_2 weighting could be achieved by changing the order of the applied center-out phase encoding scheme. Adiabatic RF pulses are less sensitive to non-uniformities in the excitation field and would help to facilitate 180° refocusing RF pulses to maintain the transversal magnetization even at higher magnetic field strengths

[NORRIS1989, DE GRAAF2003, BALCHANDANI2012, VAN KALLEVEEN2012]. The incorporation of separate readout gradients for the two single echoes presents the possibility to vary the ordering scheme in k-space independently for the SE and the STE. Thus, the T_2 weighting of the STE can be increased without inducing extra weighting to the T_2^*-weighted SE image. A further option to enhance T_2 weighting is the use of an additional T_2 preparation module [BRITTAIN1995] before the 2in1-RARE imaging module which implicates the need for a T_2 correction of the T_2^*-weighted image.

The strict separation of SE and STE magnetization within the RARE echo train offers further possibilities for contrast manipulation. While the STE magnetization is stored along the longitudinal axis, the SE part could be sensitized to diffusion. Simultaneous measurement of T_2 and ADC has been presented previously [FRANCONI1994, SONG2004, ONG2005]. These approaches do not combine the separation of SE and STE with a RARE readout but rather use three RF pulses to generate both echo groups. 2in1-RARE is capable of generating two different T_2^* contrasts for the SE and STE images. Furthermore, flow sensitive bipolar gradients can be applied while the STE magnetization is stored along the longitudinal axis to encode for velocity of the SE part.

Obviously, the proposed 90°-α_1-(τ)-α_2 preparation module can be combined with other rapid imaging modules such as EPI, GRASE and FLASH. The proposed preparation is compatible with non-Cartesian phase encoding. Moreover, the initial excitation RF pulse can be substituted by any spin preparation that provides transverse magnetization. The proposed 2in1-RARE approach is not limited to brain images but also holds the promise to meet the needs of applications such as cardiac imaging as well as abdominal and liver imaging.

In summary, a modified RARE variant designated 2in1-RARE was developed within the scope of this thesis. 2in1-RARE strictly separates magnetization of primary spin echoes and stimulated echoes within a RARE echo train. This enables the simultaneous generation of independent images with two different contrasts. The performed experiments presented in this chapter demonstrated that PD and T_2^*-weighted phantom and brain images simultaneously acquired with the 2in1-RARE sequence provide image quality comparable to conventional but sequential PD and T_2^*-weighted RARE approaches.

4. Development of diffusion-sensitized Rapid Acquisition with Relaxation Enhancement Imaging

In today's clinical practice, single-shot echo planar imaging (ss-EPI) is most widely used for neurovascular DWI. Because of its speed advantage, ss-EPI offers excellent temporal resolution and insensitivity to bulk motion and, nevertheless, reasonable spatial resolution. Notwithstanding these capabilities, EPI is prone to magnetic susceptibility artifacts that present themselves as signal loss and image distortion. These detrimental effects are more severe at high magnetic field strengths and particularly pronounced in regions with poor main magnetic field homogeneity. Thus, DWI of cranial regions adjacent to cavities, sinuses, or near skin/muscle/bone/brain boundaries is particularly challenging and prone to geometric distortions.

This constraint constitutes a severe challenge for diffusion-sensitized EPI of the eye and orbit as revealed by a recent study comparing different magnetic field strengths; nondiagnostic image quality due to geometric distortion was observed in 40% (2 out of 5) of the study population investigated at 3.0 T [ERB-EIGNER2013]. These pioneering insights suggest a clinical preference for ophthalmic DWI at 1.5 T. Nonetheless, distorted DWI-EPI images are still prevalent at 1.5 T [ERB-EIGNER2013]. The propensity of EPI to geometric distortion at 3.0 T might be elusive if not prohibitive for diffusion-sensitized ophthalmic MRI at 7.0 T. A possible way to reduce distortion in EPI is the application of segmented k-space data collection schemes [KIM1996, JEZZARD2012]. Readout-segmented EPI (rs-EPI) was shown to afford DWI of the brain at 3.0 T and at 7.0 T with largely reduced susceptibility artifacts [PORTER2009, HEIDEMANN2010]. Arguably, the applicability and efficacy of rs-EPI for ophthalmic imaging is yet untapped and requires careful assessment in healthy subjects and patients.

An imaging strategy that presents with an immunity to image distortions is conceptually appealing for the pursuit of anatomically accurate DWI of the eye and orbit, especially at higher B_0. RARE, being largely insensitive to B_0 inhomogeneity related image distortions, presents a valuable alternative to EPI particularly at (ultra)high magnetic field strengths. This makes it attractive to use diffusion-sensitized RARE techniques for MRI of the eye and orbit. Recently, single-shot RARE (ss-RARE) was shown to be suitable for ophthalmic imaging [DE GRAAF2012b]. Notwithstanding this

success, ss-RARE runs the caveat of being prone to blurring artifacts induced by point spread function broadening and, hence, is limited in spatial resolution.

Recognizing the clinical opportunities of ocular MRI along with the sensitivity gain [RICHDALE2009, LANGNER2011, BEENAKKER2013, GRAESSL2014a, LINDNER2014, WALTER2014] and the recent clinical advances of high spatial resolution MRI at (ultra)high magnetic fields [NIENDORF2013, SINNECKER2013, BIZINO2014, BOUVY2014, FISCHER2014, HAN2014, MÜLLER2014, ZEINEH2014, KRAFF2015, NIENDORF2015], this chapter examines the applicability of diffusion-sensitized multi-shot RARE (ms-RARE) for the pursuit of anatomically accurate DWI of the eye and orbit at 3.0 T and 7.0 T. To meet this goal a diffusion-sensitized split-echo ms-RARE variant was adapted upon and implemented. The suitability of ms-RARE for distortion-free DWI was carefully demonstrated in phantom experiments and benchmarked against ss-RARE, ss-EPI and rs-EPI at 3.0 T and at 7.0 T. The clinical applicability of ms-RARE for DWI of the human eye, optical nerve, ocular muscles and orbit was examined in an initial feasibility study including ten healthy adult subjects and patients with intraocular masses (uveal melanoma). The merits and limitations of diffusion-sensitized ms-RARE are discussed and implications for clinical ophthalmic MRI at 3.0 T and 7.0 T are considered.

Portions of this chapter have been published in [FUCHS2014d] and were submitted to Investigative Radiology as a full paper which was accepted for publication in November 2014. Driven by the motivation to enhance image quality of ophthalmic DWI, a RARE based imaging approach was adapted [WILLIAMS1999] and was completely independently implemented. All of the work and experiments necessary to demonstrate the feasibility of ms-RARE were performed independently. This included pulse sequence implementation including the phase correction algorithm on a clinical scanner, development and validation of the reconstruction software, collection of experimental data in phantoms and benchmarking of ms-RARE versus ss-RARE, ss-EPI and rs-EPI. As part of the project, the applicability of ms-RARE for ophthalmic imaging was examined in an *in-vivo* feasibility study in healthy volunteers and patients with intraocular masses.

4.1 Implementation of diffusion-sensitized multi-shot split echo RARE

The diffusion-sensitized multi-shot split-echo RARE (ms-RARE) variant is shown schematically in Figure 36a including diffusion sensitization, phase correction for motion compensation and the imaging module [WILLIAMS1999]. The dephasing gradient along the frequency encoding direction was modified from the original RARE, being now unbalanced to separate the echo into two groups for ESP. This approach eliminates interferences between odd and even echoes (E1 and E2) [SCHICK1997]. Unipolar diffusion sensitizing gradients were placed around the first refocusing RF pulse. The first two echoes were acquired without phase encoding to support 1D navigator phase

correction for eye motion compensation [ANDERSON1994, ORDIDGE1994, MORI1998, WILLIAMS1999]. The phase graph in Figure 36b depicts the magnetization evolution for the odd (E1) and the even (E2) echo group. E1 and E2 were reconstructed separately and the resulting images added afterwards to provide the final image.

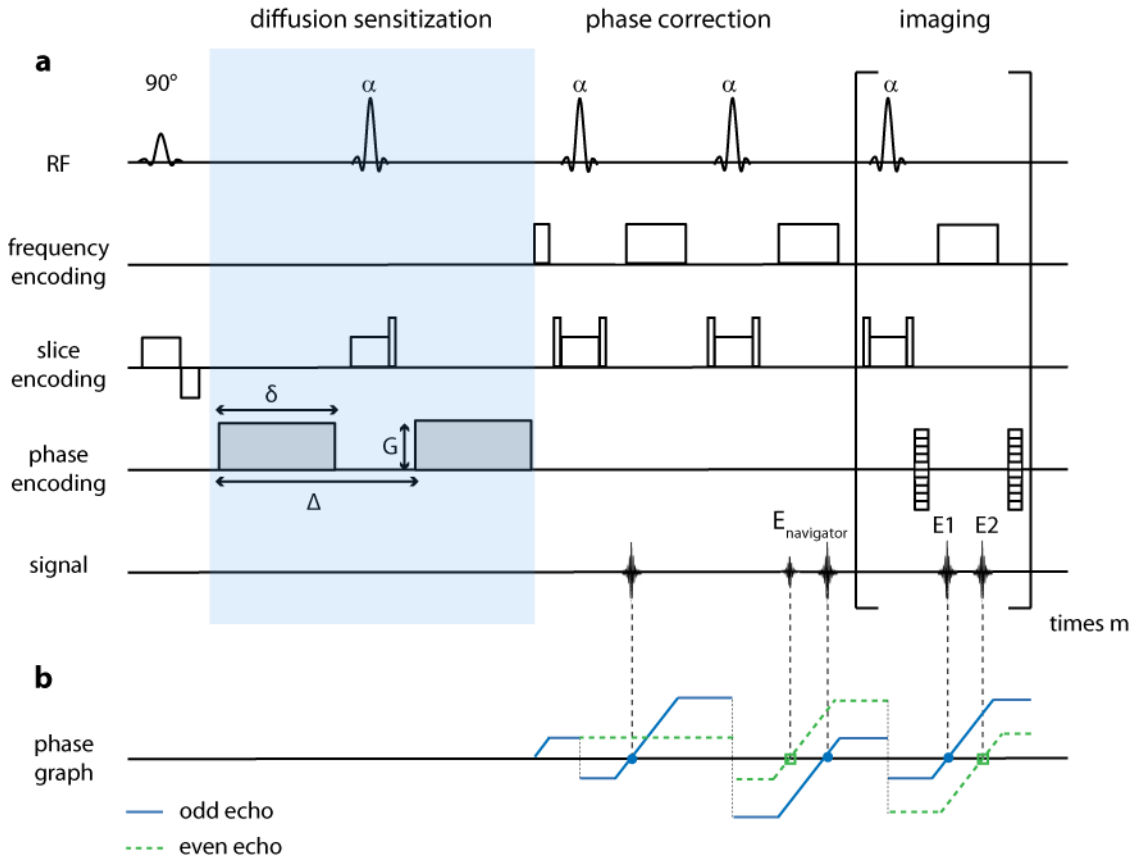

Figure 36: **Diffusion-sensitized multi-shot split echo RARE sequence diagram**
(a): Basic scheme of the diffusion-sensitized multi-shot split-echo RARE (ms-RARE) sequence [WILLIAMS1999] showing the RF pulse train, the frequency encoding, phase encoding and the slice selection gradients. The dephasing frequency encoding gradient prior to the second refocusing RF pulse α is unbalanced, i.e. the 0^{th} moment of this gradient does not equal half the 0^{th} moment of the readout gradient [SCHICK1997]. Unipolar diffusion sensitization gradients of amplitude G and duration δ, separated by the delay between the onset of the gradient pulses (Δ), surround the first refocusing pulse in phase encoding direction. After the third refocusing pulse, the odd (E1) and the even (E2) echo are generated for the first time. These data are acquired without phase encoding and serve as 1D navigator signal ($E_{navigator}$) to correct for motion artifacts caused by changing unknown phase shifts due to the diffusion sensitization from shot to shot. The odd (E1) and the even (E2) echoes are acquired within each echo spacing, reconstructed separately, with the resulting images being added afterwards. **(b)**: The evolution of the magnetization is illustrated in the extended phase graph. Only the two pathways contributing to the signal are shown: the odd echo (blue solid line) and the even echo (green dashed line).

Ghosting artifacts in diffusion-weighted images arise from phase errors corrupting the raw data and being translated into the processed image via FT. Rigid body motion, also called bulk motion, is the primary source of these phase errors and can be categorized into two types of motion:

translation and rotation. It has been shown that translational motion causes zero-order (i.e. constant) phase errors whereas rotation results in first-order (i.e. linear) phase errors [ANDERSON1994]. Correcting translational motion using a non-phase encoded additional echo, called 1D navigator echo, in a Stejskal-Tanner preparation experiment has been introduced long ago [ORDIDGE1994]. Subsequently, the concept has been extended to correct for rotations [ANDERSON1994, DE CRESPIGNY1995]. Thorough considerations on signal evolution and the effect of phase errors revealed that translational and rotational motion can only be corrected satisfyingly with 1D navigators if the diffusion sensitization gradients are applied along the phase encoding direction [ANDERSON1994]. In the case of diffusion sensitization gradients being applied along the slice selection or frequency encoding axis, the use of 2D navigator echoes is favorable [BUTTS1996].

The 1D phase correction scheme applied for ms-RARE has been described previously [MORI1998, WILLIAMS1999]. A schematic illustration is displayed in Figure 37. Navigator echoes $E_{nav,j}$ are acquired without phase encoding before the actual data acquisition once the even and odd echo groups have built up. Thus, navigator information is available for even and odd signal parts for each excitation cycle j with $j = 1…j_{max}$, where j_{max} is the total number of excitations. Splitting the k-space at the center frequency creates two sub-k-spaces; k-$space_{even}$ and k-$space_{odd}$ which are considered and reconstructed separately using the same algorithm. k-space splitting is conducted for the navigator data as well as for the image data. Next, all navigator echoes $E_{nav,j}$ are masked so that only segments with explicit non-zero signal are considered. Navigator and image projections along the frequency encoding direction are generated via 1D FFT. Subsequently, the navigator echo with the highest signal amplitude is determined as the reference navigator $E_{nav,ref}$. The difference $\Delta\Phi_j$ between the phase of the reference navigator Φ_{ref} and the phase of all navigator echoes Φ_j is calculated. The excitation number j is determined for each image projection and the corresponding $\Delta\Phi_j$ is added. Thus, phase variations among different excitations are eliminated. In the next step, 1D FFT along phase encoding direction is performed for the corrected image data. Finally, combining the single RF coil images using the sum-of-square routine and adding the even and the odd image generates the final result.

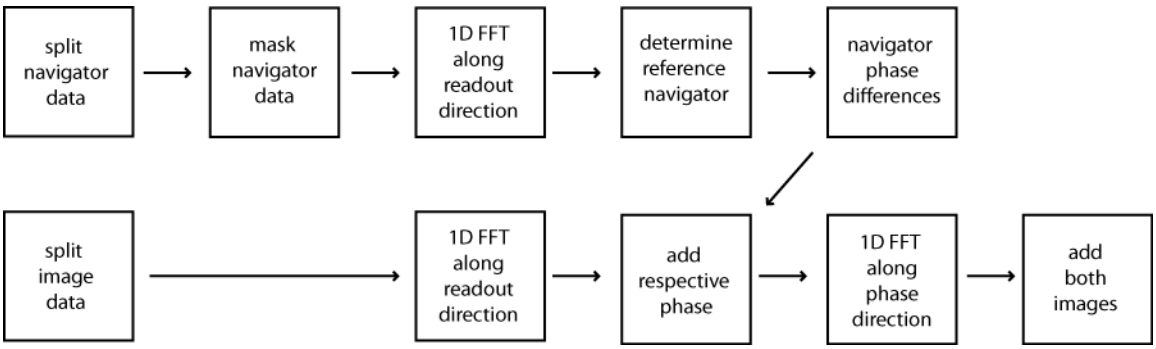

Figure 37: **Process chart of the split-echo RARE 1D navigator phase correction**
Single steps of the phase correction are illustrated schematically for the navigator data as well as the image data.

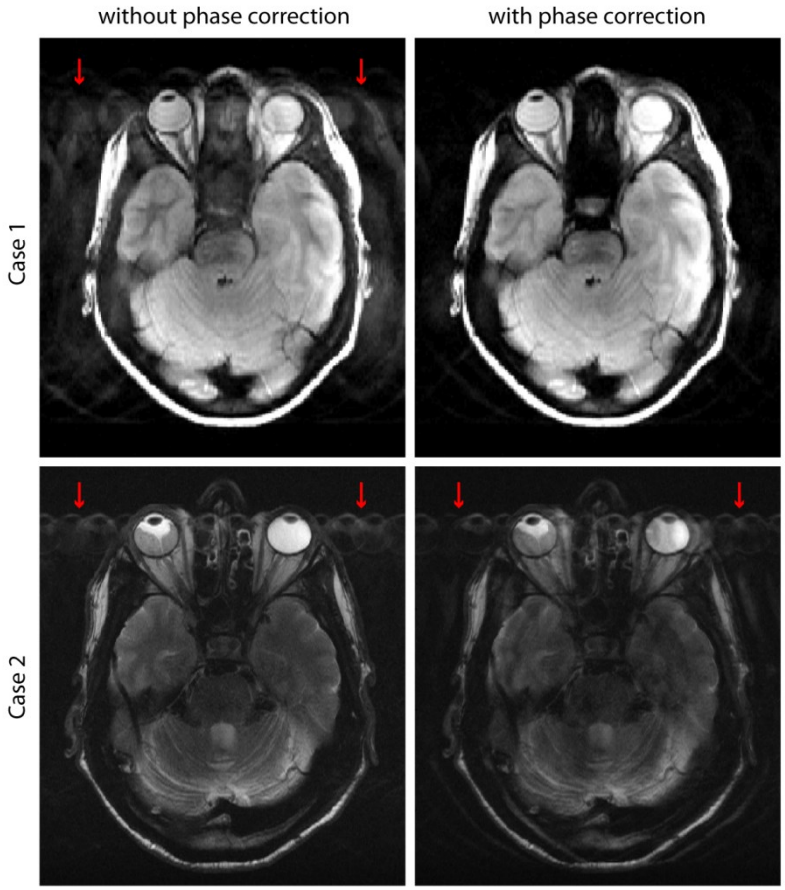

Figure 38: **Performance of 1D navigator phase correction**
Example 1 exhibits low-intensity ghosting artifacts that are well compensated with the 1D navigator phase correction. In comparison, example 2 shows high-intensity ghosting artifacts that cannot be corrected using the described formalism. The images without and with phase correction exhibit the same window settings. Artifacts are marked with red arrows.

The performance and quality of the phase correction varies with the integrity of the input data. Since only 1D correction was implemented into the pulse sequence, diffusion sensitization gradients were always applied along the phase encoding direction to avoid uncorrectable phase

errors. Case 1 in Figure 38 exemplifies a dataset with ghosting artifacts due to eye movements during data acquisition that are well compensated by the 1D phase correction. The images without and with phase correction exhibit the same window settings and it becomes obvious that no ghost images of the eyes are present after the phase correction. In comparison, case 2 shows an example for which the phase correction failed. The intensity of the ghosting artifacts is much more pronounced. This suggests that the degree of motion during the acquisition was considerably higher and more complex, i.e. taking place in various directions which might be an explanation for the failure of phase correction in that particular case.

4.2 Validation in phantom experiments

The applicability of ms-RARE for the purpose of diffusion-weighted imaging was examined in phantom experiments before moving to *in-vivo* examinations. Static phantoms were employed (i) to evaluate SNR performance, (ii) to analyze PSF characteristics and (iii) to review the strength of diffusion weighting. In each of these three sets of experiments ms-RARE was benchmarked versus ss-EPI and ss-RARE. ss-EPI is considered as the gold standard for DWI and ss-RARE is useful to offset EPIs distortion constraints. Both techniques were provided by the MR manufacturer and were applied without further modifications.

Thanks to a collaboration with Siemens Healthcare (Erlangen, Germany), the readout segmented EPI (rs-EPI) pulse sequence was made available for our study. To assess and quantify the extent of geometric distortions, a comparison of ms-RARE, ss-EPI and rs-EPI was performed in a structure phantom.

4.2.1 Signal-to-noise ratio assessment

SNR was evaluated for ss-EPI, ss-RARE and ms-RARE for b-values ranging from 0 s/mm^2 to 1000 s/mm^2 at 3.0 T. For this purpose, a basic cylindrical phantom containing distilled water mingled with manganese chloride was used (T_1 = (1024 $\pm$ 3) ms, T_2 = (93 $\pm$ 1) ms). Sequence parameters are summarized in Table 6. Identical spatial resolution and comparable receiver bandwidth were chosen to enable a reasonable comparison. For each approach TE was set to minimum to preserve SNR.

Table 6: **Sequence parameters for the SNR comparison**
Common sequence parameters used for the SNR comparison of ss-EPI, ss-RARE and ms-RARE are noted.

	ss-EPI	ss-RARE	ms-RARE
spatial resolution [mm^3]	1.0 x 1.0 x 5.0	1.0 x 1.0 x 5.0	1.0 x 1.0 x 5.0
TR [ms]	3000	2290	500
TE [ms]	171	113	21
receiver bandwidth [kHz]	483	303	333

Table 7 summarizes SNR obtained for different b-values using ss-EPI, ss-RARE as well as ms-RARE imaging. This survey demonstrates that the proposed ms-RARE implementation provides SNR which is competitive with the clinically established methods ss-EPI and ss-RARE techniques.

Table 7: Comparison of SNR
Mean SNR ($\pm$ standard deviation) are given for each pulse sequence type and b-value ranging from 0 s/mm^2 to 1000 s/mm^2.

b-value [s/mm^2]	ss-EPI	ss-RARE	ms-RARE
0	32.0 ± 2.6	61.2 ± 5.4	29.0 ± 2.4
250	19.2 ± 1.6	32.3 ± 2.7	16.6 ± 1.3
500	11.0 ± 1.0	16.6 ± 1.5	9.7 ± 0.9
750	6.73 ± 0.9	11.0 ± 1.3	6.1 ± 0.7
1000	4.0 ± 0.8	5.1 ± 0.9	4.5 ± 0.7

4.2.2 Point spread function assessment

The objective for the PSF comparison of ss-EPI, ss-RARE and ms-RARE is to quantify image quality with respect to effective spatial resolution and image sharpness. For this purpose, the cylindrical phantom used for the SNR assessment in the previous section was employed and the pulse sequence parameters (Table 6 in the previous section) were kept the same. To study the effect of diffusion sensitization b-values of 0 s/mm^2 and 1000 s/mm^2 were employed. Phase encoding gradients were turned off. The FWHM of the PSF was determined as a quantitative measure.

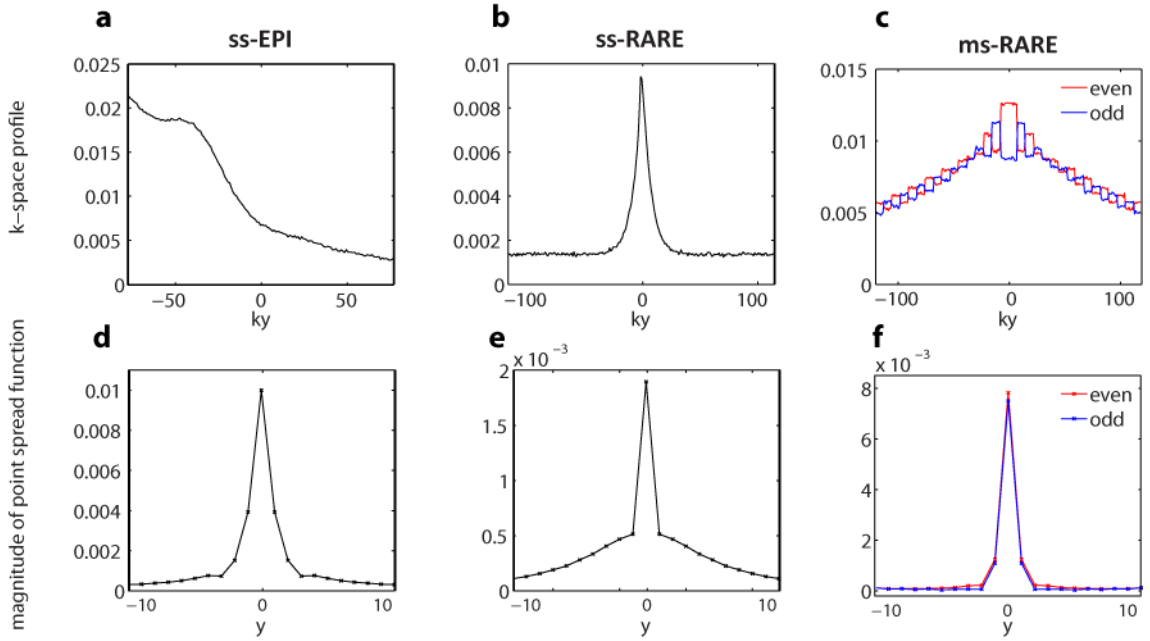

Figure 39: **PSF comparison for b = 0 s/mm²**

k-space profiles are depicted for ss-EPI (**a**), ss-RARE (**b**) and ms-RARE (**c**) for acquisitions exhibiting b = 0 s/mm². **d-f**: The corresponding PSF for each pulse sequence is shown. For the split-echo RARE approach, the profiles and PSFs are shown for the even (red) and the odd (blue) echo groups.

Figure 39 depicts the k-space profiles and central extracts of the PSFs obtained for b = 0 s/mm². The width of the main peak is in the same range for all three approaches, which is quantified by the FWHMs given in Table 8. The FWHM for ms-RARE is 20% lower compared to the ss-EPI approach and 10% lower versus the ss-RARE variant for b = 0s/mm². The broad shoulder in the PSF obtained for ss-RARE might explain image blurring which mainly occurs for low b-values. For b = 1000 s/mm² (Figure 40) an overall reduction in signal intensity due to the strong diffusion weighting was observed but the FWHM of the PSF was found to be reduced by 20% for ss-EPI and ss-RARE while the reduction was only 7% for ms-RARE.

Table 8: Comparison of PSF FWHM

FWHM in pixel is given for ms-RARE, ss-RARE and ss-EPI for b = 0 s/mm² and b = 1000 s/mm². In the case of split-echo RARE, the FWHM is stated for both echo groups.

Method	FWHM for b = 0 s/mm²	FWHM for b = 1000 s/mm²
ss-EPI	1.7	1.3
ss-RARE	1.5	1.2
ms-RARE	1.4/1.3	1.3/1.2

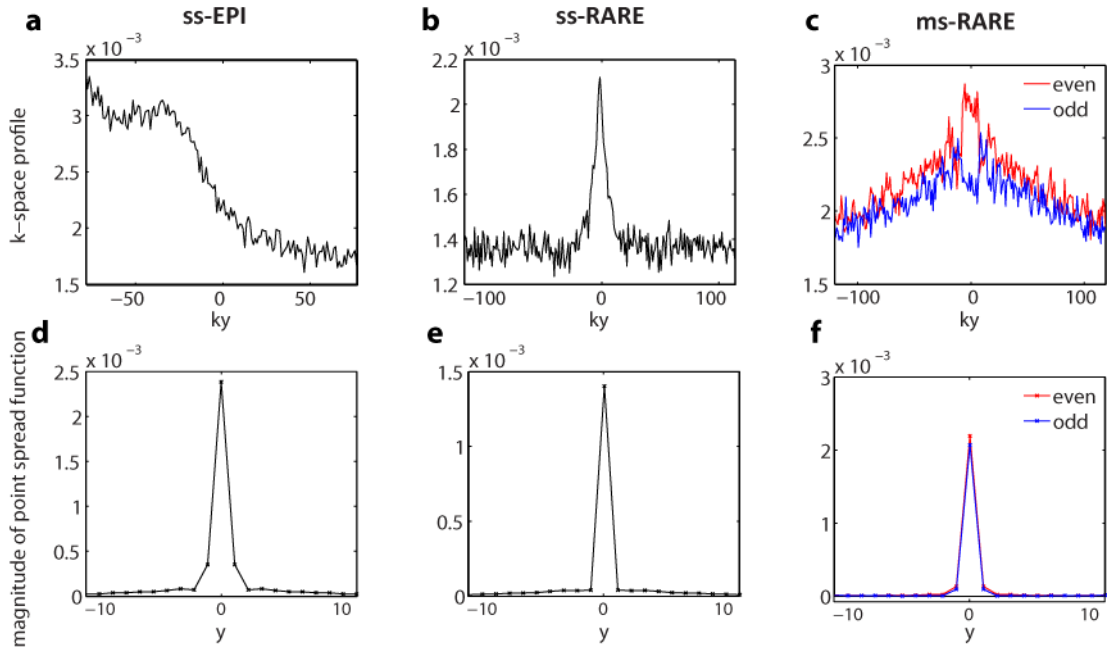

Figure 40: **PSF comparison for b = 1000 s/mm²**
k-space profiles are depicted for ss-EPI (**a**), ss-RARE (**b**) and ms-RARE (**c**) for acquisitions exhibiting b = 1000 s/mm². **d-f**: The corresponding PSF for each pulse sequence is shown. For the split-echo RARE approach, the profiles and PSFs are shown for the even (red) and the odd (blue) echo groups.

These data demonstrate that the effective spatial resolution which was quantified by the FWHM of the PSF afforded by ms-RARE is as good as the effective spatial resolution of ss-EPI and ss-RARE and is even superior if no diffusion weighting is applied.

4.2.3 Validation of the diffusion weighting

The goal of this set of experiments was to validate the diffusion weighting within ms-RARE. Artifact levels were benchmarked against ss-EPI and ss-RARE. For this purpose a static cylindrical phantom (diameter d = 14 cm) containing four tubes filled with liquids with known ADCs fixed in agarose was employed. Tap water (50 ml, d = 30 mm), acetone (assay ≥ 99.5%, 50 ml, d = 30 mm), dimethyl sulfoxide (DMSO, 15 ml, d = 17 mm) and sunflower oil (50 ml, d = 30 mm) were selected as references. T_2 relaxation times at 3.0 T are 2-3 s for tap water, acetone and DMSO and approximately 100 ms for sunflower oil [BERNSTEIN2004]. Sequence parameters (Table 9) were adjusted to achieve the best possible image quality for each DWI approach. Volume selective B_0 shimming was applied for all three approaches which is primarily beneficial for ss-EPI due to its propensity to B_0 inhomogeneity related artifacts. Diffusion encoding was performed along the phase encoding direction using five b-values ranging from 0 s/mm² to 1000 s/mm² with a constant increment 250 s/mm². The experiments were performed at room temperature (T = 23°C). ADC maps were generated by applying a linear fit to the logarithmized data consisting of the five

acquisitions with increasing b-value. A ROI was placed in the area of each reference liquid to calculate mean value and standard deviation of ADC.

Table 9: Sequence parameters for the ADC survey

Imaging parameters used for the validation of diffusion weighting in ms-RARE. For comparison ss-EPI and ss-RARE were applied.

	ss-EPI	ss-RARE	ms-RARE
spatial resolution [mm^3]	1.8 x 1.8 x 5	1.3 x 1.3 x 5	1.0 x 1.0 x 5
matrix	136 x 136	192 x 192	256 x 256
TR [ms]	5000	2940	2000
TE [ms]	119	115	98
receiver bandwidth [kHz]	454	232	250
nominal flip angle (refocusing)	90°	120°	180°
b-values [s/mm^2]	0, 250, 500, 750, 1000		

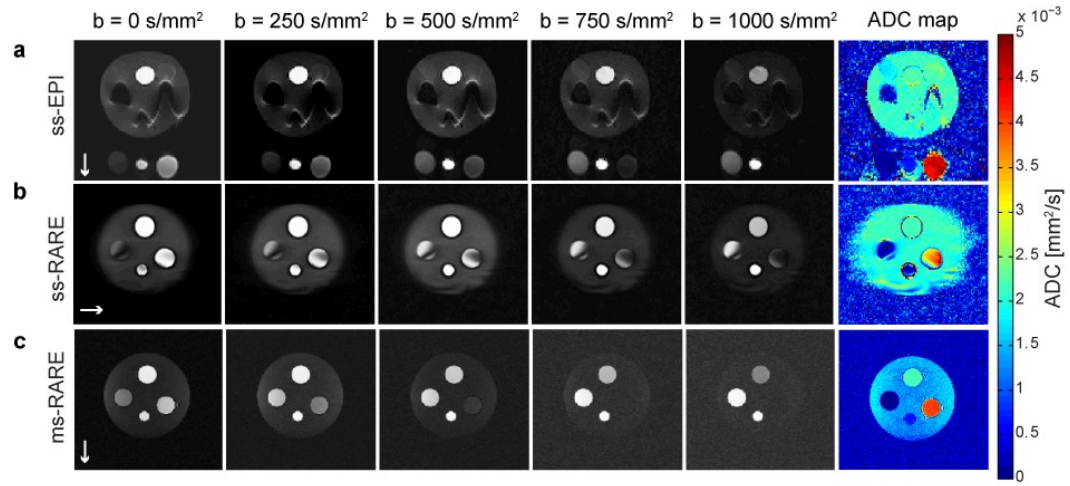

Figure 41: **Survey of DWI images and ADC maps**

ss-EPI **(a)**, ss-RARE **(b)** and ms-RARE **(c)** images exhibiting different b-values are depicted. For better illustration, the images do not exhibit identical window settings. Phase encoding direction is denoted by white arrows in the b = 0s/mm^2 images. The last column shows ADC maps calculated from the differently weighted images for each of the three approaches. The cylindrical phantom (d = 15 cm) contains water (top), acetone (right), DMSO (bottom) and sunflower oil (left) fixed in agarose. Due to severe geometric distortions in the ss-EPI images (a), oil, DMSO and acetone are displayed from left to right on the very bottom of the images.

Figure 41 depicts the acquired images using five different b-values and the three pulse sequence types together with the resulting ADC maps. Single-shot EPI images yielded severe geometric distortions and ghosting artifacts. Three of the four tubes were severely mis-registered due to

chemical shift artifacts along the phase encoding direction and were superimposed by severe ghosts due to off resonance effects. These artifacts arise from the low bandwidth in phase encoding direction of 1300 Hz/pixel (ESP = 0.77 ms) of the applied ss-EPI protocol. Given this value, even small frequency offsets due to the chemical shift between various materials result in the pronounced pixel displacements that were observed in this experiment. The tubes with sunflower oil, acetone and DMSO are displaced while the water tube does not present any artifact. This can be explained by the chemical shift between the agarose part of the phantom – which mainly consists of water – and sunflower oil (≈ 3.5 ppm), acetone (≈ 2.8 ppm), DMSO (≈3.4 ppm) [HOFFMAN2006]. Due to the similar chemical shift between water and the agarose filling, the water tube is not displaced. Signal voids and image blurring due to the long train of high flip angle refocusing RF pulses are observed for the ss-RARE images. No image artifacts are visible for ms-RARE which shows a decreased SNR due to the enhanced spatial resolution. Transferring the larger matrix size to ss-EPI and ss-RARE amplified the artifact level due to the increase in echo train length and resulted in data which could not be evaluated. On the other hand, decreasing the read-out size for ms-RARE lead to an imperfect separation of both echo groups which caused ring-like image artifacts.

Table 10 surveys the ADCs derived from the proposed ms-RARE approach and the reference techniques ss-EPI and ss-RARE. Despite of the artefacts obtained for ss-EPI and ss-RARE a good agreement was found for ADC_{water} for the three approaches. The ADCs derived from the proposed diffusion-weighted ms-RARE approach accord very well with the literature. This result confirms the correct diffusion weighting within ms-RARE. It also highlights the capabilities of ms-RARE to support ADC mapping for compounds resembling diffusion rates of healthy and pathologic tissue. The ss-RARE images show image artifacts within the oil, acetone and DMSO tubes resulting in deviating ADC mean values and increased standard deviations versus ss-EPI and ms-RARE.

Table 10: Synopsis of the diffusion weighting validation
Mean ADC (± standard deviation) is given in units of 10^{-3} mm^2/s and were calculated from ROIs placed in the respective material. The last row gives literature values for each of the four materials.

	Water	Oil	Acetone	DMSO
ss-EPI	2.220 ± 0.067	0.087± 0.030	4.552 ± 0.227	0.692 ± 0.011
ss-RARE	2.167 ± 0.028	0.153 ± 0.121	3.980 ± 0.445	0.366 ± 0.285
ms-RARE	2.104 ± 0.038	0.030 ± 0.018	4.026 ± 0.119	0.675 ± 0.020
Literature values	2.13 (25°C) [LANDOLT1969]	0.01 [DEONI2004]	4.77 (25°C) [LANDOLT1969]	0.73 (25°C) [HOLZ2000]

This experiment confirms the precise diffusion weighting within ms-RARE and demonstrates the capability of ms-RARE to provide artifact free images with high spatial resolution in contrast to ss-EPI and ss-RARE.

4.2.4 Quantification of geometric distortions

This section focuses on the assessment of geometric distortions in ms-RARE, ss-EPI and rs-EPI at 3.0 T and at 7.0 T. For this purpose, a cylindrical structure phantom (diameter d = 18 cm, height h = 14 cm) was used. A transaxial slice covering five cylinders (d = 3.5 cm) containing different concentrations of $MnCl_2$ in distilled water was used for imaging. For all three imaging approaches data exhibiting a spatial resolution of (0.9 x 0.9 x 5.0) mm^3 were acquired for b = 0 s/mm^2 and b = 500 s/mm^2 at 3.0 T and at 7.0 T. A localizer spoiled gradient echo (FLASH) acquisition exhibiting the same spatial resolution and matrix size was used as a reference to define image geometry. To visualize the extent of geometric distortions, contours around the cylindrical structures in the phantom were defined in the FLASH reference image and transferred to the data obtained with ms-RARE, ss-EPI and rs-EPI. Quantification of geometric distortions was performed using center of gravity analysis. For this purpose, the areas within the contours were determined using an edge detection algorithm based on intensity differences and the center of gravity was calculated for each structure. The displacement of the center of gravity (in pixels) was calculated with respect to the FLASH reference image. All displacements obtained were averaged over all structures and the two b-values for each imaging approach.

The ms-RARE variant produced distortion-free images at 3.0 T and at 7.0 T as demonstrated by the difference maps in Figure 42. Unlike ms-RARE, modest displacements between the contour lines and the image of the phantom were observed for rs-EPI. The distortions were most pronounced for ss-EPI which showed displacements of up to 2.4 mm at 3.0 T and 7.4 mm at 7.0 T along the phase encoding direction. The quantitative assessment of the geometric integrity using the center of gravity approach revealed that images obtained with ms-RARE accord very well with the reference derived from FLASH imaging. It should be noted that the geometric integrity of the ms-RARE images was maintained over the range of diffusion sensitizations used. No significant differences were observed for acquisitions with b = 0s/mm^2 and b = 500 s/mm^2. In rs-EPI the center of gravity was displaced by $(1.8 \pm 0.5)/(2.3 \pm 1.4)$ pixels from the reference at 3.0 T/7.0 T. Even more prominent displacements were observed for ss-EPI, in which a displacement of center of gravity by $(2.7 \pm 1.0)/(8.3 \pm 5.7)$ pixels from the FLASH reference was observed at 3.0 T/7.0 T.

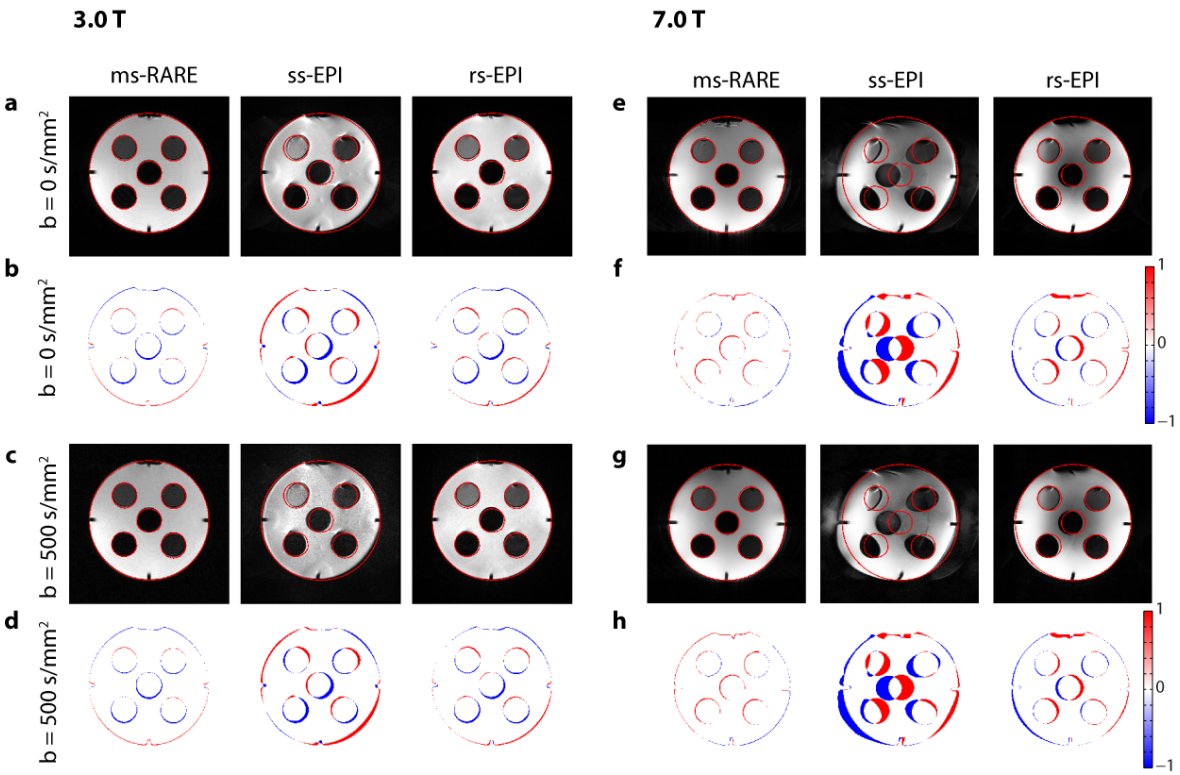

Figure 42: **Assessment of geometric distortions in a static structure phantom**
Images obtained in a structure phantom for a transaxial slice covering five cylinders at 3.0 T (**left column**) and 7.0 T (**right column**) using ms-RARE, ss-EPI and rs-EPI with diffusion weighting of b = 0 s/mm^2 (**a,e**) and of b = 500 s/mm^2 (**c,g**). All images exhibit a spatial resolution of (0.9 x 0.9 x 5.0) mm^3. The red contour represents the geometry of the FLASH reference image which was acquired with the same spatial resolution and matrix size. The red contour was superimposed to all images to assess the degree of geometric distortions. Difference maps with respect to the FLASH reference are depicted for b = 0 s/mm^2 (**b,f**) and b = 500 s/mm^2 (**d,h**) for each approach. Center of gravity analysis revealed a displacement of the center of gravity in pixels with respect to the FLASH reference of $(1.1 \pm 0.2)/(0.9 \pm 0.1)$ for ms-RARE, $(2.7 \pm 1.0)/(8.3 \pm 5.7)$ for ss-EPI and $(1.8 \pm 0.5)/(2.3 \pm 1.4)$ for rs-EPI performed at 3.0 T and at 7.0 T.

These data demonstrate the impediments of the clinically most commonly used DWI pulse sequence ss-EPI in terms of geometric distortions and limited spatial resolution. It has been also shown in these phantom experiments that ms-RARE is a valuable if not superior alternative for diffusion-weighted imaging.

4.3 *In-vivo* diffusion-sensitized multi-shot split echo RARE of the eye and orbit

Recognizing the performance of ms-RARE observed for the phantom experiments this section explores the feasibility of ms-RARE for distortion free diffusion-weighted images of the eye and the orbit. The proposed ms-RARE pulse sequence is assessed *in-vivo* in healthy volunteers at 3.0 T and at 7.0 T. A comparison with ss-EPI and rs-EPI is performed. ms-RARE is applied in patients with intraocular masses at 3.0 T and 7.0 T. The *in-vivo* DWI data are benchmarked against *ex-vivo* imaging which is performed at 9.4 T in the case of enucleation of the eye.

4.3.1 Instrumentation and experimental setup

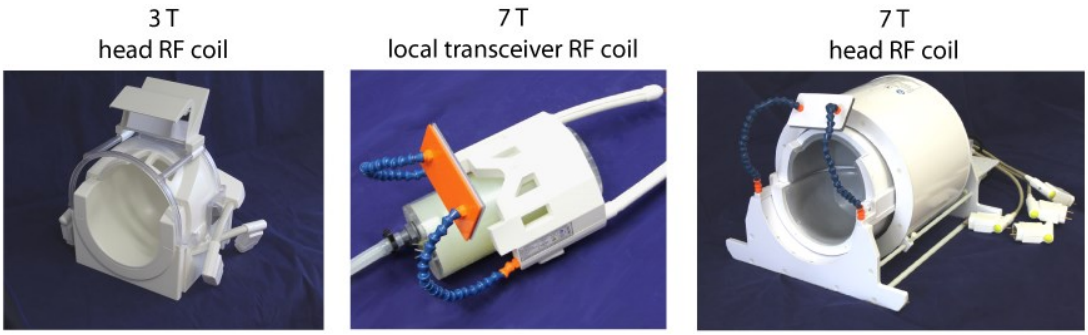

Figure 43: **Photographs of the RF coils used for ophthalmic DWI**
(a): At 3.0 T a commercially available 32 element head RF coil (Siemens Healthcare, Erlangen, Germany) was employed. **(b):** An in-house built 6 channel local transceiver RF coil array dedicated for eye imaging was put to use for imaging at 7.0 T [GRAESSL2014a]. **(c):** For comparison of RF coil performance in terms of signal homogeneity across the eye, a 7.0 T 24 channel head RF coil (Nova Medical, Wilmington, MA, USA) was exploited.

For experiments at 3.0 T a 32 element head RF coil (Siemens Healthcare, Erlangen, Germany) was used. A local 6 channel transceiver RF coil array customized for eye imaging was employed at 7.0 T [GRAESSL2014a] (Figure 43). The performance of these RF coils for eye imaging is illustrated in Figure 44. Signal variation along a profile perpendicular to the line connecting the short axis of the lens with the retina was determined to be approximately 25 % for the 32 channel element head RF coil (1Tx/32Rx) for imaging at 3.0 T. Using the local transceiver RF coil array at 7.0 T (6Tx/6Rx) resulted in a signal variation smaller than 5 % along the same profile. In comparison, the head RF coil (Nova Medical, Wilmington, MA, USA) was used in its volume mode (1Tx/1Rx) and provided a signal variation of approximately 55 % along the specified profile. This underlines the need and value of using a RF coil array tailored for ophthalmic imaging.

Subject preparation included careful positioning of the volunteer and fixation of the head using foam material. The eyelid of the investigated eye was closed using tape to reduce movements in the area of interest [RICHDALE2009]. To reduce motion artifacts due to involuntary eye movement an optoacoustic triggering scheme which consisted of an acquisition window followed by a pause to allow for blinking [BERKOWITZ2001, RICHDALE2009] was employed. The applied device transformed the acoustic events within the triggering scheme into TTL signals for the scanner (easyACT, MRI.TOOLS GmbH, Berlin, Germany [FRAUENRATH2008, FRAUENRATH2009, FRAUENRATH2010]). Subjects were asked to fixate on a cross-hair which was presented on a screen. For this purpose, the employed RF coils are equipped with a mirror to present the visual information to the subject. The fixation period was followed by a resting period that allowed for

blinking. MR data acquisition was interrupted during the resting periods. Alternating fixation-resting periods were repeated until the end of each scan.

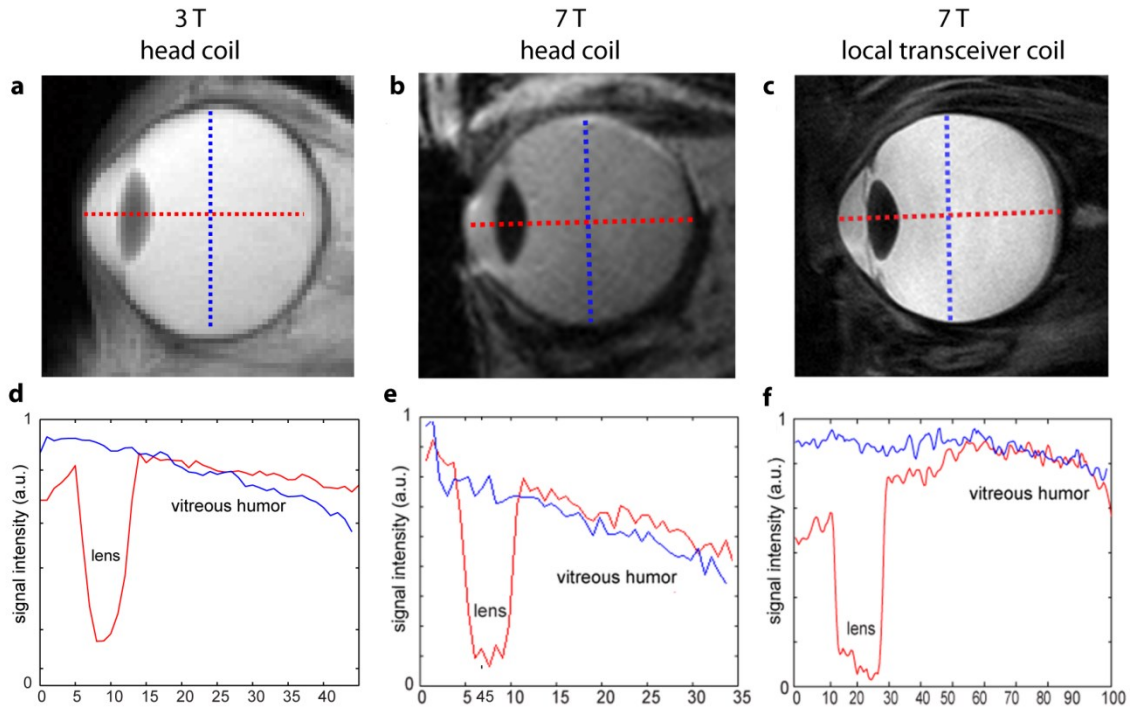

Figure 44: **Assessment of RF coil performance for eye imaging**
T_2-weighted 2D RARE images obtained at **(a)** 3.0 T employing the 1Tx/32Rx head array (Siemens Healthcare, Erlangen, Germany) and at 7.0 T using the **(b)** 1Tx/1Rx configuration of the head RF coil (Nova Medical, Wilmington, MA, USA) and **(c)** the 6Tx/6Rx local transceiver RF coil array customized for ophthalmic MRI. Intensity profiles along a line connecting the short axis of the lens with the retina (marked by the red dotted line) and one perpendicular line (marked by the blue dotted line) are shown in **(d)**-**(f)** for each RF coil configuration. [(b),(c),(e) and (f) are taken from [GRAESSL2014a]]

4.3.2 Quantification of geometric fidelity versus state-of-the-art technology

In a first step, the geometric fidelity of ms-RARE, ss-EPI and rs-EPI for *in-vivo* imaging was assessed. For this purpose *in-vivo* imaging was performed at 3.0 T and at 7.0 T (b = 0 s/mm^2) for two brain slices including (i) a transaxial cranial slice placed parallel to the anterior commissure - posterior commissure (AC-PC) line that covers the cerebral ventricles and (ii) a more caudal, transaxial slice including the eyes and the orbit. At 3.0 T a spatial resolution of (0.9 x 0.9 x 5.0) mm^3 was employed. At 7.0 T the sensitivity gain inherent to the higher magnetic field strength was invested in a reduction of the slice thickness from 5.0 mm to 1.5 mm while keeping the in-plane spatial resolution of (0.9 x 0.9) mm^2. At both magnetic field strengths, volume selective B_0 shimming was applied prior to the imaging protocol to enhance B_0 homogeneity. The next step constitutes the investigation of the propensity to geometric

distortions of diffusion-sensitized ms-RARE, ss-EP and rs-EPI of the eye. ADC mapping of the eyes at 3.0 T was conducted using ms-RARE and both EPI variants applying a spatial resolution of (1.0 x 1.0 x 3.0) mm^3. Diffusion sensitization included six b-values (0, 100, 200, 300, 400 and 500 s/mm^2). Center of gravity analysis was performed for the *in-vivo* ADC maps using the ms-RARE technique as reference. For the center of gravity assessment the brain boundary, the cerebral ventricles and the shape of the eyes were used to define anatomical contours. ADC maps were generated by fitting the data points obtained for a series of b-values to a linear decay after taking the logarithm of the signal intensity. ROI analysis was performed to determine mean ADCs.

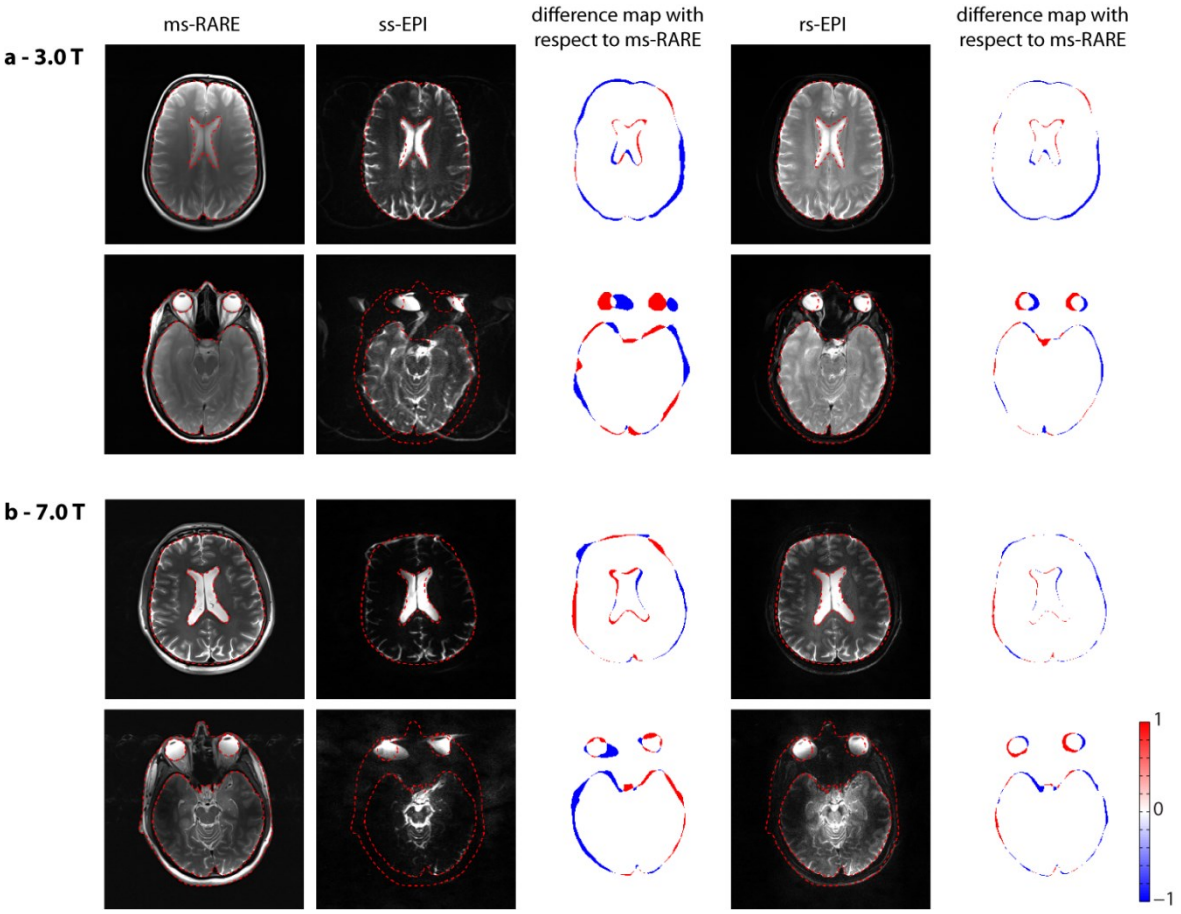

Figure 45: **Assessment of geometric distortions *in-vivo***
In-vivo comparison of non-diffusion-weighted (b= 0 s/mm^2) ms-RARE, ss-EPI and rs-EPI images for two brain slices including (i) a transaxial cranial slice that covers the ventricles and (ii) a more caudal transaxial slice including the eyes and the orbit obtained at 3.0 T (**a**) and at 7.0 T (**b**). The spatial resolution is (0.9 x 0.9 x 5.0) mm^3 for the 3.0 T data and (0.9 x 0.9 x 1.5) mm^3 for the 7.0 T data. For this *in-vivo* scenario the distortion-free ms-RARE acquisitions were taken as a reference. The red contours defined in the ms-RARE images were superimposed to the EPI variants to illustrate the extent of geometric distortions.

Figure 45 summarizes the results obtained for the *in-vivo* assessment of geometric fidelity of ms-RARE and the EPI variants for b = 0 s/mm^2. In the cranial slice which does not cover the eyes and the orbit, ss-EPI images exhibited slight deviations from the actual anatomy at 3.0 T and 7.0 T

as illustrated by the difference maps in Figure 45. Geometric distortions manifested themselves as a mismatch between the ventricle shape and the ventricle contour derived from the ms-RARE reference. Also, the prefrontal cortex and regions close to the sinuses showed distortions which were pronounced at 7.0 T. Unlike ss-EPI, the anatomy of the brain was correctly maintained for rs-EPI images at 3.0 T and 7.0 T. The more caudal slice including the eyes and the orbit showed stronger distortions, particularly for ss-EPI as indicated by the difference maps in Figure 45. The distortions in ss-EPI and rs-EPI primarily occurred in regions where air-filled cavities and sinuses hamper the B_0 homogeneity and hence increase the propensity to geometric distortions. This renders ophthalmic echo-planar imaging challenging at 3.0 T if not prohibitive at 7.0 T.

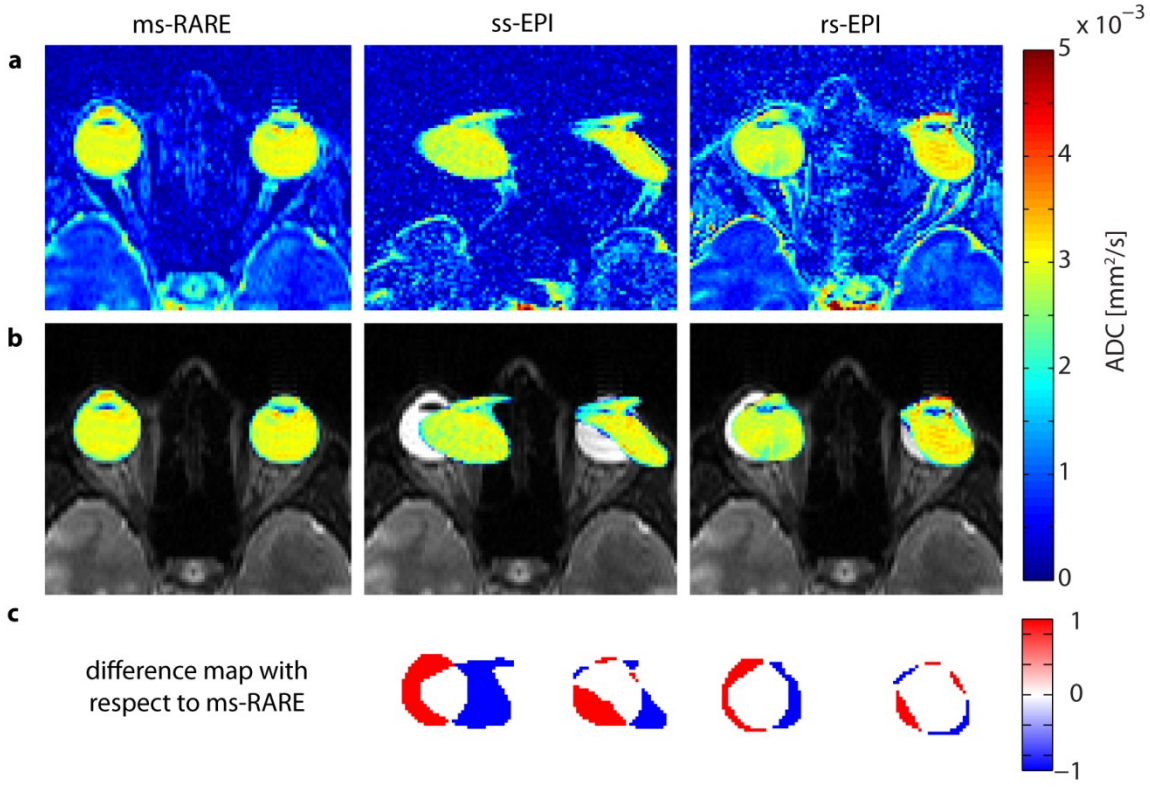

Figure 46: **Comparison of ADC maps of the eyes acquired with ms-RARE, ss-EPI and rs-EPI**
Comparison of ADC maps (**a**) of the eyes calculated from diffusion-sensitized data with b-values up to 500 s/mm^2 at 3.0 T using ms-RARE (**left column**), ss-EPI (**center**) and rs-EPI (**right column**). The spatial resolution is (1.0 x 1.0 x 3.0) mm^3 for all three approaches. The ADC maps were masked to only show the eyes and were superimposed to a T_2-weighted RARE image (b = 0 s/mm^2) used as anatomical reference (**b**). The difference maps with respect to the ms-RARE approach in (**c**) demonstrate the extent of geometric distortions for both EPI variants.

Figure 46 demonstrates that the ADC maps acquired with ss-EPI at 3.0 T showed severe geometric distortions while rs-EPI showed moderate distortions. For ss-EPI the center of gravity of the masked eyes was displaced by (20.2 ± 0.9) pixels versus the ms-RARE reference. In comparison, the displacement was reduced to (11.3 ± 0.8) pixels for the rs-EPI variant. For ms-RARE, no

distortions and no other imaging artifacts were detected as indicated by the match between the ADC maps superimposed to the anatomic reference images (Figure 46b). ROI analysis within the vitreous body of the eye revealed mean ADCs of: $ADC_{ms\text{-}RARE} = (3.02 \pm 0.10)\cdot 10^{-3}$ mm^2/s, $ADC_{ss\text{-}EPI} = (2.89 \pm 0.16)\cdot 10^{-3}$ mm^2/s and $ADC_{rs\text{-}EPI} = (2.84 \pm 0.19)\cdot 10^{-3}$ mm^2/s which compare well with ADCs previously reported for the same compartment using diffusion-weighted ss-EPI of the eye at 1.5 T [ERB-EIGNER2013]. These results confirm the validity of the diffusion weighing used in the proposed ms-RARE.

To summarize, ms-RARE is beneficial over ss-EPI as well as rs-EPI to image the eye and the orbit since it provides high spatial resolution images free of geometric distortion. This capability is of high relevance to image the anatomical details of the eye and the orbit.

4.3.3 Feasibility study in healthy volunteers at 3.0 T

To demonstrate the feasibility of ms-RARE at 3.0 T five healthy volunteers (mean age: (29 ± 3) years, 3 males, 2 females, mean BMI: (22.7 ± 2.1) kg/m^2) without any known history of ocular diseases were scanned. For anatomical reference, T_1-weighted 3D spoiled gradient echo (FLASH) imaging was conducted: TR = 7.6 ms, TE = 2.1 ms, spatial resolution = (0.6 x 0.6 x 0.6) mm^3, matrix size = 256 x 256, receiver bandwidth = 164 kHz, acquisition time = 1:30 min. ms-RARE was performed using the following imaging parameters: TR = 4000 ms, TE = 96 ms, ETL = 16, ESP = 4.84 ms, spatial resolution = (0.5 x 0.5 x 5.0) mm^3, matrix size = 256 x 256, receiver bandwidth = 250 kHz, acquisition time = 0:52 min per b-value. Diffusion sensitization ranging from b = 0 s/mm^2 to b = 398 s/mm^2 was employed. After offline reconstruction of the split echo data including phase correction in case of motion artifacts, an ADC map was calculated using the diffusion-weighted images together with a linear fit to the logarithmized image data.

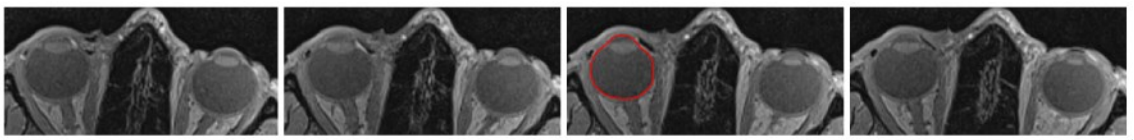

Figure 47: **Images reconstructed from a 3D T_1-weighted acquisition for anatomical reference**
Four reconstructed slices are shown with the second from right being used for DWI. The here defined contour (displayed in red) was used to assess the quality of anatomical depiction in diffusion-weighted images.

Four slices reconstructed from the 3D anatomical reference dataset of an exemplary volunteer are depicted in Figure 47. The second slice from right was chosen for diffusion-weighted imaging. The contour encircling the right eye derived from this image serves as a reference to assess the

geometric fidelity of ms-RARE. Figure 48 displays the diffusion-weighted images exhibiting b-values of 0, 8, 32, 73, 103, 203, 292 and 398 s/mm^2. The contour defined in Figure 47 was transferred to the diffusion-weighted images. The agreement between the contour derived from the reference data and the shape of the eye obtained for ms-RARE demonstrates that ms-RARE affords ophthalmic imaging free of distortion artifacts. No major degradation in image quality due to eye motion was detected for this volunteer. A ROI placed in the vitreous humor of the right eye in the ADC map displayed in Figure 49 resulted in an ADC of $(2.79 \pm 0.16) \times 10^{-3}$ mm^2/s. For the left eye an ADC of $(3.02 \pm 0.11) \times 10^{-3}$ mm^2/s was observed for the vitreous humor. Both values compare well with ADCs previously reported for DWI of the eye using ss-EPI at lower magnetic field strengths ($(2.76 \pm 0.23) \times 10^{-3}$ mm^2/s, [ERB-EIGNER2013]).

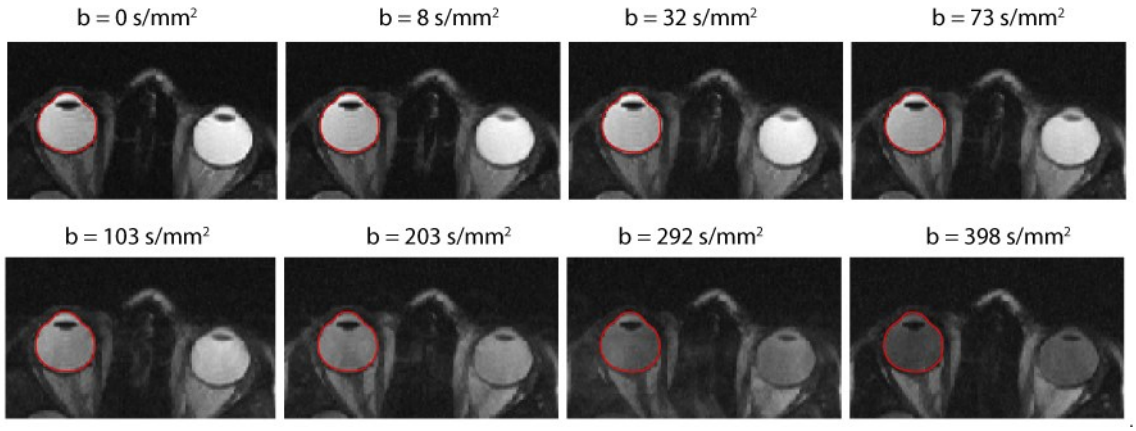

Figure 48: **Diffusion-weighted images of the eyes acquired in a healthy volunteer at 3.0 T**
ms-RARE images acquired with b-values ranging from b = 0 s/mm^2 to b = 398 s/mm^2. For better visualization, the images do not exhibit the same window settings. During acquisition, the right eye was closed with tape while the left eye was open and followed the triggering scheme on the screen. The red contour around the right eye was transferred from the FLASH reference in Figure 47 and demonstrates the capability of ms-RARE to generate distortion free images with high anatomical fidelity.

The overlay of the masked ADC map with the anatomical image using the contour defined in Figure 47 for the right eye and an analog one for the left eye demonstrates the feasibility of accurate co-registration (Figure 49). This is beneficial for the assessment of spatial arrangements of the eye segments and their masses with the ultimate goal to provide guidance during diagnostic assessment and treatment of ophthalmological diseases.

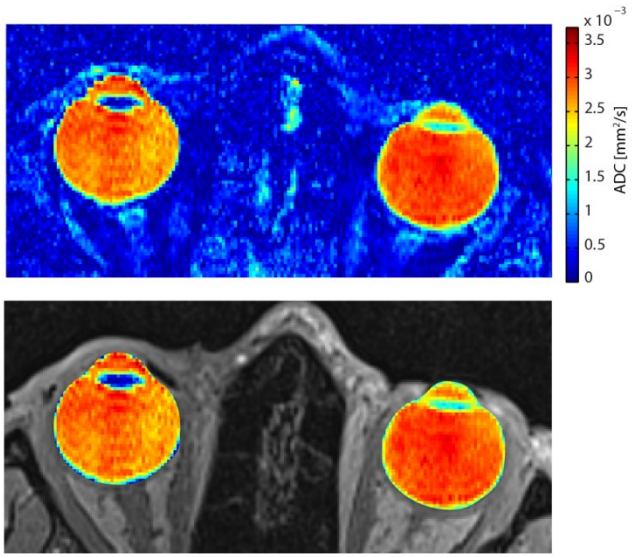

Figure 49: **ADC map of the eyes of a healthy volunteer**
ADC map calculated from the data shown in Figure 48. The eyelid of the closed right eye is clearly visible, while it is not detectable for the open left eye. The lower panel shows an overlay of the masked ADC map with an anatomical image.

Results obtained in two more volunteers out of the feasibility study are presented in Figure 50. Diffusion-sensitized images are shown together with the corresponding ADC map and the overlay of the masked ADC map onto the anatomical images.

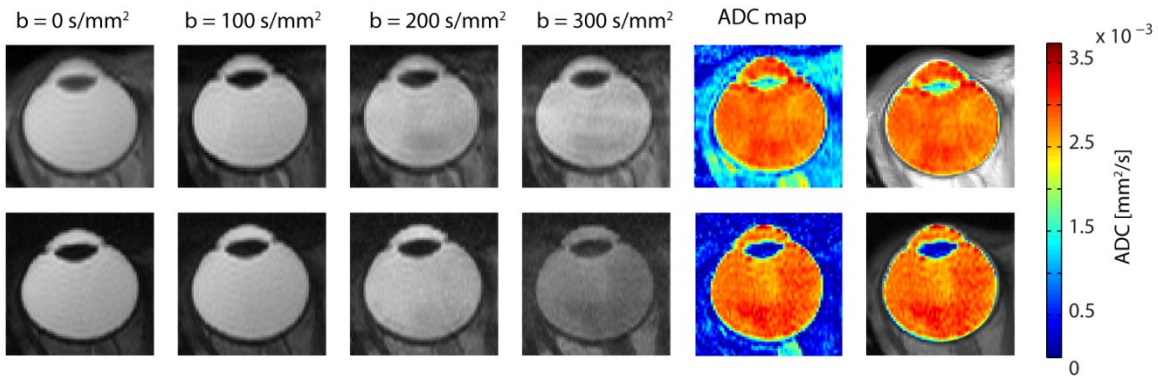

Figure 50: **Results obtained in two more volunteers included in the feasibility study**
Exemplary results derived from two more volunteers included in the feasibility study at 3.0 T using diffusion-weighted ms-RARE. Diffusion-sensitized data with b-values ranging from 0 s/mm^2 to 300 s/mm^2 are shown together with the corresponding ADC map. Overlays of the masked ADC map and the anatomical image demonstrate that no geometric distortions or significant image artifacts were observed.

4.3.4 Feasibility study in healthy volunteers at 7.0 T

Further to the feasibility study at 3.0 T, five healthy volunteers (mean age: (33 $\pm$ 9) years, 3 males, 2 females, mean BMI: (22.5 $\pm$ 1.1) kg/m^2) were examined at 7.0 T to investigate the feasibility of ms-RARE to image the orbit at ultrahigh magnetic field strength. For this purpose, the sensitivity

gain inherent to 7.0 T was invested in an increase in spatial resolution compared to the 3.0 T reference and two spatial resolutions were used: (i) (0.4 x 0.4 x 3.0) mm^3 which constitutes a factor of 2.6 reduction in voxel size versus the 3.0 T reference and (ii) (0.2 x 0.2 x 2.0) mm^3 exhibiting a further reduction in voxel size by a factor of 6.

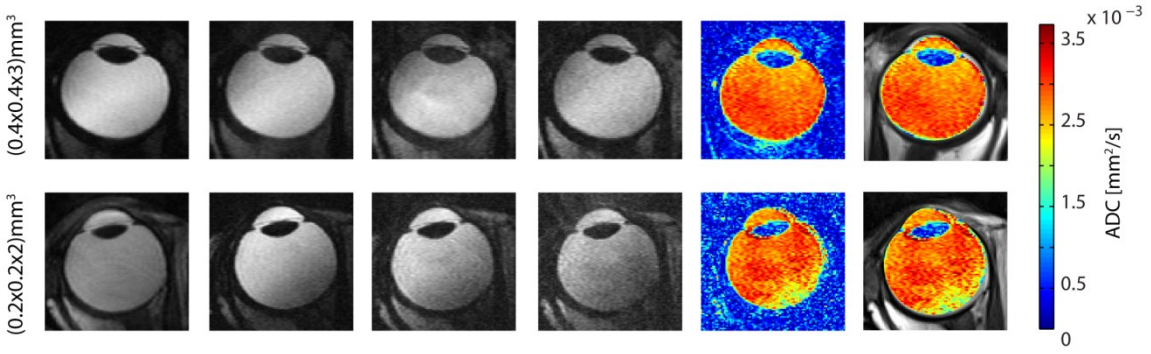

Figure 51: **Diffusion-weighted images of the eye acquired in healthy volunteers at 7.0 T**
Exemplary results derived from volunteers included in the feasibility study at 7.0 T using diffusion-weighted ms-RARE. Diffusion-sensitized data with b-values ranging from 0 s/mm^2 to 300 s/mm^2 are shown together with the corresponding ADC map. Overlays of the masked ADC map and the anatomical image demonstrate that no geometric distortions or significant image artifacts were observed.

Figure 51 summarizes the results obtained within the feasibility study in healthy volunteers at 7.0 T. The two datasets with different spatial resolutions demonstrate that diffusion-weighted ms-RARE provides images of the eyes free of geometric distortion. Notwithstanding the sub-millimeter spatial resolution for the dataset shown in the right column of Figure 51 which embodies a factor of 15 reduction in voxel size versus the 3.0 T reference, no distortions or any other imaging artifacts are observed. These examples underline the applicability of ms-RARE for ophthalmic diffusion-sensitized imaging at ultrahigh magnetic field strength.

4.3.5 Pilot study in patients with ocular masses

Thanks to the collaboration with T. Lindner, O. Stachs, R. Guthoff (Department of Ophthalmology, University of Rostock) and P.-C. Krüger, S. Hadlich, S. Langner (Institute for Diagnostic Radiology and Neuroradiology, University of Greifswald), it was possible to apply the proposed ms-RARE approach in patients (n = 6, mean age: (55 ± 12) years, 4 males, 2 females, mean BMI: (27.5 ± 4.7) kg/m^2) with uveal melanoma and/or retinal detachment at 3.0 T and at 7.0 T as a precursor to larger clinical studies. For this purpose the diffusion-weighted ms-RARE protocol designed for the *in-vivo* feasibility study in healthy volunteers was applied at 3.0 T. High spatial resolution anatomical RARE imaging was conducted at 7.0 T to obtain an anatomical reference with a (0.1 x 0.1 x 1.2) mm^3 spatial resolution.

In one case the diseased eye was enucleated as part of the therapy and afterwards imaged at 9.4 T by Andreas Pohlmann (B.U.F.F.). For this purpose, *ex-vivo* measurements were conducted on a 9.4 T small bore MR system (Biospec 94/20, Bruker Biospin, Ettlingen, Germany). A birdcage volume RF resonator was used for transmission and signal reception. To provide anatomical reference, *ex-vivo* anatomical FLASH imaging was performed. Diffusion-weighted data with b-values of up to 500 s/mm^2 using spin echo imaging were acquired with a spatial resolution of (0.1 x 0.1 x 0.3) mm^3. After *ex-vivo* MR imaging the enucleated globe was fixed in 4% formalin solution for at least 24 hours and sliced afterwards. A macrophotography of the enucleated and bisected eye was produced. Optical microscopy of hematoxylin and eosin (H&E) stainings of various sections of the eye using different magnifications (10-fold and 20-fold) was conducted to characterize the pathology of the eye.

The corresponding results to this exemplary case are shown in Figure 52. Four reconstructed slices of the 3D T_1-weighted anatomical scan are shown in Figure 52a for the normal left eye and for the pathological right eye. These anatomical images clearly show the loss in integrity of the vitreous compartments as a result of retinal detachment. Diffusion-weighted ms-RARE data of the right eye using b-values from 0 s/mm^2 to 600 s/mm^2 are depicted in Figure 52b. The retinal detachment demonstrated hypointense signal for b-values of up to 300 s/mm^2 and is very well delineated even for modest diffusion weighting. For b-values larger than 200 s/mm^2 the tumor becomes detectable as hyperintense mass in the subretinal space. The ADC map clearly delineates the tumor from the surrounding hemorrhage and the vitreous body. Mean ADC of the tumor was $(0.97 \pm 0.15)\cdot 10^{-3}$ mm^2/s. The subretinal hemorrhage revealed an ADC of $(1.67 \pm 0.10)\cdot 10^{-3}$ mm^2/s. For the vitreous body an ADC of $(2.91 \pm 0.10)\cdot 10^{-3}$ mm^2/s was found. These differences in the ADC induced an ample contrast between the subretinal hemorrhage and the tumor. Unlike diffusion-weighted ms-RARE and the ADC maps derived from diffusion-weighted ms-RARE the tumor remained undetectable in high spatial resolution T_1-weighted anatomical data as well as in the T_2-weighted (b = 0 s/mm^2) ms-RARE images. Because of the diffusion-weighted ms-RARE data free of geometric distortion, the ADC map can be conveniently co-registered with the anatomical data to determine the exact position of the ocular mass.

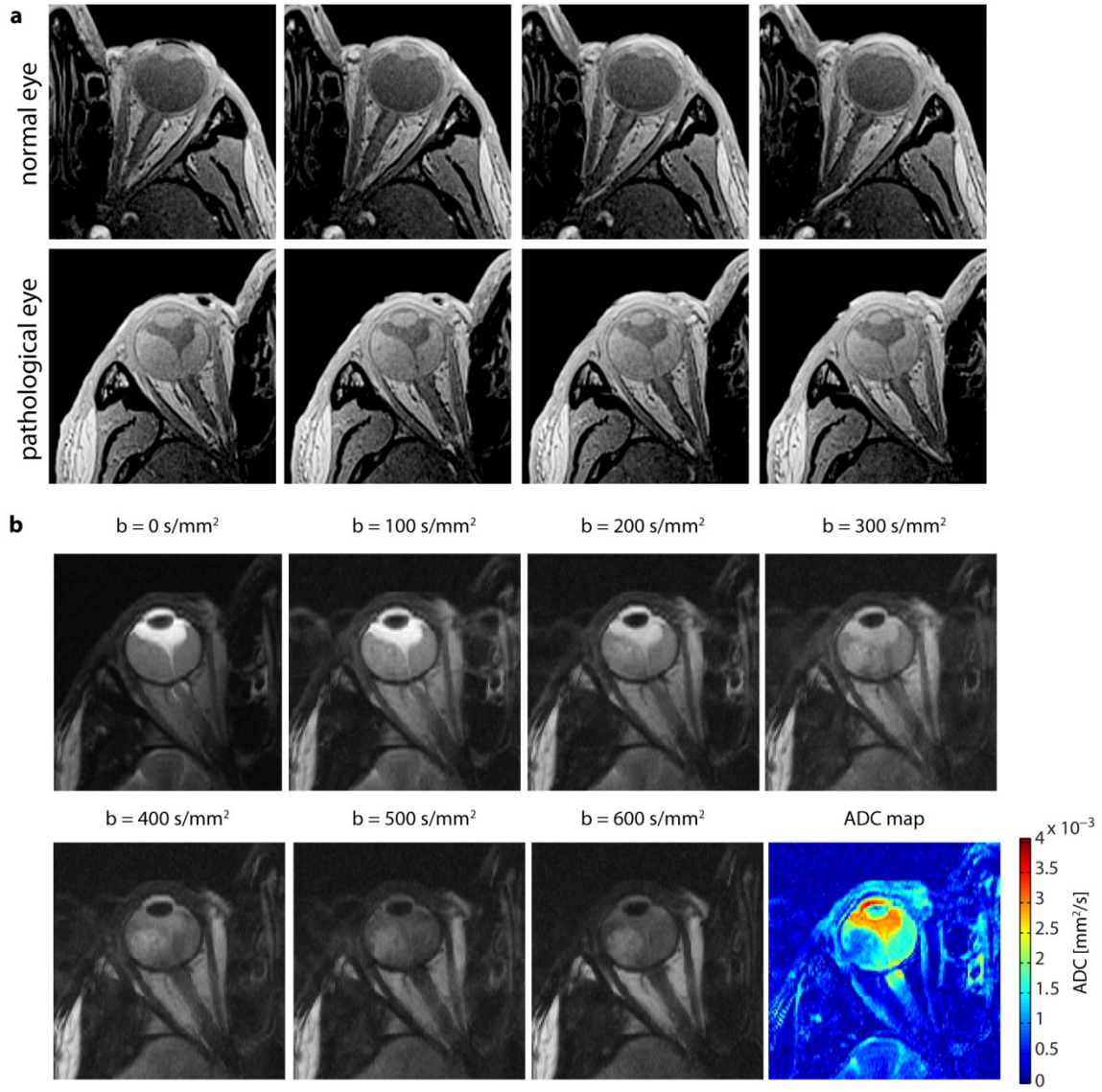

Figure 52: **Anatomical and diffusion-weighted images of the eyes of a patient with a uveal melanoma** (**a**): Four reconstructed slices derived from the 3D T_1-weighted anatomical scan of the normal left eye (1st row) and the pathological right eye (2nd row) showing a retinal detachment. (**b**): Diffusion-weighted images acquired using ms-RARE of the pathological right eye with b-values up to 600 s/mm^2. The corresponding ADC map (**bottom right**) shows reduced ADCs in the area of the subretinal hemorrhage with respect to the vitreous humor and even a lower ADC within the melanoma. The diffusion-weighted images exhibit a spatial resolution of (0.5 x 0.5 x 5.0) mm^3.

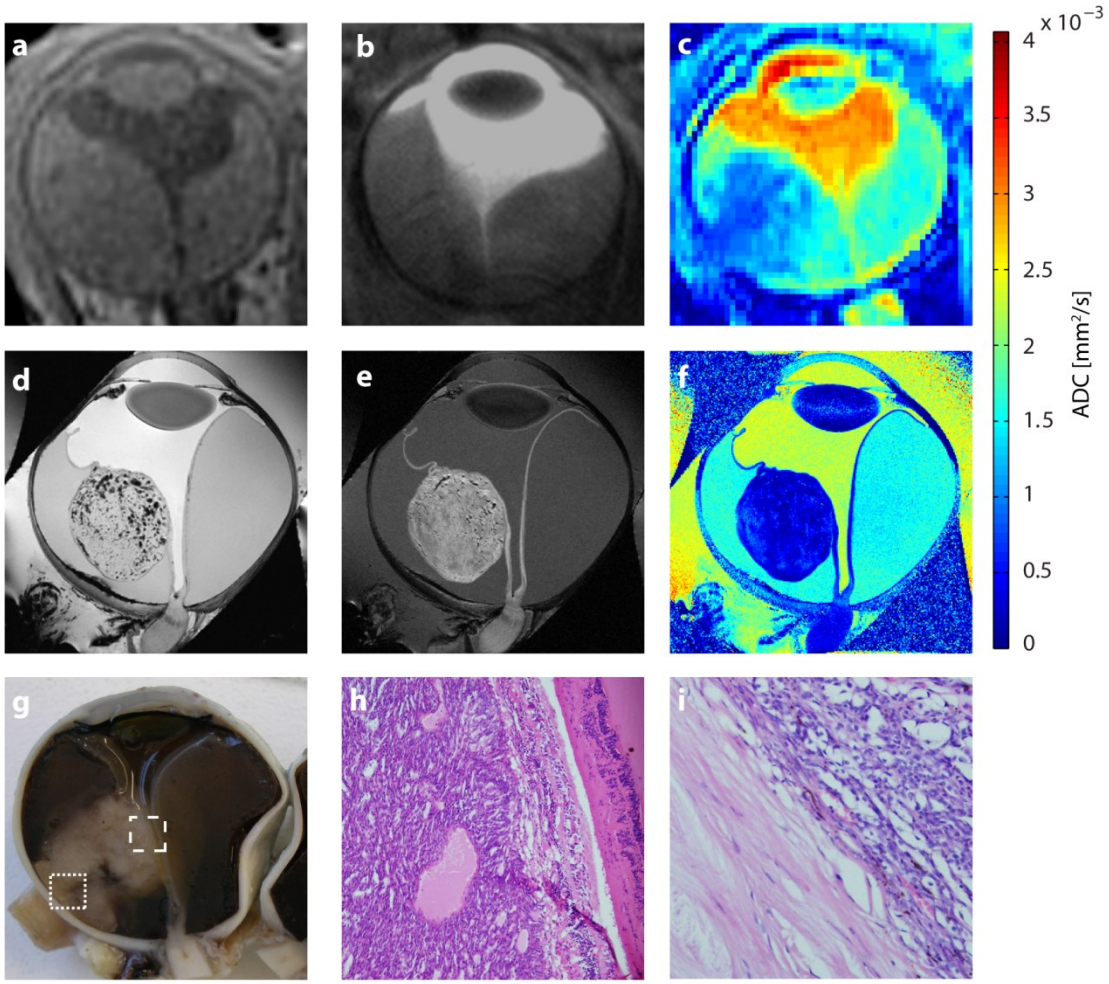

Figure 53: **Synopsis of *in-vivo* and *ex-vivo* imaging modalities**
Comparison of *in-vivo* MR imaging at 3.0 T and at 7.0 T (**a-c**), *ex-vivo* MR microscopy at 9.4 T (**d-f**), macroscopy (**g**) and histology (**h-i**) of the pathological eye studied in Figure 52. (**a**): *In-vivo* T_1-weighted FLASH image acquired *in-vivo* at 3.0 T exhibiting a spatial resolution of (0.6 x 0.6 x 0.6) mm^3. (**b**): *In-vivo* T_2-weighted ms-RARE image obtained at 7.0 T with a spatial resolution of (0.1 x 0.1 x 1.2) mm^3. (**c**): *In-vivo* ADC map acquired at 3.0 T with a spatial resolution of (0.5 x 0.5 x 5.0) mm^3. (**d**): *Ex-vivo* T_2^*-weighted FLASH image acquired at 9.4 T exhibiting a spatial resolution of (0.05 x 0.05 x 0.25) mm^3. (**e**): *Ex-vivo* diffusion-sensitized (b = 500 s/mm^2) spin echo image acquired at 9.4 T with a spatial resolution of (0.1 x 0.1 x 0.3) mm^3. (**f**): Corresponding *ex-vivo* ADC map exhibiting the same scaling as the *in-vivo* map. (**g**): Macrophotography of the enucleated eye. (**h**): H&E staining with 10-fold magnification showing the transition from the ocular mass to the detached retina (dashed box in g). (**i**): H&E staining with 20-fold magnification showing the transition from the sclera to the tumor (dotted box in g).

A comparison of *in-vivo* and *ex-vivo* results for the patient shown in Figure 52 is presented in Figure 53. The *in-vivo* T_1-weighted image acquired at 3.0 T and the *in-vivo* T_2-weighted ms-RARE image acquired at 7.0 T clearly delineate retinal detachment but not the ocular mass (Figure 53a,b). *Ex-vivo* imaging using FLASH at 9.4 T (Figure 53d) increases spatial resolution by a factor of 19 compared to *in-vivo* T_2-weighted imaging at 7.0 T. *Ex-vivo*, retinal detachment as well as the

tumor itself can be clearly depicted. The fine structure of the tumor is even more pronounced when using high spatial resolution diffusion-weighted MR microscopy at 9.4 T (Figure 53e). The vitreous body showed an *ex-vivo* ADC of $(2.21 \pm 0.12) \cdot 10^{-3}$ mm^2/s. In comparison, the subretinal hemorrhage revealed an *ex-vivo* mean ADC of $(1.49 \pm 0.13) \cdot 10^{-3}$ mm^2/s. For the tumor an *ex-vivo* ADC of $(0.35 \pm 0.20) \cdot 10^{-3}$ mm^2/s was found. Although the voxel size of the *in-vivo* ADC map acquired at 3.0 T (Figure 53c) was 2000 times larger compared to that of the *ex-vivo* MR microscopy (Figure 53f), the ocular mass was still clearly identifiable in the *in-vivo* ADC map. Macrophotography of the enucleated eye confirmed the retinal detachment and the extent of the tumor. Histology confirmed the malignancy of the melanoma and its diverse tissue composition including the presence of intratumoral hemorrhage, lymphoid vessels and interlaced fiber bundles as demonstrated by ADC mapping *in*- and *ex-vivo*.

4.4 Summary and Discussion

In this chapter, the feasibility of diffusion-weighted multi-shot RARE for ophthalmic DWI free of geometric distortion at 3.0 T and 7.0 T has been demonstrated. Techniques based on RARE offer immunity to B_0 inhomogeneities and, hence, are particularly suited for ophthalmic DWI. This is of clinical relevance since ss-EPI, which is commonly used for DWI in today's clinical practice, is prone to magnetic susceptibility artifacts induced by the air-filled nasal cavities and frontal sinuses surrounding the eye. This effect infringes the geometric integrity and is even present at 1.5 T which showed image distortion prevalent of DWI-EPI of the eye in a recent study [ERB-EIGNER2013]. The propensity of ss-EPI to geometric distortions is exacerbated at both 3.0 T and 7.0 T, as shown in this chapter, and constitutes a severe obstacle for diffusion-sensitized EPI of the eye and orbit at (ultra)high magnetic fields. State-of-the-art rs-EPI versions help to enhance geometric fidelity of ophthalmic DWI at 3.0 T and 7.0 T. However, it has been shown in this thesis that rs-EPI still has some setbacks in eliminating image distortion. Multi-shot RARE's quality of imaging free of geometric distortions underscores its value for advancing the capabilities of DWI of the eye and orbit. Further to ocular imaging, diffusion-sensitized ms-RARE holds the promise for targeting and imaging deeper lying sections of the orbit, the optical canal, and the optic nerve. Diffusion-weighted imaging of the optic nerve bears clinical relevance for optic neuropathies in neuroinflammatory diseases and also for the differential diagnosis of debilitating autoimmune or orphan diseases of the central nervous system that run the risk of visual impairment [SINNECKER2012, WUERFEL2012].

Magnetic resonance imaging of subtle ocular structures requires a millimeter to submillimeter in-plane spatial resolution over a small FOV [PATZ2007]. Realizing this constraint, the benefits of

the sensitivity gain inherent to (ultra)high magnetic field MR were translated into spatial resolution enhancements and reduction in scan time at 3.0 T and 7.0 T versus the kindred counterpart at 1.5 T. Ophthalmic DWI-EPI studies at 1.5 T reported the use of 8 to 10 averages to support a spatial resolution with a voxel size of 4 mm^3 [ERB-EIGNER2013]. The 3.0 T setup used in this thesis supported a voxel size of 1.2 mm^3 in a single average ms-RARE acquisition. For the 7.0 T setup, a voxel size of approximately 0.1 mm^3 was achieved using a single average ms-RARE acquisition. The latter corresponds to a factor of 40 enhancement in spatial resolution versus clinical protocols used at 1.5 T [ERB-EIGNER2013] and brings us closer to *ex-vivo* MR microscopy images acquired at 9.4 T. Furthermore, scan time was shortened by an order of magnitude compared with the 1.5 T DWI-EPI reference [ERB-EIGNER2013].

It is a recognized limitation that the current ms-RARE implementation puts 1D linear navigator correction to good use. Unknown phase shifts induced by diffusion sensitization gradients or by eye motion might vary from shot to shot and might cause ghosting artifacts in the resulting image which contains combined information originating from all shots. The extension to 2D linear navigation improves phase correction results [BUTTS1996, ATKINSON2000]. Further gain can be achieved by using a 2D non-linear phase correction [PORTER2009]. Combining this correction algorithm with a reacquisition technique to identify data that cannot be properly corrected in the first run increases the power and robustness of the correction procedure. Incorporation of these strategies into ms-RARE offers further improvements in image quality. This becomes relevant for broad-scale patient studies that might include patients uncompliant with the triggering scheme customized for keeping involuntary eye motion at a minimum.

It is also a recognized limitation that the 1D linear phase correction restricts the diffusion sensitization gradients to the phase encoding axis and hence limits the maximum achievable b-value. Expanding the phase correction to the slice and readout axes would facilitate an increase in the maximum b-value because the diffusion sensitization gradients can be distributed along all 3 encoding axes. This would afford b-values of up to 1000 s/mm^2 which are commonly used for clinical DWI of stroke and other brain diseases. The current ms-RARE implementation uses a pair of unipolar Stejskal-Tanner gradients [STEJSKAL1965] which helps to balance diffusion sensitization time and diffusion sensitization strength. However, pairs of unipolar gradients are not motion compensated and can be prone to eddy current related artifacts. Pairs of bipolar diffusion sensitizing gradients or twice-refocused gradients offer those features but come with a less effective sensitization [HONG1992, NIENDORF1996, REESE2003].

Although ocular DWI is still an emerging area [NIENDORF2014], it may be expected to continue to drive further technological developments. The application of double echo RARE techniques like 2in1-RARE, which afford a simultaneous combination of anatomical contrast (proton density or T_2 weighting) and diffusion weighting [FUCHS2014b], provides opportunities to advance the capabilities of ocular MRI with ms-RARE. Generating two contrasts simultaneously within one acquisition offers substantial scan time reduction. This is of benefit not only in a clinical scenario but also in preclinical studies of the eye and the orbit where multiple parameters and contrasts are assessed. Moreover, simultaneous acquisition of multiple contrasts obviates the need for slice co-registration when combining multiple series of images with anatomical (T_2 or proton density) and functional (DWI) contrast which would be beneficial for ophthalmic MRI dealing with eye motion. The use of self-calibrated parallel imaging techniques tailored for RARE imaging presents another opportunity to extend the capabilities of ms-RARE [KLIX2014]. For this purpose, the full echo of coherent RARE needs to be decomposed into two parities which can be independently phase encoded using (a) regular sampling to derive coil sensitivity profiles and (b) k-space undersampling for accelerated DWI acquisitions. One practical implication is that the speed gain of self-calibrated ms-RARE would help to reduce examination times while improving both operator convenience and patient comfort. Slice accelerated acquisition schemes using power independent of number of slices (PINS) RF pulses, which perform spatially periodic excitation and refocusing, provide means for improving imaging speed and spatial coverage while relaxing RF power deposition in RARE based imaging at 7.0 T [NORRIS2011].

The high spatial resolution requirements and the diffusion sensitization of ophthalmic MRI are likely to motivate further advancements in the gradient coil performance which today commonly provide a maximum gradient strength of 40 to 45 mT/m for clinical MR scanners, a constraint that governs the extent of spatial resolution, minimum echo time, and maximum diffusion weighting. Previous reports suggest that gradient inserts help to further enhance maximum gradient strength across the target anatomy [WONG2012]. To this end, the engineering and early application of gradient systems that provide a maximum gradient strength of up to 300 mT/m [MCNAB2013] and diffusion sensitization far beyond b = 1000 s/mm^2 provide encouragement for improvements which would help to relax the competing constraints between minimum echo time, SNR and maximum b-value experienced in this thesis. It is also possible to consider adding local planar or shaped high-performance surface gradient RF coils to the head for ophthalmic DWI. Another development that is looming on the UHF-MR research horizon is the move toward ophthalmic imaging at 9.4 T and higher magnetic field strengths which will afford further spatial resolution

enhancements that might help to approach the spatial resolution used in the *ex-vivo* MR microscopy.

The promising results obtained for ophthalmic diffusion-weighted imaging using ms-RARE raise the question if the technique can be used to image other target regions in which the application of ss-EPI is also challenging. One example is diffusion-weighted imaging of the heart which is an overall challenging technique. The application of ms-RARE is compromised by various reasons. First, since the heart is beating and performing rotations and contractions during each cardiac cycle, the phase variation from shot to shot is extremely large and complex. Hence, it is challenging if not impossible to correct for these phase errors. Second, it is of high importance to apply diffusion sensitization at an optimal time point during the cardiac cycle to avoid superposition of diffusion related signal variations and those generated by bulk motion. It has been shown that for this purpose the systolic phase is favorable over the diastolic phase [GAMPER2007]. Despite the larger bulk motion during systole, the myocardium is thicker and relaxes spatial resolution requirements. Furthermore, the duration (≈ 300 ms) and position of the systolic phase during the cardiac cycle is more reproducible. Tagging data provided information about rotation and contraction during systole and revealed that during the first half of systole mainly rotation occurs while contraction primarily takes place in the second half of systole [LORENZ2000]. The second half of systole turned out to be the best time point to apply diffusion sensitization [GAMPER2007]. Of course, this time period is rather short (≈ 150 ms). Since the diffusion sensitization is directly linked with the imaging part of the pulse sequence, which should ideally be positioned in late diastole, the freedom of timing within the cardiac cycle is further limited. Hence, the application of a multi-shot DWI pulse sequence for the generation of reliable cardiac diffusion-weighted images is not straightforward and up to now not realized.

To summarize, it has been shown in this chapter that diffusion-sensitized multi-shot RARE has the capability to acquire high contrast, high spatial resolution, distortion-free images of the eye and orbit in healthy subjects and patients. The results underline the challenges of ocular imaging at 3.0 T and 7.0 T when using echo planar based imaging modules and demonstrate that these issues can be offset by using RARE based imaging techniques. It was shown that RARE based techniques offer immunity to B_0 inhomogeneities and hence are particularly suited for ophthalmic DWI. The benefits of such improvements would be in positive alignment with the needs of explorations that are designed to examine the potential of (ultra)high magnetic field MRI of the assessment of spatial arrangements of the eye segments and their masses with the ultimate goal to provide guidance during diagnostic assessment and treatment of ophthalmological diseases.

5. Development of cardiac Rapid Acquisition with Relaxation Enhancement Imaging at 7.0 Tesla

Inversion recovery prepared black blood RARE techniques [SIMONETTI1996] are commonly used for anatomical and morphological imaging of the heart and large vessels [SIMONETTI1996, HUNDLEY2010]. Clinical applications also include probing for myocardial edema [ABDEL-ATY2004, ABDEL-ATY2007a, ABDEL-ATY2009, H-ICI2012], assessment of amyloidosis [WASSMUTH2011] and noninvasive myocardial tissue characterization using parametric mapping [HEINRICHS2009].

Ultrahigh field cardiovascular MR (UHF-CMR) applications become increasingly used for research and should help to advance the capabilities of MRI for the assessment of cardiovascular diseases. The SNR gain inherent to UHF-CMR holds the promise to enhance spatial and temporal resolution. Such improvements can foster the assessment of cardiac morphology and tissue characterization using RARE imaging. Unfortunately, the image quality achievable at UHF is not always exclusively defined by SNR considerations. As a deep-lying organ surrounded by inhomogeneous tissue structures within the comparatively large volume of the thorax, the heart is particularly susceptible to wavelength-related RF field focusing and transmission field non-uniformities that accompany UHF MR. Additional RF power deposition constraints render UHF-CMR challenging. In particular, RARE imaging at 7.0 T presents a special challenge due to the train of high peak RF power refocusing pulses. Recognizing the constraints and opportunities of high spatial resolution RARE based black blood imaging at 7.0 T the challenge was accepted and the feasibility of anatomical cardiac RARE imaging at 7.0 T is demonstrated in this chapter.

Going one step further, the feasibility of RARE based T_2^* mapping of the heart at 7.0 T as a tool for noninvasive myocardial tissue characterization was investigated with the results being presented in this chapter.

Parts of this section have been published in [FUCHS2013] and [FUCHS2014c]. Driven by the motivation to transfer double inversion recovery prepared black blood RARE imaging from clinically established magnetic field strengths to UHF-CMR, the project has been conducted. These efforts included the independent research for alternative fat suppression methods, the following implementation into the pulse sequence and its evaluation in phantom experiments. Considerations on the inversion recovery preparation module have been undertaken with the goal to improve the blood suppression. T_2^* weighting has been included into the pulse sequence to

enable myocardial tissue characterization based on susceptibility differences. Using the hardware developed within the working group, the *in-vivo* feasibility study and data collection on T_2^* mapping have been performed independently.

5.1 Instrumentation

5.1.1 Multi-channel radiofrequency coil technology tailored for cardiac MR

Since the advent of experimental whole body 7.0 T MRI scanners ultrahigh magnetic field MR is driven by development of novel hardware and imaging methodology. These efforts include explorations into local transceiver surface RF coils dedicated for specific applications. The following considerations concentrate on cardiac transceiver RF coils which constitute the basic requirement for cardiac imaging at 7.0 T. Our group developed four-, eight-, sixteen- and thirty-two-channel transmit/receive RF coil arrays consisting of loop elements dedicated for anatomical and functional cardiac imaging at 7.0 T [DIERINGER2011, GRAESSL2011, THALHAMMER2012, WINTER2012, GRAESSL2014b]. A two-dimensional RF coil design together with a large number of transmit/receive elements showed superior performance versus one-dimensional layouts including enhanced degrees of freedom for B_1^+ modulation and improved parallel imaging performance. It has been shown, that dipole antennas – designated as radiative elements – provide improved SNR and increased B_1^+ efficiency at ultrahigh magnetic field strengths when compared to loop elements or stripline designs [RAAIJMAKERS2011, IPEK2012]. Electrical dipoles hold the benefit that the RF energy is directed perpendicular to the dipole along the Poynting vector to the subject. As a result, the excitation field is symmetrical with respect to the central axis of the radiative element and uniform with increased depth penetration [RAAIJMAKERS2011]. To exploit the advantages of dipole antennas together with the capabilities of two-dimensional arrays, a 16-channel transceiver dipole array for UHF-CMR has been developed [GRAESSL2013]. The applied dipole is bow tie shaped and immersed with deuterium oxide (D_2O) to shorten the length of the dipole (Figure 54a) [WINTER2013]. The cardiac array consists of 16 dipole elements, distributed in two rings of eight elements around the upper torso (eight elements posterior, eight elements anterior) (Figure 54b). All 16 elements are supplied with equal-intensity signals, while phase adjustments are achieved by inserting phase-shifting coaxial cables into the setup. The Poynting vectors of the single dipole elements of the cardiac array point circularly to the heart, providing a beneficial excitation field for cardiac imaging.

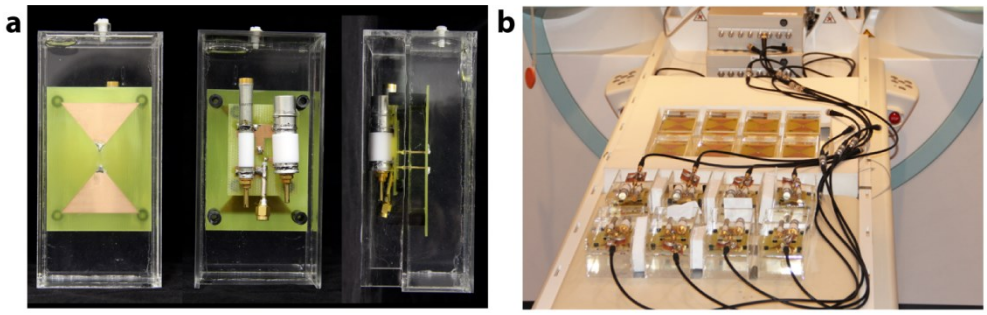

Figure 54: **16 channel bowtie cardiac array**
(a): Picture photographs from the front, back and side of the bow tie antenna building block [WINTER2013].
(b): Setup of the 16-element dipole RF coil array on the patient table [GRAESSL2013].

The bow tie antenna RF coil array was employed for the *in-vivo* feasibility study in healthy volunteers outlined in this chapter. One recognized limitation of the design is the gap between the two rings resulting in limited reception efficiency. This can be offset by including additional meander shaped dipole receive elements into the setup [OEZERDEM2013]. A less sophisticated but more straightforward way is to use one ring which reduces the number of elements to eight. With this approach the anatomic coverage along the head-feet direction is reduced versus a two ring 16-element configuration but still is large enough to cover the entire heart. The 8-channel bow tie approach was applied for T_2^* mapping of the myocardium to ensure uniform B_1^+ across the heart. For the preliminary patient data presented here, a 16-channel loop array was employed [THALHAMMER2012].

5.1.2 Synchronisation of data acquisition with cardiac motion

The heart, in general, is a challenging target object for MRI. It is a deep lying organ surrounded by various tissue types, including air contained in the lungs. Respiratory motion is dealt with restricting the data acquisition to short breath holds which reduce if not eliminate the displacement of the diaphragm during data acquisition. Cardiac motion has a major impact on the data acquisition regime. Image artifacts due to motion related to cardiac activity are suppressed by synchronizing data acquisition with the cardiac cycle. The synchronization requires reliable information about cardiac activity. Various strategies including electrocardiogram (ECG) [LANZER1985, FISCHER1999, CHIA2000], finger plethysmography [LANZER1984]/pulse oximetry (POX), motion induced changes in the impedance match of RF coils [BUIKMAN1988] and self-gating techniques [CROWE2004, LARSON2004, BUEHRER2008, NIJM2008] have been applied for synchronization of data acquisition with the cardiac cycle. In current clinical practice, ECG is the most commonly used gating and triggering technique. The underlying concept is the detection of the R-peak of the ECG that marks the onset of the cardiac cycle. At high and ultrahigh magnetic

field strengths, ECG being an electrical measurement is corrupted by magnetohydronynamic (MHD) effects (Figure 55) [FRAUENRATH2009, SNYDER2009, BECKER2010]. The MHD effect creates electric potential which is mainly related to blood flow in the aorta and in the heart ventricles. The ECG is superimposed by this potential which is at maximum during systole since blood flows most rapidly while the heart is contracting. As a result, an elevation in the area of the T-wave of the ECG occurs which is prone to be mis-detected as an R-peak. This mis-registration hampers synchronization of the data acquisition with cardiac activity which compromises the image quality in cardiac imaging due to cardiac motion induced blurring.

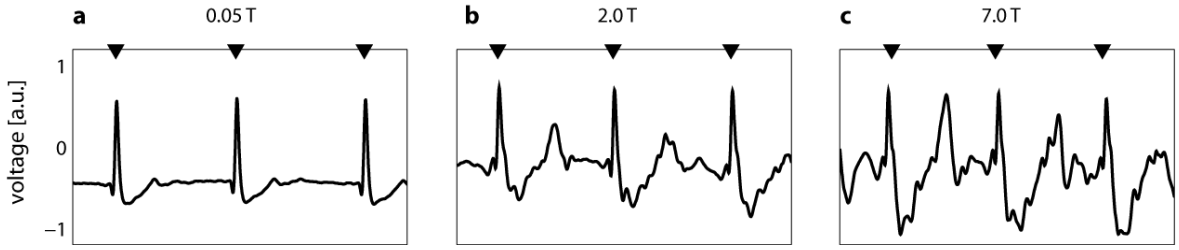

Figure 55: **ECG curves at different magnetic field strengths**
ECG recordings acquired at **(a)** 0.05 T (fringe field position approximately 7 m away from the isocenter of the 7.0 T magnet, **(b)** 2.0 T (patient table of the MR scanner at home position) and **(c)** 7.0 T (isocenter). The measurements provide waveforms which represent a combination of the ECG and the MHD effect. With decreasing magnetic field strength the MHD effect diminishes.

As an alternative technique, an MR-stethoscope which uses the phonocardiogram as signal input has been proposed [FRAUENRATH2008]. The algorithm detects the first heart tone which occurs at the beginning of systole and possesses a maximum latency of 35 ms with respect to the ECGs R-wave [FRAUENRATH2010]. Acoustic cardiac triggering (ACT) has been applied at 1.5 T, 3.0 T and 7.0 T [FRAUENRATH2009, FRAUENRATH2010]. Left ventricular function assessment has been performed at 1.5 T and 3.0 T comparing ECG and ACT gating [BECKER2010]. Evaluations revealed severe ECG distortions which induced mis-registration of the ECG, especially at 7.0 T. The phonocardiogram was reported to be immune to interferences with electromagnetic fields and to provide reliable and stable trigger information (Figure 56).

The acoustic approach has been used for triggering and gating purposes in all cardiac measurements described in this chapter.

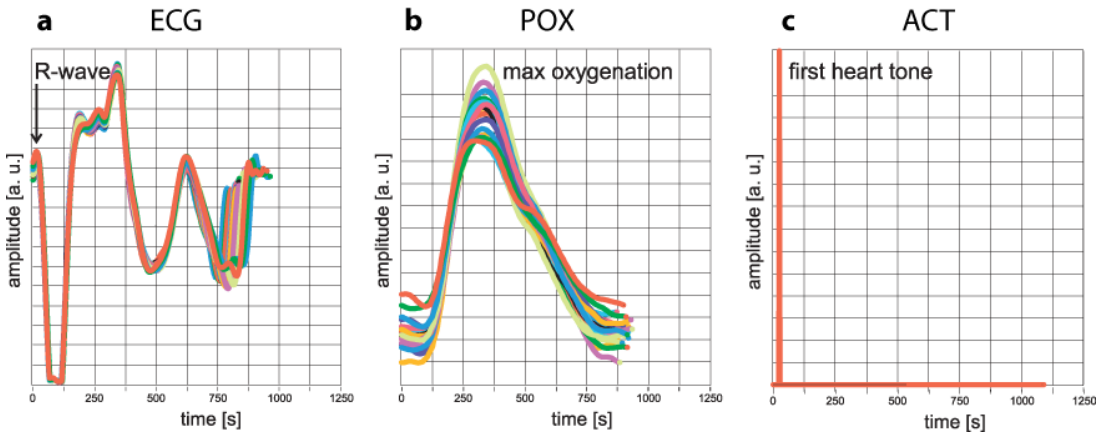

Figure 56: **ECG, POX and ACT at 7.0 T**
Signal waveforms obtained at 7.0 T using ECG **(a)**, pulse oximetry **(b)** and the phonocardiogram **(c)** over the time period of 18 cardiac cycles ([FRAUENRATH2010]).

5.2 Fat suppression with slice selection gradient reversal methodology

RARE images exhibit high signal originating from fat. Image quality can be diminished since the dynamic range is mainly determined by the strong fat signal. The high fat signal can compromise the diagnostic assessment since pathologies showing modest hyperintense signal might be masked by the high fat signal. This is of importance for cardiac imaging since subcutaneous fat from the chest wall and epicardial fat are close to the target organ.

Various fat suppression techniques were proposed which can be classified into three groups. The first type of fat suppression makes use of the specific short T_1 of fat which differs from T_1 of blood and myocardium. Short tau inversion recovery (STIR) applies a slice selective 180° refocusing RF pulse. The inversion time is adjusted so that the imaging module, i.e. the excitation pulse, is started when $M_z = 0$ for the fat signal. Combining STIR with the double inversion recovery (DIR) preparation module for blood suppression yields a triple inversion recovery (TIR) preparation [SIMONETTI1996] with the first inversion time being adjusted to suppress blood and the second one to suppress fat. TIR prepared RARE enhances the water signal and has been applied for the diagnosis of acute myocardial infarction with increased contrast between edema and healthy myocardium [ABDEL-ATY2007b].

The second group of fat suppression techniques is based on the difference in proton resonance frequency between fat molecules and water or other tissues. These methods, e.g. fat saturation (fatSat) or water excitation, apply a spectrally selective RF pulse to distinguish between fat and other tissues. The use of inversion or spectrally selective RF pulses constitutes a challenge at ultrahigh magnetic field strengths due to B_1 and B_0 inhomogeneities. The third group makes use of the advantages of the first and second group. Spectral Adiabatic Inversion Recovery (SPAIR)

applies a spectrally selective adiabatic inversion RF pulse to only invert fat spins. At $M_z = 0$ for the fat signal the imaging module starts so that fat spins do not contribute to the transversal magnetization.

An alternative fat suppression approach which falls into the second group is the slice selection gradient reversal (SSGR) approach [PARK1987, VOLK1987, GOMORI1988]. This approach does not require extra spectrally selective RF pulses but puts the slice selective RF pulses to good use for fat suppression. Due to the chemical shift between water and fat (3.5 ppm) a displacement occurs between excited slices for the different tissue types:

$$D = \frac{\delta B_0}{G} \qquad [53]$$

The displacement of the excited (or refocused) fat slice with respect to the water slice is given by equation [53], where δ is the chemical shift between fat and water in ppm, B_0 is the main magnetic field in T and G is the gradient strength of the slice selection gradient in mT/m. Equation [53] implies that the performance of SSGR increases with higher magnetic field strength and that the technique is limited by the slice thickness. If the polarity of the slice selection gradient of the excitation RF pulse is reversed with respect to the refocusing RF pulse, the displacement of the excited and the refocused fat slice is opposed (Figure 57). If the degree of displacement fulfills the condition D > (½ slice thickness), no signal originating from fatty tissue will be present in the final image.

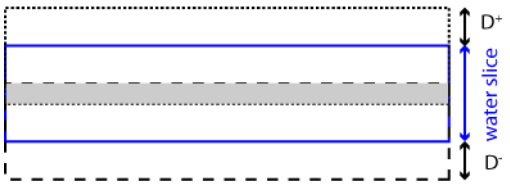

Figure 57: **Scheme of the slice selection gradient reversal technique**
The displacement D^- for the excited fat slice and D^+ for the refocused fat slice take place in opposite directions. Only signal originating from the grey shaded area will be acquired. [Figure adapted from [NAGY2008]]

Figure 58 shows phantom images acquired at 7.0 T without any fat suppression technique (a), with the SSGR approach (b) and with commercial implementations of fatSat (c) and SPAIR (d). The phantom contains sunflower oil, water, acetone and DMSO (clockwise from the upper right). The suppression of the sunflower oil was taken as a quality measurement for the different techniques. Figure 59 shows the signal intensity along a vertical profile covering the sunflower oil tube.

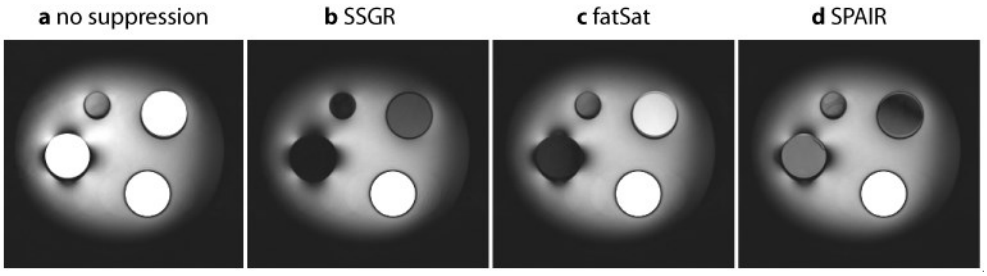

Figure 58: **Comparison of fat suppression techniques at 7.0 T**
Phantom images without fat suppression (a), with SSGR (b), fatSat (c) and SPAIR (d). The phantom contains sunflower oil, water, acetone and DMSO (clockwise from the upper right). The degree of suppression within the sunflower oil tube is taken as a quality measurement for the respective suppression technique.

The images and signal profiles demonstrate that the fatSat technique which relies on the spectral excitation and subsequent spoiling of excited fat spins does not provide satisfying fat suppression (66% fat suppression efficiency versus the reference without fat suppression technique). The application of SPAIR or SSGR results in a fair suppression of the sunflower oil. In case of SSGR an averaged fat suppression efficiency of approximately 92% was achieved. For the SPAIR approach an averaged fat suppression efficiency of approximately 95% was accomplished (Table 11). Notwithstanding this success fat suppression with SPAIR was found to be rather non-uniform across the tube containing sunflower oil amounting to a signal variation of 95% along a profile across the tube. For the same profile the SSGR approach showed a 45% variation in fat suppression efficiency which is reflected by a more uniform image.

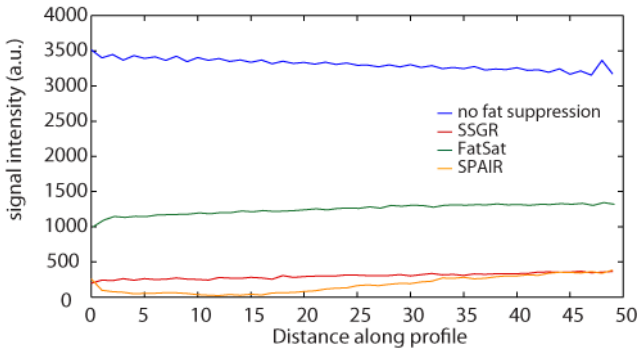

Figure 59: **Signal intensity for sunflower oil for different suppression techniques**
The signal intensity along a vertical profile within the tube containing sunflower oil is illustrated for the acquisition without any fat suppression (blue), with SSGR based fat suppression (red), with fatSat fat suppression (green) and with fat suppression using SPAIR (orange).

It is conspicuous that the SSGR technique not only suppresses the sunflower oil but also the signal in the acetone and DMSO tubes. The reason is that the chemical shift between water and acetone is 2.8 ppm while water and DMSO exhibit a chemical shift of 3.3 ppm [HOFFMAN2006]. These chemical shifts are close to the chemical shift between water and fat. With this insight it is no surprise that the signal of DMSO and acetone is affected by the SSGR suppression technique. It

should be noted that the water signal intensity is not affected by the SSGR approach at all as outlined in Table 11.

Table 11: **SNR comparison for different fat suppression techniques**
Absolute SNR is noted for an acquisition without any suppression as well as for SSGR, FatSat and SPAIR for four different materials. The remaining signal in % is given for the three different suppression techniques with respect to the measurement without suppression.

	No suppression	SSGR		FatSat		SPAIR	
Water	543 ± 40	545 ± 30	100.3%	532 ± 28	97.8%	569 ± 26	104.6%
Sunflower oil	506 ± 11	42 ± 5	8.3%	171 ± 9	33.7%	23 ± 16	4.6%
Acetone	265 ± 15	3 ± 1	1.0%	13 ± 4	47.2%	82 ± 3	30.9%
DMSO	104 ± 19	7 ± 3	6.4%	56 ± 11	54.3%	72 ± 14	69.1%

A recent comparison of SSGR with other fat suppression technique for single shot RARE imaging of the abdomen at 7.0 T revealed that SSGR exhibits the best performance and hence should be the method of choice for fat suppressed applications of RARE variants [JOHST2014]. Due to these results and the outcome of the performed phantom imaging, the SSGR technique is applied for the purpose of fat suppression in the examinations presented in the following sections.

5.3 Suppression of blood signal

At lower magnetic field strengths the double inversion recovery preparation module is the established technique for dark blood RARE imaging [SIMONETTI1996]. It features a nonselective 180° inversion RF pulse for global inversion of M_z. The initial inversion pulse is immediately followed by an adiabatic slice-selective 180° inversion RF pulse which reverses the magnetization for the slice to be imaged into the original state. At $M_z = 0$ for blood signal the excitation of the imaging part takes place. A two R-R interval repetition time approach is needed for RARE imaging in conjunction with double inversion recovery preparation to minimize T_1 weighting and to maximize the signal. The inversion time depends on TR, the heart rate and on T_1 of blood which changes with magnetic field strength [LADD2007, ROONEY2007, MOSER2012]:

$$TI_{null} = -T_1 \ln\left(\frac{1 + e^{-TR/T_1}}{2}\right) \qquad [54]$$

Assuming $T_1 = 2600$ ms for blood at 7.0 T [ROONEY2007] and a heart rate of 60 bpm equation [53] provides $TI_{null} = 810$ ms. Obviously, the heart rate is not constant but varies to different extent in

various subjects. Consequently, TI_{null} is altered which bears the risk to diminish the blood suppression efficiency.

In addition to timing issues B_1^+ inhomogeneities and imperfect inversion render the double inversion recovery approach at 7.0 T challenging. Various inversion RF pulses have been proposed to enhance inversion quality [RODGERS2013, KELLMAN2014]. These studies showed that hyperbolic secant (HS) RF pulses [SILVER1984] show less complete inversion compared to flattened HS RF pulses (HSn) with a nonlinearity factor *n* which is preferably equal 8 (HS8) [TANNÚS1996]. The current commercial implementation of the double inversion recovery module uses HS RF pulses and showed poor blood suppression efficiency. In order not to delay progress no extra blood suppression module but the blood suppression inherent to the train of RF refocusing pulses used in RARE was applied in the performed pilot studies presented in the following sections.

5.4 Proof-of-principle in i*n-vivo* imaging studies

5.4.1 Feasibility study in healthy volunteers

For the *in-vivo* feasibility study five healthy volunteers (mean age: (28.2 ± 2.9) years, 2 females, 3 males, mean BMI: (22.1 ± 2.1) kg/m^2, mean heart rate: (66.6 ± 8.1) bpm) without any known history of disease were scanned. RARE imaging was performed using the following parameters: TR = 1 R-R interval, TE = 45 ms, ESP = 6.4 ms, 4 dummy echoes, ETL = 12, receiver bandwidth = 179 kHz, spatial resolution = (1.2 x 1.2 x 5.0) mm^3, matrix size = 256 x 256, SSGR fat suppression. Four-chamber views and midventricular short-axis views of the heart were acquired for each volunteer. For selected subjects, basal and apical short-axis views of the heart were also acquired. To transfer the SNR gain inherent to 7.0 T into enhanced spatial resolution experiments with a spatial resolution as good as (0.9 x 0.9 x 2.0) mm^3 were performed.

Figure 60 shows exemplary four-chamber and short-axis views of the heart derived from cardiac RARE imaging in conjunction with SSGR fat suppression. The four-chamber views (Figure 60a-c) demonstrate the signal homogeneity across the heart which enables the depiction of the left and the right ventricle from the apex to the atria. The septum, which is often in the focus of clinical interest, is very well delineated.

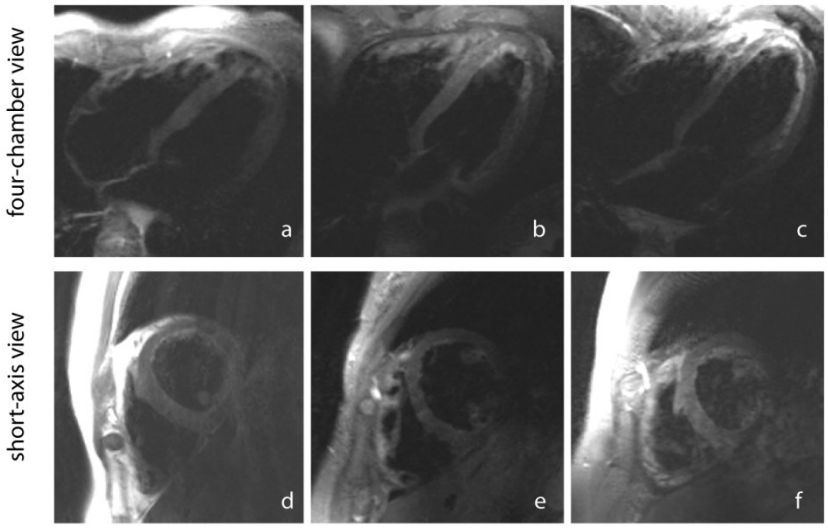

Figure 60: **7T cardiac RARE in healthy volunteers**
Four-chamber views **(a)-(c)** and short-axis views **(d)-(f)** of different volunteers included in the feasibility study acquired with the 16-channel bow tie antenna array. The images exhibit a spatial resolution of (1.2 x 1.2 x 5.0) mm^3. The example in (a),(d) was acquired at a very early stage of the project and was completed without the SSGR technique.

Notwithstanding this success, robust B_1^+ uniformity is still a challenge for cardiac RARE. An example with rather suboptimal B_1^+ homogeneity is presented in Figure 61. In particular the four-chamber view shows decreased signal coverage towards the atria which is also visible in the basal short-axis view. It is mainly the anterolateral segment of the myocardium – being most distant from the surface – which shows some signal reduction.

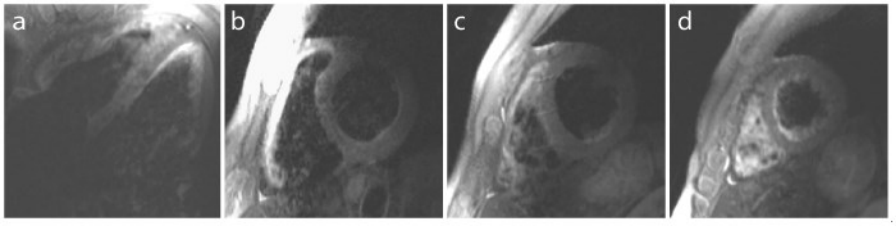

Figure 61: **7T cardiac RARE 4cv and short axis views in an exemplary healthy volunteer**
Four-chamber view **(a)**, basal **(b)**, midventricular **(c)** and apical **(d)** short axis views acquired in an exemplary volunteer to assess the image quality along the long axis of the heart. The spatial resolution of the images is (1.2 x 1.2 x 5.0) mm^3. The images were acquired using the 16-channel bow tie antenna array.

The quality of the fat suppression performed by using the SSGR technique is highly diverse. The images displayed in Figure 60a,d were acquired at a very early stage of this project when the SSGR technique was not yet included in the protocol. As a result, ghosts generated by the high signal in the chest wall superimpose the image. This effect disappeared with the addition of SSGR even though the fat signal is not very well suppressed in some cases (Figure 60f). The overall amount of fatty tissue and possibly the orientation within the FOV may affect the suppression quality.

The midventricular short-axis views (Figure 60d-f, Figure 61c) show little signal from slow flowing blood as it is expected for this location. Towards the apex, substantial blood signal remains as it is visible in the four-chamber views (Figure 60a-c, Figure 61a) and the apical short-axis view (Figure 61d). Bright blood signal is visible at the endocardial boarder of the left ventricle for all segments in the apical short-axis view and the right ventricle is basically totally filled with slow flowing blood which is not suppressed.

Despite these impediments, it is an appreciable achievement to tackle the obstacles like increased RF power deposition and RF non-uniformity for cardiac RARE imaging at 7.0 T and to generate sufficient signal homogeneity to perform four-chamber view black blood imaging of the heart with satisfying depiction of the myocardium.

The preliminary results helped to fine-tune the imaging including an enhanced spatial resolution. Figure 62 displays images with a spatial resolution that is by a factor of two improved versus the RARE images depicted in Figure 60 and Figure 61. In this particular case, the ample B_1^+ uniformity afforded the depiction of the entire myocardium, including the anterolateral segment from the apex to the atria.

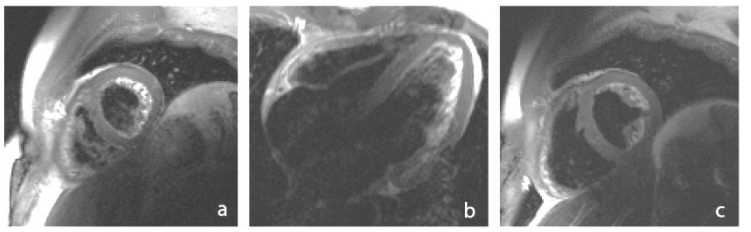

Figure 62: **High spatial resolution 7.0 T cardiac RARE images**
Four-chamber view **(a)**, midventricular **(b)** and apical **(c)** short axis views of a selected volunteer acquired using the 16-channel bow tie antenna array. The images exhibit a spatial resolution of (0.9 x 0.9 x 4.0) mm^3.

5.4.2 Pilot study in patients with hypertrophic cardiomyopathy

Cardiac RARE imaging at 7.0 T was applied in a pilot patient study including patients with hypertrophic cardiomyopathy (HCM) patients [HUELNHAGEN2015]. The imaging protocol included left ventricular function assessment and myocardial tissue characterization based on T_2^* mapping.

Due to the encouraging results obtained for healthy volunteers, RARE imaging of a four-chamber view was performed in each HCM patient to investigate its feasibility in a clinical scenario. For this purpose a 16-channel loop RF coil array was employed together with: TR = 1 R-R interval, TE = 45 ms, ESP = 6.4 ms, 4 dummy echoes, ETL = 12, receiver bandwidth = 179 kHz, spatial resolution = (1.2 x 1.2 x 5.0) mm^3, matrix size = 256 x 256, SSGR fat suppression. Preliminary

results are presented in Figure 63 for two HCM patients (first patient: 47 years, BMI = 24.6 kg/m^2, 64 bpm; second patient: 66 years, BMI = 23.0 kg/m^2, 64 bpm).

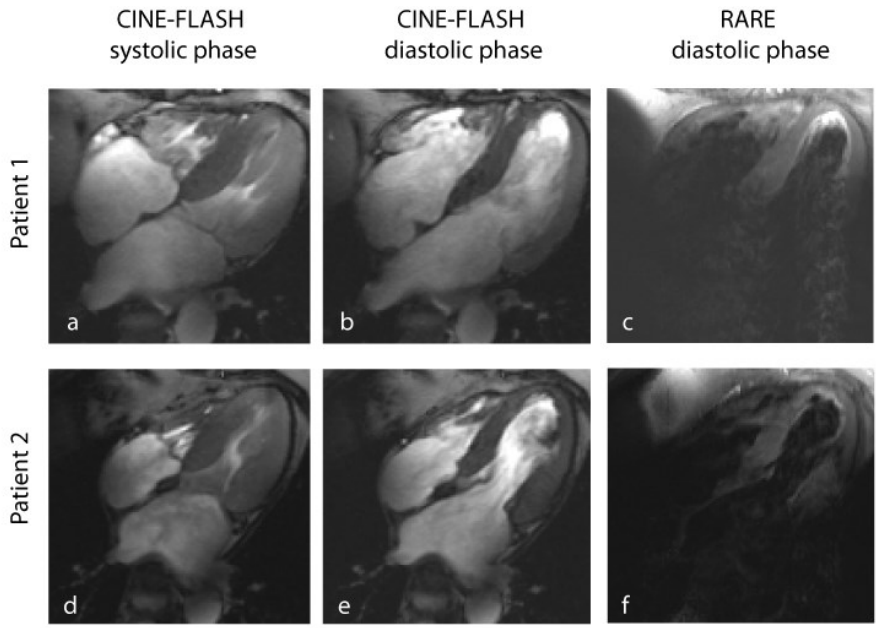

Figure 63: **Examples for 7T cardiac RARE imaging in HCM patients**
Four-chamber view FLASH images from a CINE acquisition are depicted for a systolic **(a,d)** and a diastolic **(b,e)** cardiac phase for two patients. The corresponding RARE images for the same slice are depicted in **(c)** and **(f)**. The RARE images exhibit a spatial resolution of (1.2 x 1.2 x 5.0) mm^3.

FLASH images acquired at systole (Figure 63a,d) demonstrate the myocardial thickening in the left ventricle of these patients, a clinical feature of HCM. The pathology is also recognizable in the diastolic phase (Figure 63b,e). The corresponding RARE images (Figure 63c,f) which were triggered to the late diastole underscore the challenges of cardiac RARE imaging at ultrahigh magnetic field strengths. One shortcoming is the reduced B_1^+ homogeneity which can be attributed to the use of a loop RF coil array instead of bow tie antennas used in the feasibility study in healthy volunteers. This results in a limited depiction of the heart starting from the midventriulcar short-axis. Since blood flow is parallel to the four-chamber view of the heart blood signal contributions remain in regions with slow blood flow, in particular in regions close to the apex. Motion artifacts present another challenge since the patients' capabilities to hold the breath are commonly inferior to healthy subjects. Notwithstanding these challenge the clear delineation of the myocardium from the blood pool (especially for patient 1) and the depiction of the right ventricle in the area with sufficient B_1^+ homogeneity can be appreciated.

5.5 Tissue characterization with quantitative mapping of the effective relaxation time T_2^*

Emerging CMR applications include T_2^* mapping which is increasingly used for non-invasive myocardial tissue characterization [HEZEL2012]. The linear relationship between magnetic field strength and microscopic susceptibility renders it conceptually appealing to pursue myocardial T_2^* mapping at ultrahigh magnetic fields [MELONI2014]. The relatively strong T_2^* weighting required to make GRE based techniques sensitive to changes in magnetic susceptibility asks for long evolution times (TE) between RF excitation and data acquisition. This approach prolongs scan times and increases the propensity for susceptibility artifacts and signal void which is pronounced at UHF. RARE imaging is largely immune to B_0 inhomogeneities and provides images free of distortions due to the use of RF refocused echoes. The applicability of cardiac RARE at 7.0 T has been demonstrated in the previous chapter. This finding, together with the challenges and opportunities of myocardial T_2^* mapping were the driving forces to investigate the feasibility of RARE based T_2^* mapping of the heart at 7.0 T using the 8-channel bow tie antenna array.

T_2^* weighting in RARE is accomplished by inserting an evolution time τ after the excitation RF pulse whereby an additional phase is accrued reflecting the T_2^* effect [NORRIS1992]. This approach runs the benefit that T_2^* can be adjusted from zero upwards to maximize functional or tissue contrast [HEINRICHS2009]. To avoid destructive interferences between odd and even echo groups a split-echo RARE variant was employed [SCHICK1997]. Two images were reconstructed separately and added afterwards to restore the full available signal intensity. Fat suppression was performed using the SSGR technique. After offline-reconstruction the images were co-registered and fitted to a mono-exponential decay.

Myocardial T_2^* mapping using split-echo RARE was performed for a midventricular short-axis view after volume selective B_0 shimming. The following parameters were employed: TR = 1 R-R interval, TE = 45 ms, ESP = 6.5 ms, spatial resolution = (1.2 x 1.2 x 5.0) mm^3, nominal flip angle = 180°, τ = 0-14 ms, phase encoding H-F). For comparison, multi-echo gradient echo (ME-GRE) was completed (TR = 13 ms, 8 equidistant echoes with TE = 2.04-10.20 ms, spatial resolution = (1.2 x 1.2 x 5.0) mm^3, nominal flip angle = 10°, phase encoding A-P). Data acquisition was triggered to mid-diastole using the acoustic approach.

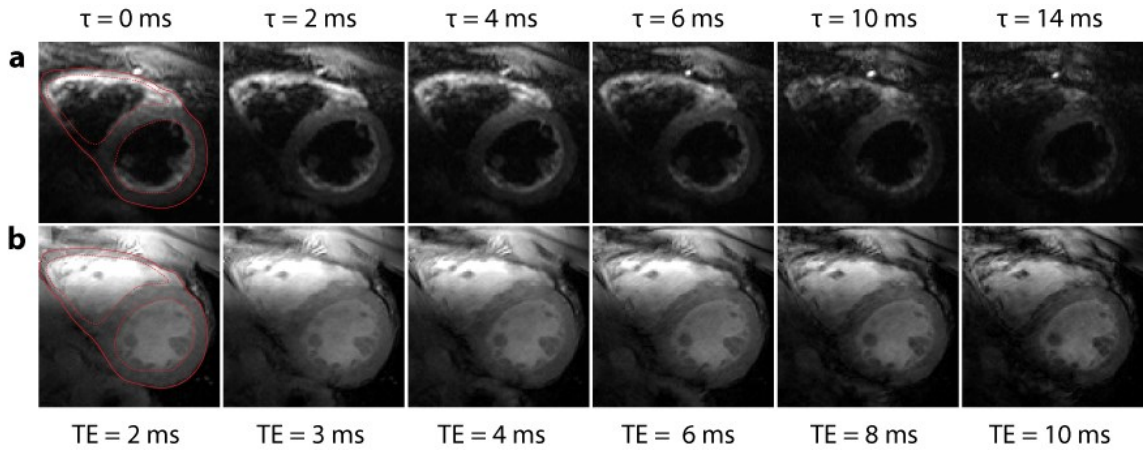

Figure 64: **T_2^* mapping of the heart at 7.0 T**
(a): T_2^*-weighted split-echo RARE images employing evolution times ranging from τ = 0 ms to τ = 14 ms. **(b):** ME-GRE with TE ranging from 2 ms to 10 ms. For improved visualization, the images do not exhibit identical windowing over the range of increasing susceptibility weighing.

Figure 64a shows a series of T_2^*-weighted images derived from RARE using evolution times τ ranging from 0 ms to 14 ms. The geometric integrity of the RARE images is maintained over the range of T_2^* weighting. Subcutaneous fat is mostly suppressed in the RARE images while fat surrounding the myocardium remained present in some areas despite the SSGR fat suppression. Myocardial T_2^* mapping was feasible for the RARE based technique as demonstrated in Figure 65a. In comparison, ME-GRE imaging exhibited less myocardium to blood contrast since signal contributions from the blood pool were not suppressed. A myocardium/blood contrast ratio of 0.8 was observed for the GRE image with TE = 2 ms while a ratio of 16.3 was determined for the RARE image with τ = 0 ms. As a consequence, the delineation of the myocardium in the corresponding T_2^* map (Figure 65b) is more challenging compared to the RARE based T_2^* map. Despite using volume selective shimming susceptibility artifacts occurred in the inferolateral segment of the heart when using ME-GRE with echo times larger than 6 ms (Figure 64b). This translates itself in an underestimation of T_2^* relaxation times in the myocardial segment 10 (inferior) and 11 (inferolateral) according to the standardized myocardial segmentation and nomenclature for tomographic imaging of the heart [CERQUEIRA2002]. The T_2^* map derived from RARE imaging shows an averaged effective transversal relaxation time which accords well with previously reported results [HEZEL2012]. For the septum an averaged T_2^* of (16 ± 6) ms was observed for the RARE based approach. In comparison, an averaged T_2^* of (15 ± 6) ms for the septum was derived from ME-GRE acquisitions.

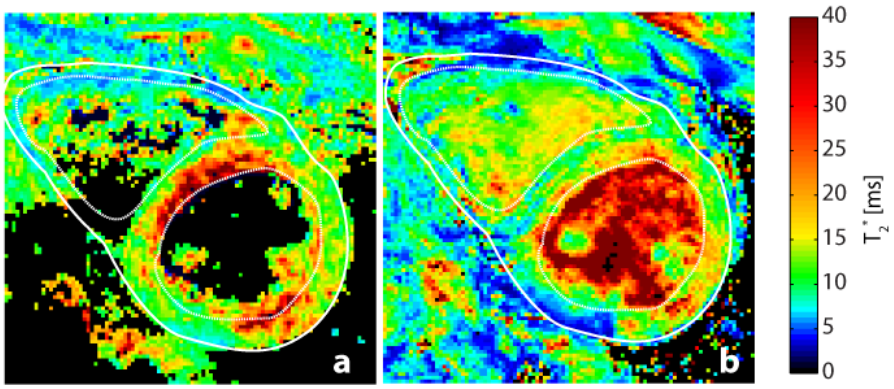

Figure 65: **Myocardial T_2^* maps of the heart acquired at 7.0 T**
T_2^* maps of a short-axis view derived from data shown in Figure 64 are depicted for the RARE approach **(a)** and the GRE approach **(b)**. The contour defined in the images shown in Figure 64 were copied to the T_2^* maps for better delineation of the myocardium.

These preliminary results demonstrate that the RF power deposition and RF non-uniformity constraints of RARE imaging can be offset at 7.0 T to enable myocardial T_2^* mapping using split-echo RARE. This approach holds the potential to provide a valuable alternative for T_2^* mapping free of image distortion versus gradient echo imaging approaches. Myocardial T_2^* within the septum derived from RARE imaging matches T_2^* obtained from gradient echo imaging. Differences in T_2^* between endocardial and epicardial layers of the myocardium found in a previous study using gradient echo based techniques [HEZEL2012] were confirmed by RARE based T_2^* mapping. Further investigations are necessary to prove if these findings result from anatomical structures or if they are caused by susceptibility gradients at the blood/myocardium interface.

5.6 Summary and Discussion

The work outlined in this chapter demonstrates for the first time that cardiac RARE imaging at 7.0 T is feasible. Imaging in healthy subjects and preliminary patient data have been presented, followed by explorations into RARE based T_2^* mapping of the heart. The feasibility study in healthy volunteers was performed using an eight-channel bow tie cardiac array. In comparison, the patient data were acquired using a 16-channel loop array. A closer examination of the experimental data shows that dipole antennas provide better B_1^+ efficiency versus loop elements which is in alignment with previous numerical simulations [RAAIJMAKERS2011, IPEK2012].

The current implementation of the applied RARE sequence features Hanning-windowed SINC RF pulses which provide a rather poor ratio between nominal and actual flip angle which is pronounced at higher magnetic field strengths. Adiabatic RARE imaging has been suggested for ultrahigh magnetic field applications in the rat brain [DE GRAAF2003]. Recently, a study applying adiabatic RARE imaging for human brain, neck and pelvis imaging at 7.0 T was published [VAN

KALLEVEEN2012]. A non-selective adiabatic half passage (AHP) RF pulse with a duration of 2 ms was applied for excitation. Two slice selective adiabatic full passage (AFP) RF pulses, which provide a distinct frequency profile, were used to generate the first echo. The duration of each of the two RF pulses is 10 ms. The remaining echoes along the echo train were generated by BIR4 RF pulses (B_1-insensitive rotation, 4 composites [STAEWEN1990, GARWOOD1991, TANNÚS1997]), each of them 6 ms long. With these RF pulse designs the minimal ESP is 15 ms and the first echo is generated 30 ms after the excitation RF pulse. These long RF pulse durations and the prolonged ESP render this approach inappropriate for human cardiac RARE imaging at 7.0 T. On the one hand, the long resulting TE would decrease the available signal intensity. On the other hand, data acquisition is restricted to the cardiac rest period in diastole which has a heart rate dependent duration of approximately 100 ms to 200 ms. Consequently, the number of echoes that can be acquired after one excitation is very much restricted. With this limitation the number of excitations grows rapidly. For example, the acquisition of a 256 x 256 matrix recommended by the guidelines for standardized MR protocols would require 23 heart beats if a 1 R-R interval repetition time is used [KRAMER2008, KRAMER2013]. This poses a challenge since the overall sequence duration should not exceed 15 s which defines a clinically acceptable breath hold period. Let alone that the adiabatic RF pulses, especially the BIR4 RF pulses, are SAR consuming which reinforces the timing constraints. Slice accelerated acquisition schemes using power independent number of slices (PINS) RF pulses which perform spatially periodic excitation and refocusing provide means for relaxing power deposition [NORRIS2011]. These pulses with durations shorter than 6 ms have been successfully incorporated into RARE for brain imaging [NORRIS2014] and showed largely reduced SAR values with the attendant advantage of multislice imaging.

State-of-the-art UHF-MR systems support multi-channel transmit arrays that can be driven in two modes: (i) using an array of independent feeding RF power amplifiers (RFPA) with control of phase, amplitude or even complete RF waveforms for all individual channels or (ii) using a single feeding RFPA. For the latter regime the amplifier output is commonly split into fixed-intensity signals using RF power splitters. Phase adjustments for individual coil elements or groups of coil elements are accomplished with phase-shifting networks or coaxial cables like in the case of the cardiac arrays applied in this thesis. Multi feeding RFPA implementations support software driven control over phase and amplitude by modulating the applied input signal. Moreover it enables sophisticated parallel transmission (pTX) of independent RF waveforms to every channel, holding the potential to improve the excitation/refocusing homogeneity and to reduce the overall RF energy [KATSCHER2003, ZHU2004a, ULLMANN2005, KATSCHER2006]. Slice selective spoke RF pulses [SAEKHO2006] consist of several short sinc RF subpulses which are accompanied by gradient pulses

in k_z direction to obtain slice selection as well as in k_x and k_y direction to achieve in-slice modulation with the goal to improve B_1^+ homogeneity. These RF waveforms are based on the small-tip-angle (STA) approximation [PAULY1989] and are prone to fail for larger flip angles which are required for RARE imaging. A spoke design which overcomes the STA estimation and which reduces severe B_1^+ inhomogeneities was introduced for 90° and 180° slice-selective excitations [XU2007, SETSOMPOP2008b]. A further challenge is to transfer the concept of pTX using spoke RF pulses which was initially presented for brain imaging [SETSOMPOP2008a, WU2010, CLOOS2012] to cardiac imaging. In cardiac MR cardiac and physiological motion dictate the viable window for data acquisition which needs to be balanced with the competing spatial resolution constraints. A study by [SCHMITTER2013] successfully demonstrated the feasibility of cardiac CINE gradient echo imaging at 7.0 T using spoke RF pulses consisting of two RF subpulses. With this approach it was shown that spoke pulses support improvements in the excitation field homogeneity or a reduction in the RF pulse energy. With RF pulse durations of approximately 5 ms for the high-flip angle spoke RF pulses and the strategies presented to transfer the spoke concept to cardiac imaging, it would be conceptually appealing to implement the spoke approach for cardiac RARE imaging at 7.0 T.

Fat suppression was performed using the SSGR technique. Since this approach does not use any additional RF pulses, its application at 7.0 T is favorable versus fat suppression techniques commonly used at lower magnetic field strengths. Increasing the magnetic field strength improves the performance of SSGR so that this approach will be used for further explorations into RARE based black blood imaging of the heart at 7.0 T.

Blood suppression remains a challenge that warrants further development. The current implementation of the DIR module employs HS RF pulses providing limited inversion efficiency. Here substitution of the HS RF pulses by HS8 pulses holds the promise to improve inversion efficiency [RODGERS2013, KELLMAN2014]. Another option to suppress signal from blood is to incorporate modest diffusion weighting into the RARE sequence. The results presented in this chapter were obtained without the use of an additional blood suppression module. Major parts of the blood pool are suppressed by the in-flow of non-excited spins during excitation and refocusing. Remaining signal from slow flowing blood can potentially compromise the diagnostic assessment so that explorations into reliable blood suppression techniques at UHF are of high importance.

Prospective navigator gating and tracking using 2D selective beam excitation holds the potential to further increase image quality [EHMAN1989, VAN ELDEREN2009], especially in patients who may not be able to hold their breath sufficiently long. Respiratory motion control relaxes scan time

constraints and enables higher spatial resolutions. For CMR at 7.0 T the heart/lung interface rather than the diaphragm is used for navigator localization which requires a shortening of the navigator RF pulse to reduce susceptibility artifacts at the heart/lung interface [WANG1995, VAN ELDEREN2009].

In conclusion, the sophisticated RF coil technology forwarded by our group provided uniform signal across the entire heart and helped to afford cardiac RARE imaging at 7.0 T. Signal losses due to low actual flip angles are offset by the high inherent signal intensity of RARE sequences. Equipped with this hardware the preliminary results showed that cardiac RARE imaging at ultrahigh magnetic field strength is feasible but requires further research. The merits and limitations of the current implementations have been carefully considered. Solutions and alternative approaches for enhancing transmission field uniformity, fat suppression and blood signal suppression have been discussed.

Conclusions and Future Directions

This thesis demonstrates the feasibility and applicability of novel Rapid Acquisition with Relaxation Enhancement variants which were developed to advance existing imaging techniques with a focus on enhancing anatomical integrity, relaxing acquisition time constraints and offsetting artifact level. RARE imaging facilitates fast acquisitions which are of pivotal importance in clinical routine where economic constraints ask for ever shorter scanning times. Moreover, durations of single acquisitions are limited for reasons of patient comfort and the purpose of avoiding image artifacts. RARE – presenting itself as an excellent imaging technique for fast imaging with high signal intensity and insensitivity to static magnetic field inhomogeneities – was chosen as a starting point for the explorations undertaken in this thesis.

To facilitate the development of novel RARE methodology the signal generation within RARE was carefully investigated and examined. For this purpose the focus was set on the physical principles and approaches which form the foundation for the development of novel RARE variants.

The proposed simultaneous dual contrast weighting methodology using double echo RARE imaging (2in1-RARE) [FUCHS2014b] separates spin echoes and stimulated echoes within the echo train and thereby enables individual contrast manipulation of both magnetization components. The current implementation generates a PD-weighted anatomical and a T_2^*-weighted functional image within one acquisition. 2in1-RARE was carefully examined in phantom imaging including point spread function assessment. The newly developed RARE variant was benchmarked versus split-echo RARE acquisitions. T_2^* mapping was performed in comparison to standard multi-echo gradient echo imaging to validate the T_2^* weighting within 2in1-RARE. A feasibility study in healthy volunteers demonstrated its applicability for *in-vivo* brain imaging. The investigation of an MS patient using 2in1-RARE underlined the ability to depict small and subtle pathological structures in the brain. Dual-contrast pulse sequences [HIGUCHI1991, FRANCONI1994, SONG2004, ONG2005] are of high interest because of their speed advantage over sequential acquisitions and the eliminated risk of mis-registrations when acquiring more than one contrast. A dual-contrast RARE variant exploiting the strict separation of spin echoes and stimulated echoes presented in the scope of this thesis is the first of its type and hence was filed for patent application. 2in1-RARE offers further possibilities for contrast generation; the spin echo part can be sensitized to flow or diffusion.

The latter option would offer the possibility to combine 2in1-RARE with the adopted multi-shot split-echo diffusion-weighted RARE variant (ms-RARE) [WILLIAMS1999]. Distortion free diffusion-weighted images of the orbit have been presented in this thesis using the ms-RARE variant [PAUL2015]. As a precursor to the *in-vivo* situation, the proposed RARE based approach was validated in phantom experiments versus ss-EPI which is the clinical standard for DWI [WARACH1995] and versus ss-RARE which was recently suggested as an alternative for orbital DWI [DE GRAAF2012b]. This comparison revealed that SNR provided by ms-RARE is competitive with ss-EPI and ss-RARE. Apparent diffusion coefficients derived from ms-RARE accord very well with ADCs obtained with ss-EPI and ss-RARE approaches, which demonstrates the integrity of ms-RARE for DWI. The propensity of ms-RARE to geometric distortions was assessed qualitatively and quantitatively in a structure phantom using two EPI variants as a reference. The geometric fidelity obtained for ms-RARE was found to be superior to the clinical standard (ss-EPI) as well as superior to an improved EPI variant (rs-EPI). Severe geometric distortions were observed for ss-EPI.

These findings underline the need for alternative imaging techniques to circumvent the observed degradation in image quality when using readily available imaging techniques. Especially, the geometric distortions intrinsic to ss-EPI are amplified when moving to higher magnetic field strengths. Imaging of the eye – as a small and subtle organ – requires a sub-millimeter resolution combined with a small field-of-view [PATZ2007] which is at the SNR limit at magnetic field strengths commonly used in clinical practice. This constraint can be addressed by moving to high and ultrahigh magnetic field strengths ($B_0 \geq 3.0$ T). The gain in signal-to-noise ratio inherent to high magnetic field strengths can be translated into spatial resolution enhancements. Consequently high spatial resolution *in-vivo* imaging of the human eye is enabled [MAFEE2005, RICHDALE2009]. With the achievements of this thesis project, diffusion-weighted ms-RARE in conjunction with dedicated RF coil technology [GRAESSL2014a] enabled distortion free diffusion-weighted imaging of the eye and orbit at 3.0 T and at 7.0 T with an in-plane spatial resolution as good as (0.2 x 0.2 x 2.0) mm^3.

An *in-vivo* comparison of ms-RARE, ss-EPI and rs-EPI underscored the geometric distortion constraints for the EPI variants at 3.0 T and 7.0 T. These results render diffusion-weighted EPI variants unsuitable for DWI of the eye and orbit at 3.0 T and 7.0 T. The development of RARE based DWI approaches was taken to the next level by demonstrating its feasibility in a pilot patient study as a precursor to broader clinical studies. This pilot study demonstrated the capability of diffusion-weighted ms-RARE to differentiate between retinal detachment and ocular masses. The geometric integrity of diffusion-weighted ms-RARE affords a convenient co-registration with high spatial resolution anatomical reference images with the ultimate goal to provide guidance in

therapy planning and evaluation. High spatial resolution *ex-vivo* images and histology of the enucleated eye confirmed the results obtained with *in-vivo* DWI. Further to ocular imaging, diffusion-sensitized ms-RARE holds the promise for targeting and imaging deeper lying sections of the orbit, the optical canal and optic nerve. DWI of the optic nerve bears clinical relevance for optic neuropathies in neuroinflammatory diseases and also for the differential diagnosis of debilitating autoimmune or orphan diseases of the central nervous system that run the risk of visual impairment [SINNECKER2012, WUERFEL2012].

DWI and sophisticated diffusion tensor imaging have been applied to assess myocardial microstructure *in-vivo* [REESE1995, WU2006, NIELLES-VALLESPIN2013]. However, DWI of the beating heart is challenging and prone to misinterpretation of the acquired data due to the discrepancy between the diffusion on a micrometre scale and the bulk cardiac motion taking place on a millimetre scale. T_2^*-weighted imaging using gradient echo imaging techniques has been suggested as an alternative [KOEHLER2003] since it is less sensitive to motion induced corruption of data. Ultrahigh magnetic field strengths are beneficial for the pursuit of T_2^*-weighted imaging due to the linear relationship between microscopic susceptibility and the magnetic field strength [MELONI2014]. On the downside, increased macroscopic magnetic field inhomogeneities render gradient echo imaging using long echo times unsuitable for susceptibility weighting challenging at ultrahigh magnetic field strengths. To overcome these shortcomings, this thesis investigated the feasibility of a T_2^*-weighted RARE variant with the ultimate goal to provide means for characterization of *in-vivo* myocardial microstructure at 7.0 T.

A first requirement for successful RARE imaging at 7.0 T is uniform signal across the heart which was achieved by using a cardiac bow tie antenna RF coil array [GRAESSL2013, WINTER2013]. This design holds the benefit that the Poynting vector is aligned vertically to the surface and hence it is beneficial for imaging deep lying organs like the heart [RAAIJMAKERS2011]. That finding is part of widespread explorations into enabling RF coil technology with the goal to overcome non-uniformities of the transmission fields in the thorax and abdomen which offset the benefits of UHF imaging. Rigid, flexible and modular multi-channel RF coil design configurations evolved with a trend towards a larger number of transmit and receive elements based on the motivation to improve anatomic coverage and transmission field shaping. Reports concentrate on strip line elements [SNYDER2009, VAUGHAN2009], dielectric resonant antennas [AUSSENHOFER2014], loop elements [WINTER2012, GRAESSL2014b] and electrical dipoles [IPEK2012, WINTER2013]. The latter provide a linear polarized current pattern, where RF energy is directed perpendicular to the dipole along the Poynting vector to the subject. As a consequence, the excitation field presents itself symmetrical and rather uniform with increased depth penetration [RAAIJMAKERS2011]. These

properties led to the decision to use a cardiac bow tie antenna RF coil array for the explorations into cardiac RARE imaging at 7.0 T within the scope of this thesis.

A pilot study in healthy volunteers demonstrated that anatomical cardiac RARE imaging at 7.0 T is feasible. Few limitations were revealed which need to be assessed in future studies. Fat suppression using the slice selection gradient reversal technique yielded a satisfying fat suppression efficiency of up to 92%. Elimination of signal from slow flowing blood remains a concern so that it is essential to drive explorations into novel blood suppression methodology including novel inversion RF pulse designs. The preliminary patient data are heartening but underline the need for further research into enhanced transmission field uniformity and blood suppression, while managing the RF power deposition constraints.

RARE based T_2^* mapping was accomplished and benchmarked against gradient echo imaging. The observed transmural change of T_2^* from epicardium to endocardium [HEZEL2012] creates a starting point for further investigations of myocardial microstructure. Up to date, late gadolinium enhancement is a proven clinical tool for the assessment of ischemic heart diseases and also for non-ischemic myocardial diseases such as hypertrophic cardiomyopathy. The findings obtained from myocardial T_2^* mapping performed in this thesis can be interpreted as an indicator to use susceptibility weighting as an endogenous contrast agent. If this holds true, the need for exogenous contrast agents could perhaps become obsolete in the long run. This development would help to address the spatial and temporal resolution constraints of today's late gadolinium enhancement techniques, let alone the replacement of contrast enhanced by non-contrast enhanced imaging technique. The latter has major cost and patient safety/comfort implications

Susceptibility weighted imaging (SWI) processing combines the information of T_2^*-weighted magnitude images and the corresponding high-pass-filtered phase images [HAACKE2004]. The information comprised within the phase images increases the contrast between tissues with differing susceptibilities. SWI has been applied to investigate tissue microstructure and track fibers in the brain [DEISTUNG2008, LIU2012]. Recently, SWI has been suggested to investigate myocardial microstructure *ex-vivo* [HUELNHAGEN2014b] as well as *in-vivo* in the human heart at 7.0 T [HUELNHAGEN2014a]. Since susceptibility effects change with the tilt angle between myocardial fibers and the external field [ZIENER2012], SWI constitutes a promising tool for investigations of myocardial fiber structure. Going one step further, quantitative susceptibility mapping (QSM) [LI2004] holds the promise to provide local information about microscopic susceptibility. Those explorations apply gradient echo imaging techniques for the generation of T_2^*-weighted images, accompanied by the constraints discussed in this thesis. RARE based T_2^*-weighted imaging holds

the potential to overcome those hindrances with the ultimate goal to disestablish *ex-vivo* histology and to provide reliable *in-vivo* information for the assessment of myocardial microstructure.

To summarize, within the scope of this PhD thesis new Rapid Acquisition with Relaxation Enhancement variants were developed. Implementation and validation of these techniques were realized to advance the capabilities of MRI with simultaneous contrast, of diffusion-weighted MRI of the eye and orbit free of geometric distortion and of high spatial resolution black blood imaging of the heart including myocardial T_2^* mapping. The underlying physical and the methodological characteristics of the developed imaging techniques were carefully assessed in phantom imaging as well as *in-vivo* imaging. Bridging the gap between development and practice as well as between research and clinical routine was a major goal of this thesis. To realize this challenge, the clinical applicability of the proposed approaches was demonstrated in healthy subjects as well as in multiple sclerosis patients, in patients with ocular masses and in patients with hypertrophic cardiomyopathy. The merits and limitations of the proposed approaches were carefully discussed including a look beyond the horizon.

References

ABDEL-ATY (2009). Myocardial Edema Imaging of the Area at Risk in Acute Myocardial Infarction; Seeing Through Water. *JACC: Cardiovascular Imaging* **2**(7):832-834.

ABDEL-ATY and SCHULZ-MENGER (2007a). Cardiovascular Magnetic Resonance T2-weighted Imaging of Myocardial Edema in Acute Myocardial Infarction. *Recent Patents on Cardiovascular Drug Discovery* **2**(1):63-68.

ABDEL-ATY, SIMONETTI and FRIEDRICH (2007b). T2-weighted cardiovascular magnetic resonance imaging. *J Magn Reson Imaging* **26**(3):452-459.

ABDEL-ATY, ZAGROSEK, SCHULZ-MENGER, TAYLOR, MESSROGHLI, KUMAR, GROSS, DIETZ and FRIEDRICH (2004). Delayed enhancement and T_2-weighted cardiovascular magnetic resonance imaging differentiate acute from chronic myocardial infarction. *Circulation* **109**(20):2411-2416.

ALSOP (1997). Phase insensitive preparation of single-shot RARE: application to diffusion imaging in humans. *Magn Reson Med* **38**(4):527-533.

ANDERSON and GORE (1994). Analysis and correction of motion artifacts in diffusion weighted imaging. *Magn Reson Med* **32**(3):379-387.

APUSHKIN, APUSHKIN, SHAPIRO and MAFEE (2005). Retinoblastoma and Simulating Lesions: Role of Imaging. *Neuroimag Clin N Am* **15**(1):49-67.

ATKINSON, PORTER, HILL, CALAMANTE and CONNELLY (2000). Sampling and reconstruction effects due to motion in diffusion-weighted interleaved echo planar imaging. *Magn Reson Med* **44**(1):101-109.

AUSSENHOFER and WEBB (2014). An eight-channel transmit/receive array of TE_{01} mode high permittivity ceramic resonators for human imaging at 7T. *J Magn Reson* **243**(0):122-129.

BALCHANDANI, KHALIGHI, GLOVER, PAULY and SPIELMAN (2012). Self-refocused adiabatic pulse for spin echo imaging at 7 T. *Magn Reson Med* **67**(4):1077-1085.

BARKER and MARECI (1989). Suppression of artifacts in multiple-echo magnetic resonance. *J Magn Reson* **83**(1):11-28.

BASSER, MATTIELLO and LEBIHAN (1994a). Estimation of the Effective Self-Diffusion Tensor from the NMR Spin Echo. *J Magn Reson,Ser B* **103**(3):247-254.

BASSER, MATTIELLO and LEBIHAN (1994b). MR diffusion tensor spectroscopy and imaging. *Biophys J* **66**(1):259-267.

BECKER, FRAUENRATH, HEZEL, KROMBACH, KREMER, KOPPERS, BUTENWEG, GOEMMEL, UTTING, SCHULZ-MENGER and NIENDORF (2010). Comparison of left ventricular function assessment using phonocardiogram- and electrocardiogram-triggered 2D SSFP CINE MR imaging at 1.5 T and 3.0 T. *Eur Radiol* **20**(6):1344-1355.

BEENAKKER, VAN RIJN, LUYTEN and WEBB (2013). High-resolution MRI of uveal melanoma using a microcoil phased array at 7 T. *NMR Biomed* **26**(12):1864-1869.

BERKOWITZ, MCDONALD, ITO, TOFTS, LATIF and GROSS (2001). Measuring the human retinal oxygenation response to a hyperoxic challenge using MRI: Eliminating blinking artifacts and demonstrating proof of concept. *Magn Reson Med* **46**(2):412-416.

BERNSTEIN, KING and ZHOU (2004). *Handbook of MRI Pulse Sequences*. Elsevier Academic Press.

BERT, PATZ, OSSIANI, CARUTHERS, JARA, KREJZA and FREDDO (2006). High-Resolution MR Imaging of the Human Eye 2005. *Acad Radiol* **13**(3):368-378.

BIZINO, BONETTI, VAN DER GEEST, VERSLUIS, WEBB and LAMB (2014). High Spatial Resolution Coronary Magnetic Resonance Angiography at 7 T: Comparison With Low Spatial Resolution Bright Blood Imaging. *Invest Radiol* **49**(5):326-330.

BLOCH (1946a). Nuclear Induction. *Phys Rev* **70**(7-8):460-474.

BLOCH, HANSEN and PACKARD (1946b). The Nuclear Induction Experiment. *Phys Rev* **70**(7-8):474-485.

BLOCK, PAULY and NISHIMURA (1997). RARE spiral T_2-weighted imaging. *Magn Reson Med* **37**(4):582-590.

BOLACCHI, GARACI, MARTUCCI, MESCHINI, FORNARI, MARZIALI, MANCINO, SQUILLACI, FLORIS, CERULLI, SIMONETTI and NUCCI (2012). Differences between Proximal versus Distal Intraorbital Optic Nerve Diffusion Tensor Magnetic Resonance Imaging Properties in Glaucoma Patients. *Invest Ophthalmol Vis Sci* **53**(7):4191-4196.

BÖRNERT and JENSEN (1994). Single-shot-double-echo EPI. *Magn Reson Imaging* **12**(7):1033-1038.

BOUVY, BIESSELS, KUIJF, KAPPELLE, LUIJTEN and ZWANENBURG (2014). Visualization of Perivascular Spaces and Perforating Arteries With 7 T Magnetic Resonance Imaging. *Invest Radiol* **49**(5):307-313.

BRITTAIN, HU, WRIGHT, MEYER, MACOVSKI and NISHIMURA (1995). Coronary Angiography with Magnetization-Prepared T_2 Contrast. *Magn Reson Med* **33**(5):689-696.

BUEHRER, CURCIC, BOESIGER and KOZERKE (2008). Prospective self-gating for simultaneous compensation of cardiac and respiratory motion. *Magn Reson Med* **60**(3):683-690.

BUIKMAN, HELZEL and RÖSCHMANN (1988). The RF coil as a sensitive motion detector for magnetic resonance imaging. *Magn Reson Imaging* **6**(3):281-289.

BUTTS, DE CRESPIGNY, PAULY and MOSELEY (1996). Diffusion-weighted interleaved echo-planar imaging with a pair of orthogonal navigator echoes. *Magn Reson Med* **35**(5):763-770.

CALLAGHAN (1993). *Principles of Nuclear Magnetic Resonance Microscopy*. Oxford Science Publications.

CARMICHAEL, THOMAS and ORDIDGE (2009). Reducing ghosting due to k-space discontinuities in fast spin echo (FSE) imaging by a new combination of k-space ordering and parallel imaging. *J Magn Reson* **200**(1):119-125.

CARR and PURCELL (1954). Effects of Diffusion on Free Precession in Nuclear Magnetic Resonance Experiments. *Phys Rev* **94**(3):630-638.

CERQUEIRA, WEISSMAN, DILSIZIAN, JACOBS, KAUL, LASKEY, PENNELL, RUMBERGER, RYAN and VERANI (2002). Standardized Myocardial Segmentation and Nomenclature for Tomographic Imaging of the Heart: A Statement for Healthcare Professionals From the Cardiac Imaging Committee of

the Council on Clinical Cardiology of the American Heart Association. *Circulation* **105**(4):539-542.

CHEN, MUKHERJEE, DILLON and WINTERMARK (2006). Restricted Diffusion in Bilateral Optic Nerves and Retinas as an Indicator of Venous Ischemia Caused by Cavernous Sinus Thrombophlebitis. *Am J Neuroradiol* **27**(9):1815-1816.

CHIA, FISCHER, WICKLINE and LORENZ (2000). Performance of QRS detection for cardiac magnetic resonance imaging with a novel vectorcardiographic triggering method. *J Magn Reson Imaging* **12**(5):678-688.

CLARK, ROSENBAUM and DEMER (1999). Magnetic resonance imaging after surgical transposition defines the anteroposterior location of the rectus muscle pulleys. *J Pediatr Ophtalmol Strabismus* **3**(1):9-14.

CLOOS, BOULANT, LUONG, FERRAND, GIACOMINI, LE BIHAN and AMADON (2012). kT -points: short three-dimensional tailored RF pulses for flip-angle homogenization over an extended volume. *Magn Reson Med* **67**(1):72-80.

CONSTABLE, ANDERSON, ZHONG and GORE (1992a). Factors influencing contrast in fast spin-echo MR imaging. *Magn Reson Imaging* **10**(4):497-511.

CONSTABLE and GORE (1992b). The Loss of Small Objects in Variable TE Imaging: Implications for FSE, RARE, and EPI. *Magn Reson Med* **28**(1):9-24.

CONSTANTINIDES, ATALAR and MCVEIGH (1997). Signal-to-noise measurements in magnitude images from NMR phased arrays. *Magn Reson Med* **38**(5):852-857.

CROWE, LARSON, ZHANG, CARR, WHITE, LI and SIMONETTI (2004). Automated rectilinear self-gated cardiac cine imaging. *Magn Reson Med* **52**(4):782-788.

DE CRESPIGNY, MARKS, ENZMANN and MOSELEY (1995). Navigated Diffusion Imaging of Normal and Ischemic Human Brain. *Magn Reson Med* **33**(5):720-728.

DE GRAAF, BARKHOF, MOLL, IMHOF, KNOL, VAN DER VALK and CASTELIJNS (2005). Retinoblastoma: MR Imaging Parameters in Detection of Tumor Extent. *Radiology* **235**(1):197-207.

DE GRAAF, GÖRICKE, RODJAN, GALLUZZI, MAEDER, CASTELIJNS and BRISSE (2012a). Guidelines for imaging retinoblastoma: imaging principles and MRI standardization. *Pediatr Radiol* **42**(1):2-14.

DE GRAAF, POUWELS, RODJAN, MOLL, IMHOF, KNOL, SANCHEZ, VAN DER VALK and CASTELIJNS (2012b). Single-Shot Turbo Spin-Echo Diffusion-Weighted Imaging for Retinoblastoma: Initial Experience. *Am J Neuroradiol* **33**(1):110-118.

DE GRAAF, ROTHMAN and BEHAR (2003). Adiabatic RARE imaging. *NMR Biomed* **16**(1):29-35.

DEISTUNG, RAUSCHER, SEDLACIK, STADLER, WITOSZYNSKYJ and REICHENBACH (2008). Susceptibility weighted imaging at ultra high magnetic field strengths: Theoretical considerations and experimental results. *Magn Reson Med* **60**(5):1155-1168.

DEONI, PETERS and RUTT (2004). Quantitative diffusion imaging with steady-state free precession. *Magn Reson Med* **51**(2):428-433.

DEUX, MAATOUK, VIGNAUD, LUCIANI, LENCZNER, MAYER, LIM, DUBOIS-RANDE, KOBEITER and RAHMOUNI (2011). Diffusion-weighted echo planar imaging in patients with recent myocardial infarction. *Eur Radiol* **21**(1):46-53.

DIERINGER, RENZ, LINDEL, SEIFERT, FRAUENRATH, VON KNOBELSDORFF-BRENKENHOFF, WAICZIES, HOFFMANN, RIEGER, PFEIFFER, ITTERMANN, SCHULZ-MENGER and NIENDORF (2011). Design and application of a four-channel transmit/receive surface coil for functional cardiac imaging at 7T. *J Magn Reson Imaging* **33**(3):736-741.

DOU, REESE, TSENG and WEDEEN (2002). Cardiac diffusion MRI without motion effects. *Magn Reson Med* **48**(1):105-114.

EDELMAN, GAA, WEDEEN, LOH, HARE, PRASAD and LI (1994). In vivo measurement of water diffusion in the human heart. *Magn Reson Med* **32**(3):423-428.

EHMAN and FELMLEE (1989). Adaptive technique for high-definition MR imaging of moving structures. *Radiology* **173**(1):255-263.

ERB-EIGNER, WILLERDING, TAUPITZ, HAMM and ASBACH (2013). Diffusion-Weighted Imaging of Ocular Melanoma. *Invest Radiol* **48**(10):702-707.

FEINBERG, HOENNINGER, CROOKS, KAUFMAN, WATTS and ARAKAWA (1985). Inner volume MR imaging: technical concepts and their application. *Radiology* **156**(3):743-747.

FEINBERG and JAKAB (1990). Tissue perfusion in humans studied by fourier velocity distribution, line scan, and echo-planar imaging. *Magn Reson Med* **16**(2):280-293.

FENG, OTAZO, JUNG, JENSEN, YE, SODICKSON and KIM (2011). Accelerated cardiac T_2 mapping using breath-hold multiecho fast spin-echo pulse sequence with k-t FOCUSS. *Magn Reson Med* **65**(6):1661-1669.

FICK (1855). V. On liquid diffusion. *Philosophical Magazine Series 4* **10**(63):30-39.

FINSTERBUSCH (2010). Double-spin-echo diffusion weighting with a modified eddy current adjustment. *Magn Reson Imaging* **28**(3):434-440.

FISCHER, MADERWALD, JOHST, ORZADA, LADD, UMUTLU, LAUENSTEIN, KNIEMEYER and NASSENSTEIN (2014). Initial Evaluation of Non–Contrast-Enhanced Magnetic Resonance Angiography in Patients With Peripheral Arterial Occlusive Disease at 7 T. *Invest Radiol* **49**(5):331-338.

FISCHER, WICKLINE and LORENZ (1999). Novel real-time R-wave detection algorithm based on the vectorcardiogram for accurate gated magnetic resonance acquisitions. *Magn Reson Med* **42**(2):361-370.

FRANCONI, SONIER, SEGUIN, LE PAPE and AKOKA (1994). Acquisition of spin echo and stimulated echo by a single sequence: Application to MRI of diffusion. *Magn Reson Imaging* **12**(4):605-611.

FRAUENRATH, HEZEL, HEINRICHS, KOZERKE, UTTING, KOB, BUTENWEG, BOESIGER and NIENDORF (2009). Feasibility of Cardiac Gating Free of Interference With Electro-Magnetic Fields at 1.5 Tesla, 3.0 Tesla and 7.0 Tesla Using an MR-Stethoscope. *Invest Radiol* **44**(9):539-547

FRAUENRATH, HEZEL, RENZ, DE GEYER, DIERINGER, KNOBELSDORFF-BRENKENHOFF, PROTHMANN, SCHULZ-MENGER and NIENDORF (2010). Acoustic cardiac triggering: a practical solution for synchronization and gating of cardiovascular magnetic resonance at 7 Tesla. *J Cardiovasc Magn Reson* **12**(1):67.

FRAUENRATH, NIENDORF and MALTE (2008). Acoustic Method for Synchronization of Magnetic Resonance Imaging (MRI). *Acta Acust United Ac* **94**(1):148-155.

FUCHS, HEZEL, KLIX, MEKLE, WUERFEL and NIENDORF (2014a). On the Application of Simultaneous Dual Contrast Weighting Using Double Echo 2in1-RARE in Healthy Subjects and Multiple Sclerosis Patients. *Proc. Intl. Soc. Mag. Reson. Med. (22)*:1492.

FUCHS, HEZEL, KLIX, MEKLE, WUERFEL and NIENDORF (2014b). Simultaneous dual contrast weighting using double echo rapid acquisition with relaxation enhancement (RARE) imaging. *Magn Reson Med* **72**(6):1590-1598.

FUCHS, HEZEL, OEZERDEM, WINTER and NIENDORF (2014c). Myocardial T_2^* Mapping Free of Distortion Using Susceptibility Weighted RARE Imaging at 7 Tesla. *Proc. Intl. Soc. Mag. Reson. Med. (22)*:2443.

FUCHS, HEZEL, WINTER, OEZERDEM, GRAESSL, DIERINGER, KRAUS and NIENDORF (2013). Feasibility of Cardiac Fast Spin Echo Imaging at 7.0 T Using a Two-Dimensional 16 Channel Array of Bowtie Transceivers. *Proc. Intl. Soc. Mag. Reson. Med. (21)* 1412.

FUCHS, RIEGER, GRAESSL and NIENDORF (2014d). Diffusion Sensitized Ophthalmic MRI Free of Distortion Using Multi-Shot RARE at 3 T and 7 T. *Proc. Intl. Soc. Mag. Reson. Med. (22)*:994.

GAMPER, BOESIGER and KOZERKE (2007). Diffusion imaging of the in vivo heart using spin echoes - considerations on bulk motion sensitivity. *Magn Reson Med* **57**(2):331-337.

GARWOOD and KE (1991). Symmetric pulses to induce arbitrary flip angles with compensation for rf inhomogeneity and resonance offsets. *J Magn Reson* **94**(3):511-525.

GERLACH and STERN (1924). Über die Richtungsquantelung im Magnetfeld. *Ann Phys* **379**(16):673-699.

GLOVER and PAULY (1992). Projection Reconstruction Techniques for Reduction of Motion Effects in MRI. *Magn Reson Med* **28**(2):275-289.

GMITRO and ALEXANDER (1993). Use of a projection reconstruction method to decrease motion sensitivity in diffusion-weighted MRI. *Magn Reson Med* **29**(6):835-838.

GOMORI, HOLLAND, GROSSMAN, GEFTER and LENKINSKI (1988). Fat suppression by section-select gradient reversal on spin-echo MR imaging. Work in progress. *Radiology* **168**(2):493-495.

GRAESSL, MUHLE, SCHWERTER, RIEGER, OEZERDEM, SANTORO, LYSIAK, WINTER, HEZEL, WAICZIES, GUTHOFF, FALKE, HOSTEN, HADLICH, KRUEGER, LANGNER, STACHS and NIENDORF (2014a). Ophthalmic magnetic resonance imaging at 7 T using a 6-channel transceiver radiofrequency coil array in healthy subjects and patients with intraocular masses. *Invest Radiol* **49**(5):260-270.

GRAESSL, RENZ, HEZEL, DIERINGER, WINTER, OEZERDEM, RIEGER, KELLMAN, SANTORO, LINDEL, FRAUENRATH, PFEIFFER and NIENDORF (2014b). Modular 32-channel transceiver coil array for cardiac MRI at 7.0T. *Magn Reson Med* **72**(1):276-290.

GRAESSL, WINTER, OEZERDEM, HEZEL, FUCHS, PFEIFFER, HOFFMANN and NIENDORF (2013). A two-dimensional 16 Channel Dipole Transceiver Array for Cardiac MR at 7.0 T: Design, Evaluation of RF Shimming Behavior and Application in CINE Imaging *Proc. Intl. Soc. Mag. Reson. Med. (21)*:395.

GRAESSL, WINTER, THALHAMMER, RENZ, KELLMAN, MARTIN, VON KNOBELSDORFF-BRENKENHOFF, TKACHENKO, SCHULZ-MENGER and NIENDORF (2011). Design, evaluation and application of an eight channel transmit/receive coil array for cardiac MRI at 7.0T. *Eur J Radiol* **82**(5):752-759.

GRISWOLD, JAKOB, CHEN, GOLDFARB, MANNING, EDELMAN and SODICKSON (1999). Resolution enhancement in single-shot imaging using simultaneous acquisition of spatial harmonics (SMASH). *Magn Reson Med* **41**(6):1236-1245.

GÜLLMAR, HAUEISEN and REICHENBACH (2005). Analysis of b-value calculations in diffusion weighted and diffusion tensor imaging. *Concept Magnetic Reson* **25A**(1):53-66.

GUTBERLET, NOESKE, SCHWINGE, FREYHARDT, FELIX and NIENDORF (2006). Comprehensive Cardiac Magnetic Resonance Imaging at 3.0 Tesla: Feasibility and Implications for Clinical Applications. *Invest Radiol* **41**(2).

H-ICI, RIDGWAY, KUEHNE, BERGER, PLEIN, SIVANANTHAN and MESSROGHLI (2012). Cardiovascular magnetic resonance of myocardial edema using a short inversion time inversion recovery (STIR) black-blood technique: diagnostic accuracy of visual and semi-quantitative assessment. *J Cardiov Magn Reson* **14:**22.

HAACKE, BROWN, THOMPSON and VENKATESAN (1999). *Magnetic Resonance Imaging, Physical Principles and Sequence Design*. New York: John Wiley & Sons.

HAACKE, XU, CHENG and REICHENBACH (2004). Susceptibility weighted imaging (SWI). *Magn Reson Med* **52**(3):612-618.

HAASE, FRAHM, MATTHAEI, HANICKE and MERBOLDT (1986). FLASH imaging. Rapid NMR imaging using low flip-angle pulses. *J Magn Reson* **67**(2):258-266.

HAHN (1950). Spin Echoes. *Phys Rev* **80**(4):580-594.

HAN, LARSON, LIU and KRUG (2014). Depiction of Achilles Tendon Microstructure In Vivo Using High-Resolution 3-Dimensional Ultrashort Echo-Time Magnetic Resonance Imaging at 7 T. *Invest Radiol* **49**(5):339-345.

HEIDEMANN, PORTER, ANWANDER, FEIWEIER, HEBERLEIN, KNOSCHE and TURNER (2010). Diffusion imaging in humans at 7T using readout-segmented EPI and GRAPPA. *Magn Reson Med* **64**(1):9-14.

HEINRICHS, UTTING, FRAUENRATH, HEZEL, KROMBACH, HODENIUS, KOZERKE and NIENDORF (2009). Myocardial T_2^* mapping free of distortion using susceptibility-weighted fast spin-echo imaging: a feasibility study at 1.5 T and 3.0 T. *Magn Reson Med* **62**(3):822-828.

HENKELMAN (1985). Measurement of signal intensities in the presence of noise in MR images. *Med Phys* **12**(2):232-233.

HENNIG (1988a). Multiecho imaging sequences with low refocusing flip angles. *J Magn Reson* **78**(3):397-407.

HENNIG (1991a). Echoes - How to Generate, Recognize, Use or Avoid them in MR-Imaging Sequences. Part I: Fundamental and Not So Fundamental Properties of Spin Echoes. *Concepts Magn Reson* **3**(3):125-143.

HENNIG (1991b). Echoes - How to Generate, Recognize, Use or Avoid them in MR-Imaging Sequences. Part II: Echoes in Imaging Sequences. *Concepts Magn Reson* **3**(4):179-192.

HENNIG and FRIEDBURG (1988b). Clinical applications and methodological developments of the RARE technique. *Magn Reson Imaging* **6**(4):391-395.

HENNIG, NAUERTH and FRIEDBURG (1986). RARE imaging: A fast imaging method for clinical MR. *Magn Reson Med* **3**(6):823-833.

HENNIG, NAUERTH, FRIEDBURG and RATZEL (1984). Ein neues Schnellbildverfahren für die Kernspintomographie. *Der Radiologe* **24:**579-580.

HEZEL, THALHAMMER, WAICZIES, SCHULZ-MENGER and NIENDORF (2012). High Spatial Resolution and Temporally Resolved T_2^* Mapping of Normal Human Myocardium at 7.0 Tesla: An Ultrahigh Field Magnetic Resonance Feasibility Study. *PLoS ONE* **7**(12):e52324.

HIGUCHI, OSHIO, MOMOSHIMA, SHIGA, MELKI, RV. and FA (1991). Two-Contrast RARE: A Fast Spin-Density and T_2-Weighted Imaging Method. *J Magn Reson Imaging* **1:**147.

HOFFMAN (2006). Standardization of chemical shifts of TMS and solvent signals in NMR solvents. *Magnetic Resonance in Chemistry* **44**(6):606-616.

HOLZ, HEIL and SACCO (2000). Temperature-dependent self-diffusion coefficients of water and six selected molecular liquids for calibration in accurate 1H NMR PFG measurements. *Phys Chem Chem Phys* **2**(20):4740-4742.

HONG and DIXON (1992). Measuring diffusion in inhomogeneous systems in imaging mode using antisymmetric sensitizing gradients. *J Magn Reson* **99**(3):561-570.

HUELNHAGEN, HEZEL and NIENDORF (2014a). En Route to Probing Humang Myocardial Microstructure in vivo using Susceptibility Based MRI at 7.0 T. *Proc. Intl. Soc. Mag. Reson. Med. (22)*:1436.

HUELNHAGEN, PAUL, NIENDORF, GRAESSL, RIEGER, LYSIAK, PROTHMANN, SCHULZ MENGER and NIENDORF (2015). Towards clinical cardiac MR at 7.0 T: Early experience with black blood RARE imaging in patients with hypertrophic cardiomyopathy. *Proc. Intl. Soc. Mag. Reson. Med. (23)*:2647.

HUELNHAGEN, POHLMANN, HEZEL, PEPER, KU and NIENDORF (2014b). Detailing Myocardial Microstructure in the Ex Vivo Rat Heart Using High Isotropic Spatial Resolution Susceptibility Weighted MRI and Quantitative Susceptibility Mapping. *Proc. Intl. Soc. Mag. Reson. Med. (22)*:2437.

HUNDLEY, BLUEMKE, FINN, FLAMM, FOGEL, FRIEDRICH, HO, JEROSCH-HEROLD, KRAMER, MANNING, PATEL, POHOST, STILLMAN, WHITE and WOODARD (2010). ACCF/ACR/AHA/NASCI/SCMR 2010 Expert Consensus Document on Cardiovascular Magnetic ResonanceA Report of the American College of Cardiology Foundation Task Force on Expert Consensus Documents. *J Am Coll Cardiol* **55**(23):2614-2662.

IPEK, RAAIJMAKERS, KLOMP, LAGENDIJK, LUIJTEN and BERG (2012). Characterization of transceive surface element designs for 7 tesla magnetic resonance imaging of the prostate: radiative antenna and microstrip. *Phys Med Biol* **57**(2):343-355.

JEZZARD (2012). Correction of geometric distortion in fMRI data. *Neuroimage* **62**(2):648-651.

JOHST, ORZADA, FISCHER, UMUTLU, LADD and MADERWALD (2014). Comparison of Fat Saturation Techniques for Single-Shot Fast Spin Echo Sequences for 7-T Body Imaging. *Invest Radiol* **49**(2):101-108.

JONES, MULKERN, MANTELLO, MELKI, AHN, BARNES and JOLESZ (1992). Brain hemorrhage: evaluation with fast spin-echo and conventional dual spin-echo images. *Radiology* **182**(1):53-58.

KAISER, BARTHOLDI and ERNST (1974). Diffusion and field-gradient effects in NMR Fourier spectroscopy. *J Chem Phys* **60**(8):2966-2979.

KAPUR, SEPAHDARI, MAFEE, PUTTERMAN, AAKALU, WENDEL and SETABUTR (2009). MR Imaging of Orbital Inflammatory Syndrome, Orbital Cellulitis, and Orbital Lymphoid Lesions: The Role of Diffusion-Weighted Imaging. *Am J Neuroradiol* **30**(1):64-70.

KATSCHER and BÖRNERT (2006). Parallel RF transmission in MRI. *NMR Biomed* **19**(3):393-400.

KATSCHER, BÖRNERT, LEUSSLER and VAN DEN BRINK (2003). Transmit SENSE. *Magn Reson Med* **49**(1):144-150.

KELLMAN, HERZKA and HANSEN (2014). Adiabatic inversion pulses for myocardial T_1 mapping. *Magn Reson Med* **71**(4):1428-1434.

KELLMAN and MCVEIGH (2005). Image reconstruction in SNR units: a general method for SNR measurement. *Magn Reson Med* **54**(6):1439-1447.

KHURANA, EISENHUT, WAN, EBRAHIMI, PATEL, O'BRIEN, YEOM and DALDRUP-LINK (2013). Comparison of the diagnostic value of MR imaging and ophthalmoscopy for the staging of retinoblastoma. *Eur Radiol* **23**(5):1271-1280.

KIM, HU, ADRIANY and UĞURBIL (1996). Fast interleaved echo-planar imaging with navigator: high resolution anatomic and functional images at 4 Tesla. *Magn Reson Med* **35**(6):895-902.

KLIX, HEZEL, FUCHS, RUFF, DIERINGER and NIENDORF (2014). Accelerated Fast Spin-Echo Magnetic Resonance Imaging of the Heart Using a Self-Calibrated Split-Echo Approach. *PLoS One* **9**(4):e94654.

KOCIEMBA, PYDA, KATULSKA, ŁANOCHA, SINIAWSKI, JANUS and GRAJEK (2013). Comparison of diffusion-weighted with T2-weighted imaging for detection of edema in acute myocardial infarction. *J Cardiov Magn Reson* **15**(1):1-8.

KOEHLER, HILLER, WALLER, JAKOB, BAUER and HAASE (2003). Visualization of myocardial microstructure using high-resolution T2* imaging at high magnetic field. *Magn Reson Med* **49**(2):371-375.

KRAFF, FISCHER, NAGEL, MÖNNINGHOFF and LADD (2015). MRI at 7 tesla and above: Demonstrated and potential capabilities. *J Magn Reson Imaging* **41:**13-33.

KRAMER, BARKHAUSEN, FLAMM, KIM and NAGEL (2008). Standardized cardiovascular magnetic resonance imaging (CMR) protocols, society for cardiovascular magnetic resonance: board of trustees task force on standardized protocols. *J Cardiov Magn Reson* **10**(1):35.

KRAMER, BARKHAUSEN, FLAMM, KIM and NAGEL (2013). Standardized cardiovascular magnetic resonance (CMR) protocols 2013 update. *J Cardiov Magn Reson* **15**(1):1-10.

LADD (2007). High-Field-Strength Magnetic Resonance: Potential and Limits. *Top Magn Reson Imaging* **18**(2).

LAISSY, SERFATY, MESSIKA-ZEITOUN, RIBET, CHILLON, STEG and KLEIN (2009). Cardiac diffusion MRI of recent and chronic myocardial infarction: preliminary results. *J Radiol* **90**(4):481-484.

LANDOLT and BÖRNSTEIN (1969). *Zahlenwerte und Funktionen aus Physik, Chemie, Astronomie, Geophysik und Technik*. Berlin Heidelberg New York: Springer-Verlag.

LANGNER, KRUEGER, STACHS and HOSTEN (2011). [MR microscopy of the human eye]. *Klin Monatsbl Augenheilkd* **228**(12):1073-1078.

LANZER, BARTA, BOTVINICK, WIESENDANGER, MODIN and HIGGINS (1985). ECG-synchronized cardiac MR imaging: method and evaluation. *Radiology* **155**(3):681-686.

LANZER, BOTVINICK, SCHILLER, CROOKS, ARAKAWA, KAUFMAN, DAVIS, HERFKENS, LIPTON and HIGGINS (1984). Cardiac imaging using gated magnetic resonance. *Radiology* **150**(1):121-127.

LARSON, WHITE, LAUB, MCVEIGH, LI and SIMONETTI (2004). Self-gated cardiac cine MRI. *Magn Reson Med* **51**(1):93-102.

LE BIHAN and BRETON (1985). Imagerie de diffusion in-vivo par resonance magnetique nucleaire. *Comptes-Rendus de l'Académie des Sciences* **93**(5):27-34.

LE BIHAN, BRETON, LALLEMAND, GRENIER, CABANIS and LAVAL-JEANTET (1986). MR imaging of intravoxel incoherent motions: application to diffusion and perfusion in neurologic disorders. *Radiology* **161**(2):401-407.

LE BIHAN, MANGIN, POUPON, CLARK, PAPPATA, MOLKO and CHABRIAT (2001). Diffusion tensor imaging: Concepts and applications. *J Magn Reson Imaging* **13**(4):534-546.

LENHART, DESAI, BRUCE, HUTCHINSON and LAMBERT (2014). The Role of Magnetic Resonance Imaging in Diagnosing Optic Nerve Hypoplasia. *Am J Ophthalmol* **158**(6):1164-1171.e1162.

LI and LEIGH (2004). Quantifying arbitrary magnetic susceptibility distributions with MR. *Magn Reson Med* **51**(5):1077-1082.

LINDNER, LANGNER, GRAESSL, RIEGER, SCHWERTER, MUHLE, LYSIAK, KRAUS, WUERFEL, GUTHOFF, FALKE, HADLICH, KRUEGER, HOSTEN, NIENDORF and STACHS (2014). High spatial resolution in vivo magnetic resonance imaging of the human eye, orbit, nervus opticus and optic nerve sheath at 7.0 Tesla. *Exp Eye Res* **125:**89-94.

LIU, LI, WU, JIANG and JOHNSON (2012). 3D fiber tractography with susceptibility tensor imaging. *Neuroimage* **59**(2):1290-1298.

LORENZ, PASTOREK and BUNDY (2000). Delineation of normal human left ventricular twist throughout systole by tagged cine magnetic resonance imaging. *J Cardiov Magn Reson* **2**(2):97-108.

MAFEE, KARIMI, SHAH, RAPOPORT and ANSARI (2005). Anatomy and Pathology of the Eye: Role of MR Imaging and CT. *Neuroimag Clin N Am* **15**(1):23-47.

MALHOTRA, MINJA, CRUM and BURROWES (2011). Ocular Anatomy and Cross-Sectional Imaging of the Eye. *Semin Ultrasound CT MR* **32**(1):2-13.

MANSFIELD (1977a). Multi-planar image formation using NMR spin echoes. *J Phys C* **10**(3):L55.

MANSFIELD and MAUDSLEY (1977b). Planar spin imaging by NMR. *J Magn Reson* **27**(1):101-119.

MANSFIELD, ORDIDGE and COXON (1988). Zonally magnified EPI in real time by NMR. *J Phys E* **21**(3):275.

MATHUR, KARIMI and MAFEE (2007). Acute Optic Nerve Infarction Demonstrated by Diffusion-Weighted Imaging in a Case of Rhinocerebral Mucormycosis. *Am J Neuroradiol* **28**(3):489-490.

MCNAB, EDLOW, WITZEL, HUANG, BHAT, HEBERLEIN, FEIWEIER, LIU, KEIL, COHEN-ADAD, TISDALL, FOLKERTH, KINNEY and WALD (2013). The Human Connectome Project and beyond: Initial applications of 300 mT/m gradients. *Neuroimage* **80:**234-245.

MEIBOOM and GILL (1958). Modified Spin-Echo Method for Measuring Nuclear Relaxation Times. *Rev Sci Instrum* **29**(8):688-691.

MELKI, MULKERN, PANYCH and JOLESZ (1991). Comparing the FAISE method with conventional dual-echo sequences. *J Magn Reson Imaging* **1**(3):319-326.

MELONI, HEZEL, POSITANO, KEILBERG, PEPE, LOMBARDI and NIENDORF (2014). Detailing magnetic field strength dependence and segmental artifact distribution of myocardial effective transverse relaxation rate at 1.5, 3.0, and 7.0 T. *Magn Reson Med* **71**(6):2224-2230.

MORI and VAN ZIJL (1998). A motion correction scheme by twin-echo navigation for diffusion-weighted magnetic resonance imaging with multiple RF echo acquisition. *Magn Reson Med* **40**(4):511-516.

MOSELEY, COHEN, MINTOROVITCH, CHILEUITT, SHIMIZU, KUCHARCZYK, WENDLAND and WEINSTEIN (1990). Early detection of regional cerebral ischemia in cats: Comparison of diffusion- and T_2-weighted MRI and spectroscopy. *Magn Reson Med* **14**(2):330-346.

MOSER, STAHLBERG, LADD and TRATTNIG (2012). 7-T MR—from research to clinical applications? *NMR Biomed* **25**(5):695-716.

MULKERN, MELKI, JAKAB, HIGUCHI and JOLESZ (1991). Phase-encode order and its effect on contrast and artifact in single-shot RARE sequences. *Med Phys* **18**(5):1032-1037.

MULKERN, WONG, WINALSKI and JOLESZ (1990). Contrast manipulation and artifact assessment of 2D and 3D RARE sequences. *Magn Reson Imaging* **8**(5):557-566.

MÜLLER, KUCHLING, DÖRR, HARMS, RUPRECHT, NIENDORF, WUERFEL, PAUL and SINNECKER (2014). Detailing intra-lesional venous lumen shrinking in multiple sclerosis investigated by sFLAIR MRI at 7-T. *J Neurol* **261**(10):2032-2036.

NAGY and WEISKOPF (2008). Efficient fat suppression by slice-selection gradient reversal in twice-refocused diffusion encoding. *Magn Reson Med* **60**(5):1256-1260.

NEEMA, GOLDBERG-ZIMRING, GUSS, HEALY, GUTTMANN, HOUTCHENS, WEINER, HORSFIELD, HACKNEY, ALSOP and BAKSHI (2009). 3 T MRI relaxometry detects T_2 prolongation in the cerebral normal-appearing white matter in multiple sclerosis. *Neuroimage* **46**(3):633-641.

NIELLES-VALLESPIN, MEKKAOUI, GATEHOUSE, REESE, KEEGAN, FERREIRA, COLLINS, SPEIER, FEIWEIER, DE SILVA, JACKOWSKI, PENNELL, SOSNOVIK and FIRMIN (2013). In vivo diffusion tensor MRI of the human heart: Reproducibility of breath-hold and navigator-based approaches. *Magn Reson Med* **70**(2):454-465.

NIENDORF (1999). On the application of susceptibility-weighted ultra-fast low-angle RARE experiments in functional MR imaging. *Magn Reson Med* **41**(6):1189-1198.

NIENDORF, DIJKHUIZEN, NORRIS, VAN LOOKEREN CAMPAGNE and NICOLAY (1996). Biexponential diffusion attenuation in various states of brain tissue: Implications for diffusion-weighted imaging. *Magn Reson Med* **36**(6):847-857.

NIENDORF, GRAESSL, THALHAMMER, DIERINGER, KRAUS, SANTORO, FUCHS, HEZEL, WAICZIES, ITTERMANN and WINTER (2013). Progress and promises of human cardiac magnetic resonance at ultrahigh fields: a physics perspective. *J Magn Reson* **229:**208-222.

NIENDORF, PAUL, GRAESSL, ELS, POHLMANN, RIEGER, LINDNER, KRUEGER, HADLICH, LANGNER and STACHS (2014). Ophthalmologische Bildgebung mit Ultrahochfeld-Magnetresonanztomografie:

technische Innovationen und wegweisende Anwendungen. *Klin Monatsbl Augenheilkd* **231**(12):1187-1195.

NIENDORF, PAUL, ÖZERDEM, GRAESSL, KLIX, HUELNHAGEN, RIEGER, WAICZIES, OBERACKER and WINTER (2015). W(h)ither Cardiac and Body Ultrahigh Field Magnetic Resonance. *NMR Biomed*, doi: (accepted).

NIJM, SAHAKIAN, SWIRYN, CARR, SHEEHAN and LARSON (2008). Comparison of self-gated cine MRI retrospective cardiac synchronization algorithms. *J Magn Reson Imaging* **28**(3):767-772.

NORRIS (1991). Ultrafast Low-Angle RARE: U-FLARE. *Magn Reson Med* **17**(2):539-542.

NORRIS, BOERNERT, REESE and LEIBFRITZ (1992). On the application of ultra-fast rare experiments. *Magn Reson Med* **27**(1):142-164.

NORRIS and BORNERT (1993a). Coherence and Interference in Ultrafast RARE Experiments. *J Magn Reson* **105**(2):123-127.

NORRIS, BOYACIOGLU, SCHULZ, BARTH and KOOPMANS (2014). Application of PINS radiofrequency pulses to reduce power deposition in RARE/turbo spin echo imaging of the human head. *Magn Reson Med* **71**(1):44-49.

NORRIS and HAASE (1989). Variable excitation angle AFP pulses. *Magn Reson Med* **9**(3):435-440.

NORRIS, HOEHN-BERLAGE, WITTLICH, BACK and LEIBFRITZ (1993b). Dynamic imaging with T_2^* contrast using U-FLARE. *Magn Reson Imaging* **11**(7):921-924.

NORRIS, KOOPMANS, BOYACIOGLU and BARTH (2011). Power Independent of Number of Slices (PINS) radiofrequency pulses for low-power simultaneous multislice excitation. *Magn Reson Med* **66**(5):1234-1240.

OEZERDEM, WINTER, FUCHS and NIENDORF (2013). Towards Ultimate SNR: Combination of a Multi-Element TX/RX Dipole Antenna Array with Nested and Meander Shaped RX Dipole Antenna at 7.0 Tesla *Proc. Intl. Soc. Mag. Reson. Med. (21)*:394.

ONG, CHIN, WEHRLI, TANG and WEHRLI (2005). A new approach for simultaneous measurement of ADC and T_2 from echoes generated via multiple coherence transfer pathways. *J Magn Reson* **173**(1):153-159.

ORDIDGE, HELPERN, QING, KNIGHT and NAGESH (1994). Correction of motional artifacts in diffusion-weighted MR images using navigator echoes. *Magn Reson Imaging* **12**(3):455-460.

OSHIO, JOLESZ, MELKI and MULKERN (1991). T_2-weighted thin-section imaging with the multislab three-dimensional RARE technique. *J Magn Reson Imaging* **1**(6):695-700.

PAPADOPOULOU, MOULIN, ZOGRAFOS and SCHALENBOURG (2012). How would you manage this small melanocytic choroidal tumour? *Br J Ophthalmol* **96**(12):1530-1530.

PARK, KIM and CHO (1987). Gradient reversal technique and its applications to chemical-shift-related NMR imaging. *Magn Reson Med* **4**(6):526-536.

PATZ, BERT, FREDERICK and FREDDO (2007). T1 and T2 measurements of the fine structures of the in vivo and enucleated human eye. *J Magn Reson Imaging* **26**(3):510-518.

PAUL, GRAESSL, RIEGER, LYSIAK, HUELNHAGEN, WINTER, HEIDEMANN, LINDNER, HADLICH, ZIMPFER, POHLMANN, KRÜGER, LANGNER, STACHS and NIENDORF (2015). Diffusion-Sensitized Ophthalmic

MRI Free of Geometric Distortion at 3.0 T and 7.0 T: A Feasibility Study in Healthy Subjects and Patients with Intraocular Masses. *Invest Radiol* **50**(5):309-321.

PAULY, NISHIMURA and MACOVSKI (1989). A k-space analysis of small-tip-angle excitation. *J Magn Reson* **81**(1):43-56.

PETERS, BROOKES, HOOGENRAAD, GOWLAND, FRANCIS, MORRIS and BOWTELL (2007). T2* measurements in human brain at 1.5, 3 and 7 T. *Magn Reson Imaging* **25**(6):748-753.

PINELES, DEMER, HOLLAND, RANSOME, BONELLI and VELEZ (2012). External ophthalmoplegia in human immunodeficiency virus-infected patients receiving antiretroviral therapy. *J Pediatr Ophtalmol Strabismus* **16**(6):529-533.

PIPE (1999). Motion correction with PROPELLER MRI: Application to head motion and free-breathing cardiac imaging. *Magn Reson Med* **42**(5):963-969.

PIPE and ZWART (2006). Turboprop: improved PROPELLER imaging. *Magn Reson Med* **55**(2):380-385.

POHLMANN, CANTOW, HENTSCHEL, ARAKELYAN, LADWIG, FLEMMING, HOFF, PERSSON, SEELIGER and NIENDORF (2013a). Linking non-invasive parametric MRI with invasive physiological measurements (MR-PHYSIOL): towards a hybrid and integrated approach for investigation of acute kidney injury in rats. *Acta Physiol* **207**(4):673-689.

POHLMANN, HENTSCHEL, FECHNER, HOFF, BUBALO, ARAKELYAN, CANTOW, SEELIGER, FLEMMING, WAICZIES, WAICZIES, SCHUNCK, DRAGUN and NIENDORF (2013b). High Temporal Resolution Parametric MRI Monitoring of the Initial Ischemia/Reperfusion Phase in Experimental Acute Kidney Injury. *PLoS ONE* **8**(2):e57411.

PORTER and HEIDEMANN (2009). High resolution diffusion-weighted imaging using readout-segmented echo-planar imaging, parallel imaging and a two-dimensional navigator-based reacquisition. *Magn Reson Med* **62**(2):468-475.

PRICE (1997). Pulsed-field gradient nuclear magnetic resonance as a tool for studying translational diffusion: Part 1. Basic theory. *Concept Magnetic Reson* **9**(5):299-336.

PRUESSMANN, WEIGER, SCHEIDEGGER and BOESIGER (1999). SENSE: Sensitivity encoding for fast MRI. *Magn Reson Med* **42:**952-962.

PURCELL, TORREY and POUND (1946). Resonance Absorption by Nuclear Magnetic Moments in a Solid. *Phys Rev* **69**(1-2):37-38.

RAAIJMAKERS, IPEK, KLOMP, POSSANZINI, HARVEY, LAGENDIJK and VAN DEN BERG (2011). Design of a radiative surface coil array element at 7 T: the single-side adapted dipole antenna. *Magn Reson Med* **66**(5):1488-1497.

RABI, ZACHARIAS, MILLMAN and KUSCH (1938). A New Method of Measuring Magnetic Moments. *Phys Rev* **52:**318.

RAPACCHI, WEN, VIALLON, GRENIER, KELLMAN, CROISILLE and PAI (2011). Low b-Value Diffusion-Weighted Cardiac Magnetic Resonance Imaging: Initial Results in Humans Using an Optimal Time-Window Imaging Approach. *Invest Radiol* **46**(12):751-758.

REESE, HEID, WEISSKOFF and WEDEEN (2003). Reduction of eddy-current-induced distortion in diffusion MRI using a twice-refocused spin echo. *Magn Reson Med* **49**(1):177-182.

REESE, WEDEEN and WEISSKOFF (1996). Measuring Diffusion in the Presence of Material Strain. *J Magn Reson,Ser B* **112**(3):253-258.

REESE, WEISSKOFF, SMITH, ROSEN, DINSMORE and WEDEEN (1995). Imaging myocardial fiber architecture in vivo with magnetic resonance. *Magn Reson Med* **34**(6):786-791.

RICHDALE, WASSENAAR, TEAL BLUESTEIN, ABDULJALIL, CHRISTOFORIDIS, LANZ, KNOPP and SCHMALBROCK (2009). 7 Tesla MR imaging of the human eye in vivo. *J Magn Reson Imaging* **30**(5):924-932.

RITCHIE, LEE, FEENEY and LINGAM (2014). Using Nonechoplanar Diffusion-weighted MRI to Assess Treatment Response in Active Graves Orbitopathy: A Novel Approach with 2 Case Reports. *Ophthal Plast Reconstr Surg*, doi: 10.1097/IOP.0000000000000248.

ROCCA, ANZALONE, FALINI and FILIPPI (2013). Contribution of magnetic resonance imaging to the diagnosis and monitoring of multiple sclerosis. *Radiol Med* **118**(2):251-264.

RODGERS, PIECHNIK, DELABARRE, VAN DE MOORTELE, SNYDER, NEUBAUER, ROBSON and VAUGHAN (2013). Inversion recovery at 7 T in the human myocardium: Measurement of T_1 , inversion efficiency and B_1^+. *Magn Reson Med* **70**(4):1038-1046.

ROONEY, JOHNSON, LI, COHEN, KIM, UGURBIL and SPRINGER (2007). Magnetic field and tissue dependencies of human brain longitudinal ^1H_2O relaxation in vivo. *Magn Reson Med* **57**(2):308-318.

ROSSMANN (1969). Point Spread-Function, Line Spread-Function, and Modulation Transfer Function. *Radiology* **93**(2):257-272.

RUMBOLDT, MOSES, WIECZERZYNSKI and SAINI (2005). Diffusion-Weighted Imaging, Apparent Diffusion Coefficients, and Fluid-Attenuated Inversion Recovery MR Imaging in Endophthalmitis. *Am J Neuroradiol* **26**(7):1869-1872.

RYDBERG, RIEDERER, RYDBERG and JACK (1995). Contrast optimization of fluid-attenuated inversion recovery (flair) imaging. *Magn Reson Med* **34**(6):868-877.

SAEKHO, YIP, NOLL, BOADA and STENGER (2006). Fast-kz three-dimensional tailored radiofrequency pulse for reduced B1 inhomogeneity. *Magn Reson Med* **55**(4):719-724.

SCHAEFER, GRANT and GONZALEZ (2000). Diffusion-weighted MR Imaging of the Brain. *Radiology* **217**(2):331-345.

SCHICK (1997). SPLICE: Sub-second diffusion-sensitive MR imaging using a modified fast spin-echo acquisition mode. *Magn Reson Med* **38**(4):638-644.

SCHMITTER, DELABARRE, WU, GREISER, WANG, AUERBACH, VAUGHAN, UGURBIL and VAN DE MOORTELE (2013). Cardiac imaging at 7 tesla: Single- and two-spoke radiofrequency pulse design with 16-channel parallel excitation. *Magn Reson Med* **70**(5):1210-1219.

SEELOS, VON SMEKAL, VAHLENSIECK, GIESEKE and REISER (1993). Cardiac abnormalities: assessment with T_2-weighted turbo spin-echo MR imaging with electrocardiogram gating at 0.5 T. *Radiology* **189**(2):517-522.

SEIFERT, JAKOB, JELLUS, HAASE and HILLENBRAND (2000). High-Resolution Diffusion Imaging Using a Radial Turbo-Spin-Echo Sequence: Implementation, Eddy Current Compensation, and Self-Navigation. *J Magn Reson* **144**(2):243-254.

SEPAHDARI, AAKALU, KAPUR, MICHALS, SARAN, FRENCH and MAFEE (2009). MRI of Orbital Cellulitis and Orbital Abscess: The Role of Diffusion-Weighted Imaging. *Am J Roentgenol* **193**(3):W244-W250.

SEPAHDARI, AAKALU, SETABUTR, SHIEHMORTEZA, NAHEEDY and MAFEE (2010). Indeterminate Orbital Masses: Restricted Diffusion at MR Imaging with Echo-planar Diffusion-weighted Imaging Predicts Malignancy. *Radiology* **256**(2):554-564.

SEPAHDARI, KAPUR, AAKALU, VILLABLANCA and MAFEE (2012). Diffusion-Weighted Imaging of Malignant Ocular Masses: Initial Results and Directions for Further Study. *Am J Neuroradiol* **33**(2):314-319.

SEPAHDARI, POLITI, AAKALU, KIM and RAZEK (2014). Diffusion-Weighted Imaging of Orbital Masses: Multi-Institutional Data Support a 2-ADC Threshold Model to Categorize Lesions as Benign, Malignant, or Indeterminate. *Am J Neuroradiol* **35**(1):170-175.

SETSOMPOP, ALAGAPPAN, GAGOSKI, WITZEL, POLIMENI, POTTHAST, HEBRANK, FONTIUS, SCHMITT, WALD and ADALSTEINSSON (2008a). Slice-selective RF pulses for in vivo B 1+ inhomogeneity mitigation at 7 tesla using parallel RF excitation with a 16-element coil. *Magn Reson Med* **60**(6):1422-1432.

SETSOMPOP, ALAGAPPAN, ZELINSKI, POTTHAST, FONTIUS, HEBRANK, SCHMITT, WALD and ADALSTEINSSON (2008b). High-flip-angle slice-selective parallel RF transmission with 8 channels at 7 T. *J Magn Reson* **195**(1):76-84.

SIJBERS, DEN DEKKER, VAN AUDEKERKE, VERHOYE and VAN DYCK (1998). Estimation of the Noise in Magnitude MR Images. *Magn Reson Imaging* **16**(1):87-90.

SILVER, JOSEPH and HOULT (1984). Highly selective π2 and π pulse generation. *J Magn Reson* **59**(2):347-351.

SIMONETTI, FINN, WHITE, LAUB and HENRY (1996). "Black blood" T_2-weighted inversion-recovery MR imaging of the heart. *Radiology* **199**(1):49-57.

SINNECKER, BOZIN, DÖRR, PFUELLER, HARMS, NIENDORF, BRANDT, PAUL and WUERFEL (2013). Periventricular venous density in multiple sclerosis is inversely associated with T2 lesion count: a 7 Tesla MRI study. *Mult Scler* **19**(3):316-325.

SINNECKER, DÖRR, PFUELLER, HARMS, RUPRECHT, JARIUS, BRÜCK, NIENDORF, WUERFEL and PAUL (2012). Distinct lesion morphology at 7-T MRI differentiates neuromyelitis optica from multiple sclerosis. *Neurology* **79**(7):708-714.

SNYDER, DELABARRE, METZGER, VAN DE MOORTELE, AKGUN, UGURBIL and VAUGHAN (2009). Initial results of cardiac imaging at 7 Tesla. *Magn Reson Med* **61**(3):517-524.

SODICKSON, HARDY, ZHU, GIAQUINTO, GROSS, KENWOOD, NIENDORF, LEJAY, MCKENZIE, OHLIGER, GRANT and ROFSKY (2005). Rapid Volumetric MRI Using Parallel Imaging With Order-of-Magnitude Accelerations and a 32-Element RF Coil Array: Feasibility and implications. *Acad Radiol* **12**(5):626-635.

SODICKSON and MANNING (1997). Simultaneous acquisition of spatial harmonics (SMASH): Fast imaging with radiofrequency coil arrays. *Magn Reson Med* **38**(4):591-603.

SONG and TANG (2004). A one-shot method for measurement of diffusion. *J Magn Reson* **170**(1):136-148.

STAEWEN, JOHNSON, ROSS, PARRISH, MERKLE and GARWOOD (1990). 3-D FLASH Imaging Using a Single Surface Coil and a New Adiabatic Pulse, BIR-4. *Invest Radiol* **25**(5):559-567.

STEJSKAL and TANNER (1965). Spin Diffusion Measurements: Spin Echoes in the Presence of a Time-Dependent Field Gradient. *J Chem Phys* **42**(1):288-292.

STRENK, STRENK and GUO (2006). Magnetic resonance imaging of aging, accommodating, phakic, and pseudophakic ciliary muscle diameters. *J Cataract Refract Surg* **32**(11):1792-1798.

TANNÚS and GARWOOD (1996). Improved Performance of Frequency-Swept Pulses Using Offset-Independent Adiabaticity. *J Magn Reson, Ser A* **120**(1):133-137.

TANNÚS and GARWOOD (1997). Adiabatic pulses. *NMR Biomed* **10**(8):423-434.

THALHAMMER, RENZ, WINTER, HEZEL, RIEGER, PFEIFFER, GRAESSL, SEIFERT, HOFFMANN, VON KNOBELSDORFF-BRENKENHOFF, TKACHENKO, SCHULZ-MENGER, KELLMAN and NIENDORF (2012). Two-Dimensional sixteen channel transmit/receive coil array for cardiac MRI at 7.0 T: Design, evaluation, and application. *J Magn Reson Imaging* **36**(4):847-857.

THOMAS, DE VITA, ROBERTS, TURNER, YOUSRY and ORDIDGE (2004). High-resolution fast spin echo imaging of the human brain at 4.7 T: Implementation and sequence characteristics. *Magn Reson Med* **51**(6):1254-1264.

TIEN, FELSBERG and MACFALL (1992). Practical choices of fast spin echo pulse sequence parameters: clinically useful proton density and T_2-weighted contrasts. *Neuroradiology* **35**(1):38-41.

TORREY (1956). Bloch Equations with Diffusion Terms. *Phys Rev* **104**(3):563-565.

TROUARD, THEILMANN, ALTBACH and GMITRO (1999). High-resolution diffusion imaging with DIFRAD-FSE (diffusion-weighted radial acquisition of data with fast spin-echo) MRI. *Magn Reson Med* **42**(1):11-18.

TURNER (1984). Multipulse NMR in liquids. *Prog Nucl Mag Res Sp* **16:**311-370.

TURNER, LE BIHAN, MAIER, VAVREK, HEDGES and PEKAR (1990). Echo-planar imaging of intravoxel incoherent motion. *Radiology* **177**(2):407-414.

ULLMANN, JUNGE, WICK, SEIFERT, RUHM and HENNIG (2005). Experimental analysis of parallel excitation using dedicated coil setups and simultaneous RF transmission on multiple channels. *Magn Reson Med* **54**(4):994-1001.

VAN ELDEREN, VERSLUIS, WEBB, WESTENBERG, DOORNBOS, SMITH, DE ROOS and STUBER (2009). Initial results on in vivo human coronary MR angiography at 7 T. *Magn Reson Med* **62**(6):1379-1384.

VAN KALLEVEEN, KONING, BOER, LUIJTEN, ZWANENBURG and KLOMP (2012). Adiabatic turbo spin echo in human applications at 7 T. *Magn Reson Med* **68**(2):580-587.

VAUGHAN, SNYDER, DELABARRE, BOLAN, TIAN, BOLINGER, ADRIANY, ANDERSEN, STRUPP and UGURBIL (2009). Whole-body imaging at 7T: Preliminary results. *Magn Reson Med* **61**(1):244-248.

VERHAERT, THAVENDIRANATHAN, GIRI, MIHAI, RAJAGOPALAN, SIMONETTI and RAMAN (2011). Direct T_2 Quantification of Myocardial Edema in Acute Ischemic Injury. *JACC: Cardiovascular Imaging* **4**(3):269-278.

VOLK, TIFFON, MISPELTER and LHOSTE (1987). Chemical shift-specific slice selection. A new method for chemical shift imaging at high magnetic field. *J Magn Reson* **71**168-174.

WALTER, NIENDORF, GRAESSL, RIEGER, KRÜGER, LANGNER, GUTHOFF and STACHS (2014). Ultrahigh field magnetic resonance and colour Doppler real-time fusion imaging of the orbit – a hybrid tool for assessment of choroidal melanoma. *Eur Radiol* **24**(5):1112-1117.

WAN, PARKER, LEE, BUSWELL and GULLBERG (1995). Reduction of phase error ghosting artifacts in thin slice fast spin-echo imaging. *Magn Reson Med* **34**(4):632-638.

WANG, RIEDERER and EHMAN (1995). Respiratory Motion of the Heart: Kinematics and the Implications for the Spatial Resolution in Coronary Imaging. *Magn Reson Med* **33**(5):713-719.

WARACH, GAA, SIEWERT, WIELOPOLSKI and EDELMAN (1995). Acute human stroke studied by whole brain echo planar diffusion-weighted magnetic resonance imaging. *Ann Neurol* **37**(2):231-241.

WASSMUTH, ABDEL-ATY, BOHL and SCHULZ-MENGER (2011). Prognostic impact of T2-weighted CMR imaging for cardiac amyloidosis. *Eur Radiol* **21**(8):1643-1650.

WEIGEL (2015). Extended phase graphs: Dephasing, RF pulses, and echoes - pure and simple. *J Magn Reson Imaging* **41**(2):266-295.

WEIR, EVANS, HAJDU and POTTS (2009). The Convex Retina: Optical Coherence Tomography in Hypermetropic Shift, Without Choroidal Folds, from Intraconal Cavernous Haemangioma. *Orbit* **28**(6):398-400.

WIGGINS, POLIMENI, POTTHAST, SCHMITT, ALAGAPPAN and WALD (2009). 96-Channel receive-only head coil for 3 Tesla: Design optimization and evaluation. *Magn Reson Med* **62**(3):754-762.

WIGGINS, TRIANTAFYLLOU, POTTHAST, REYKOWSKI, NITTKA and WALD (2006). 32-channel 3 Tesla receive-only phased-array head coil with soccer-ball element geometry. *Magn Reson Med* **56**(1):216-223.

WILLIAMS, REDPATH and NORRIS (1999). A novel fast split-echo multi-shot diffusion-weighted MRI method using navigator echoes. *Magn Reson Med* **41**(4):734-742.

WINTER, KELLMAN, RENZ, GRÄßL, HEZEL, THALHAMMER, KNOBELSDORFF-BRENKENHOFF, TKACHENKO, SCHULZ-MENGER and NIENDORF (2012). Comparison of three multichannel transmit/receive radiofrequency coil configurations for anatomic and functional cardiac MRI at 7.0T: implications for clinical imaging. *Eur Radiol* **22**(10):2211-2220.

WINTER, ÖZERDEM, HOFFMANN, SANTORO, MÜLLER, WAICZIES, SEEMANN, GRAESSL, WUST and NIENDORF (2013). Design and Evaluation of a Hybrid Radiofrequency Applicator for Magnetic Resonance Imaging and RF Induced Hyperthermia: Electromagnetic Field Simulations up to 14.0 Tesla and Proof-of-Concept at 7.0 Tesla. *PLoS One* **8**(4):e61661.

WOESSNER (1961). Effects of Diffusion in Nuclear Magnetic Resonance Spin-Echo Experiments. *J Chem Phys* **34**(6):2057-2061.

WONG (2012). Local head gradient coils: Window(s) of opportunity. *Neuroimage* **62**(2):660-664.

WU, TSENG, SU, LIU, CHIOU, WEDEEN, REESE and YANG (2006). Diffusion tensor magnetic resonance imaging mapping the fiber architecture remodeling in human myocardium after infarction: correlation with viability and wall motion. *Circulation* **114**(10):1036-1045.

WU, VAUGHAN, UĞURBIL and VAN DE MOORTELE (2010). Parallel excitation in the human brain at 9.4 T counteracting k-space errors with RF pulse design. *Magn Reson Med* **63**(2):524-529.

WUERFEL, SINNECKER, RINGELSTEIN, JARIUS, SCHWINDT, NIENDORF, PAUL, KLEFFNER and DÖRR (2012). Lesion morphology at 7 Tesla MRI differentiates Susac syndrome from multiple sclerosis. *Mult Scler* **18**(11):1592-1599.

XU, KING, ZHU, MCKINNON and LIANG (2007). A noniterative method to design large-tip-angle multidimensional spatially-selective radio frequency pulses for parallel transmission. *Magn Reson Med* **58**(2):326-334.

ZEINEH, PAREKH, ZAHARCHUK, SU, ROSENBERG, FISCHBEIN and RUTT (2014). Ultrahigh-Resolution Imaging of the Human Brain with Phase-Cycled Balanced Steady-State Free Precession at 7 T. *Invest Radiol* **49**(5):278-289.

ZHANG, NATERAS, PENG, KURANOV, HARRISON, MILNER and DUONG (2011). Lamina-Specific Anatomic Magnetic Resonance Imaging of the Human Retina. *Invest Ophthalmol Vis Sci* **52**(10):7232-7237.

ZHANG, NATERAS, PENG, ROSENDE and DUONG (2012). Blood Flow MRI of the Human Retina/Choroid during Rest and Isometric Exercise. *Invest Ophthalmol Vis Sci* **53**(7):4299-4305.

ZHU (2004a). Parallel excitation with an array of transmit coils. *Magn Reson Med* **51**(4):775-784.

ZHU, HARDY, SODICKSON, GIAQUINTO, DUMOULIN, KENWOOD, NIENDORF, LEJAY, MCKENZIE, OHLIGER and ROFSKY (2004b). Highly parallel volumetric imaging with a 32-element RF coil array. *Magn Reson Med* **52**(4):869-877.

ZIENER, KAMPF, MELKUS, JAKOB, SCHLEMMER and BAUER (2012). Signal evolution in the local magnetic field of a capillary — analogy to the damped driven harmonic oscillator. *Magn Reson Imaging* **30**(4):540-553.

ZUR and STOKAR (1987). A phase-cycling technique for canceling spurious echoes in NMR imaging. *J Magn Reson Imaging* **71**(2):212-228.

Selbstständigkeitserklärung

Hiermit versichere ich, dass ich die vorliegende Dissertation nur unter der Verwendung der angegebenen Hilfen und Hilfsmittel erstellt habe.

Berlin, July 2015

Katharina Paul

Acknowledgements

Lieber Herr Niendorf, zunächst möchte ich mich für die Möglichkeit bedanken, diese Promotionsarbeit in Ihrer Arbeitsgruppe durchführen zu dürfen. Die Freiräume, die Sie mir gewährt haben, sowie das entgegengebrachte Vertrauen haben maßgeblich zu meiner wissenschaftlichen Entwicklung und den erzielten Ergebnissen beigetragen.

Ich bedanke mich außerdem bei allen Kooperationspartnern, die durch Ihre Offenheit und die angenehme Zusammenarbeit meine Arbeit weitergebracht haben.

Liebes Team der Berlin Ultrahigh Field Facility, ich möchte mich bei euch für die angenehme Arbeitsatmosphäre bedanken. In unzähligen Diskussionen, Scannersessions und in den vielen Gesprächen zwischendurch habe ich so viel gelernt.

Meinen Eltern Susanne und Ferdinand danke ich für die stetige Unterstützung. Ohne euch wären mein Studium und auch diese Promotion nicht möglich gewesen. Vielen Dank, dass ihr immer ein offenes Ohr für mich habt. Liebe Franziska, auch du bist immer da, hörst mir zu und hilfst mir so viel, dankeschön!

Meinem Mann Fabian und meinem Sohn Vincent danke ich dafür, dass sie für mich da sind und mein Leben so viel reicher machen. Ihr zeigt mir was wirklich wichtig ist und macht mich glücklich.

„Das Schönste, was wir erleben können, ist das Geheimnisvolle“

(Albert Einstein)

Scientific Contributions

Publications in Peer Reviewed Journals

Paul K, Graessl A, Rieger J, Lysiak D, Huelnhagen T, Winter L, Heidemann R, Lindner T, Hadlich S, Zimpfer A, Pohlmann A, Krüger P-C, Langner S, Stachs O, Niendorf T. Diffusion Sensitized Ophthalmic MRI Free of Geometric Distortion at 3.0 T and 7.0 T: A Feasibility Study in Healthy Subjects and Patients with Intraocular Masses. *Invest Radiol* 2015, E-pub ahead of print, doi: 10.1097/RLI.0000000000000129.

Oezerdem C, Winter L, Graessl A, **Paul K**, Els A, Weinberger O, Rieger J, Dieringer M, Hezel F, Voit D, Frahm J, Niendorf T. 16 Channel Bow Tie Antenna Transceiver Coil Array for Cardiac Magnetic Resonance at 7.0 T. *Magn Reson Med* 2015; accepted for publication.

Niendorf T, **Paul K**, Graessl A, Els A, Pohlmann A, Rieger J, Lindner T, Krüger P-C, Hadlich S, Langner S, Stachs O. Ophthalmic Imaging with Ultrahigh Field Magnetic Resonance Tomography. *Klinische Monatsblätter für Augenheilkunde* 2014; 231:1187-1195.Ma

Niendorf T, **Paul K**, Oezerdem C, Graessl A, Klix S, Huelnhagen T, Rieger J, Waiczies H, Oberacker E, Winter L. W(h)ither Cardiac and Body Ultrahigh Field Magnetic Resonance. *NMR Biomed* 2015, E-pub ahead of print, doi: 10.1002/nbm.3268.

Klix S, Els A, **Paul K**, Graessl A, Oezerdem C, Kraus O, Winter L, Thalhammer C, Huelnhagen T, Rieger J, Mehling H, Schulz-Menger J, Niendorf T. On the Subjective Acceptance during Cardiac Magnetic Resonance Imaging at 7.0 Tesla. *PLoS ONE* 2015; 10: e0117095.

Klix S, Hezel F, **Fuchs K**, Ruff J, Dieringer MA, Niendorf T. Accelerated Fast Spin-Echo Magnetic Resonance Imaging of the Heart Using a Self-Calibrated Split-Echo Approach. *PLoS ONE* 2014; 9:e94654.

Fuchs K, Hezel F, Klix S, Mekle R, Wuerfel J, Niendorf T. Simultaneous dual contrast weighting using double echo rapid acquisition with relaxation enhancement (RARE) imaging. *Magn Reson Med* 2014; 72:1590-1598.

von Knobelsdorff-Brenkenhoff F, Dieringer MA, **Fuchs K**, Hezel F, Niendorf T, Schulz-Menger J. Isometric handgrip exercise during cardiovascular magnetic resonance imaging: Set-up and cardiovascular effects. *J Magn Reson Imaging* 2013; 37:1342-1350.

Niendorf T, Graessl A, Thalhammer C, Dieringer MA, Kraus O, Santoro D, **Fuchs K**, Hezel F, Waiczies S, Ittermann B, Winter L. Progress and promises of human cardiac magnetic resonance at ultrahigh fields: a physics perspective. *J Magn Reson* 2013; 229:208-222.

Frauenrath T, **Fuchs K**, Dieringer MA, Ozerdem C, Patel N, Renz W, Greiser A, Elgeti T, Niendorf T. Detailing the use of magnetohydrodynamic effects for synchronization of MRI with the cardiac cycle: a feasibility study. *J Magn Reson Imaging* 2012; 36:364-372.

Publications in Peer Reviewed Conference Proceedings (1st Author)

Paul K, Graessl A, Rieger J, Lysiak D, Huelnhagen T, Winter L, Heidemann R, Lindner T, Hadlich S, Pohlmann A, Krüger P-C, Langner S, Stachs O, Niendorf T. Diffusion-sensitized Ophthalmic MRI Free of Geometric Distortion in Patients with Intraocular Masses. *23rd Annual Meeting of the International Society of Magnetic Resonance in Medicine (ISMRM)*, 2015, Toronto, Canada. (Electronic Poster)

Paul K, Graessl A, Rieger J, Lysiak D, Huelnhagen T, Winter L, Heidemann R, Lindner T, Hadlich S, Krüger P-C, Langner S, Stachs O, Niendorf T. Towards High Spatial Resolution Diffusion-sensitized MR Imaging of the Eye and Orbit at 3.0 T and 7.0 T: Quantitative Assessment of the Anatomic Fidelity of EPI and RARE Variants. *23rd Annual Meeting of the International Society of Magnetic Resonance in Medicine (ISMRM)*, 2015, Toronto, Canada. (Electronic Poster)

Paul K, Graessl A, Rieger J, Lysiak D, Huelnhagen T, Winter L, Els A, Endemann B, Lindner T, Hadlich S, Krüger P-C, Langner S, Stachs O, Niendorf T. In vivo MR Microscopy of the Nervus Opticus at 3.0 T and 7.0 T: Anatomical and Diffusion Weighted Imaging in Healthy Subjects and Patients with Optic Nerve Glioma. *23rd Annual Meeting of the International Society of Magnetic Resonance in Medicine (ISMRM)*, 2015, Toronto, Canada. (Oral presentation plus Electronic Poster)

Fuchs K, Hezel F, Klix S, Mekle R, Wuerfel J, Niendorf T. On the application of simultaneous dual contrast weighting using double echo 2in1-RARE in healthy subjects and multiple sclerosis patients. *22nd Annual Meeting of the International Society of Magnetic Resonance in Medicine (ISMRM)*, 2014, Milan, Italy. (Poster)

Fuchs K, Hezel F, Oezerdem C, Winter L, Niendorf T. Myocardial T_2^* mapping free of distortion using susceptibility weighted RARE imaging at 7 Tesla. *22nd Annual Meeting of the International Society of Magnetic Resonance in Medicine (ISMRM)*, 2014, Milan, Italy. (Poster)

Fuchs K, Graessl A, Rieger J, Niendorf T. Diffusion sensitized ophthalmic MRI free of distortion using multi-shot DWI-RARE at 3 T and 7 T. *22nd Annual Meeting of the International Society of Magnetic Resonance in Medicine (ISMRM)*, 2014, Milan, Italy. (Oral presentation)

Fuchs K, Hezel F, Klix S, Niendorf T. 2-in-1: Simultaneously T_2/T_2^* Weighted Double Echo Fast Spin Echo Imaging. *21st Annual Meeting of the International Society of Magnetic Resonance in Medicine (ISMRM)*, 2013, Salt Lake City, Utah, USA. (Oral presentation)

Fuchs K, Hezel F, Winter L, Oezerdem C, Graessl A, Dieringer M, Kraus O, Niendorf T. Feasibility of Cardiac Fast Spin Echo Imaging at 7.0 T Using a Two-Dimensional 16 Channel Array of Bowtie Transceivers. *21st Annual Meeting of the International Society of Magnetic Resonance in Medicine (ISMRM)*, 2013, Salt Lake City, Utah, USA. (Poster)

Fuchs K, Hezel F, Deimling M, Ruff J, Niendorf T. Diffusion weighted turbo spin echo sequence for cardiac imaging. *3rd Annual Scientific Symposium, Ultrahigh Field Magnetic Resonance: Clinical Needs, Research Promises and Technical Solutions*, 2012, Berlin, Germany. (Poster)

Fuchs K, Frauenrath T, Dieringer M, Patel N, Özerdem C, Hentschel J, Renz W, Niendorf T. Der magnetohydrodynamische Effekt als Synchronisierungsmethode für die kardiovaskuläre MRT bei 3.0 T und 7.0 T. *14th Annual Meeting of the German Chapter of the ISMRM*, 2011, Berlin, Germany. (Poster)

Fuchs K, Frauenrath T, von Knobelsdorff-Brenkenhoff F, Schulz-Menger J, Niendorf T. Acoustic cardiac triggering for cardiovascular magnetic resonance imaging in patients with pathologically changed heart sounds. *Joint MDC-FMP PhD Retreat*, 2011, Bad Liebenwalde, Germany. (Poster)

Patent Applications

Fuchs K, Hezel F, Klix S, Niendorf T. Verfahren für simultanes Erzeugen von unterschiedlichen Kontrasten mittels schneller Spin-Echo MR Bildgebung. Patent application 102013005612.8, German Patent Office (2013)

Publications in Peer Reviewed Conference Proceedings (Co-Author)

Huelnhagen T, **Paul K**, Graessl A, Rieger J, Lysiak D, Prothmann M, Schulz-Menger J, Niendorf T. Towards clinical caridac MR at 7.0 T: Early Experience with black blood RARE imaging in patients

with hypertrophic cardiomyopathy. *23rd Annual Meeting of the International Society of Magnetic Resonance in Medicine (ISMRM)*, 2015, Toronto, Canada.

Klix S, Els A, **Paul K**, Graessl A, Oezerdem C, Kraus O, Winter L, Thalhammer C, Huelnhagen T, Rieger J, Mehling H, Schulz-Menger J, Niendorf T. On the Subjective Acceptance during Cardiac Magnetic Resonance Imaging at 7.0 Tesla. *23rd Annual Meeting of the International Society of Magnetic Resonance in Medicine (ISMRM)*, 2015, Toronto, Canada.

Özerdem C, Winter L, Graessl A, **Paul K**, Els A, Voit D, Frahm J, Niendorf T. Real-time imaging of the heart and aorta at 7.0 T using a 16 channel bow tie antenna transceiver array. *23rd Annual Meeting of the International Society of Magnetic Resonance in Medicine (ISMRM)*, 2015, Toronto, Canada.

Özerdem C, Winter L, Graessl A, **Paul K**, Els A, Niendorf T. Sub-millimeter in-plane spatial resolution CINE imaging of the heart at 7.0 T using a 16 channel bow tie antenna transceiver coil array. *23rd Annual Meeting of the International Society of Magnetic Resonance in Medicine (ISMRM)*, 2015, Toronto, Canada.

Özerdem C, Winter L, **Fuchs K**, Niendorf T. Towards Ultimate SNR: Combination of a Multi-Element TX/RX Dipole Antenna Array with Nested and Meander Shaped RX Dipole Antenna at 7.0 Tesla. *4th Annual Scientific Symposium, Ultrahigh Field Magnetic Resonance: Clinical Needs, Research Promises and Technical Solutions*, 2013, Berlin, Germany.

Graessl A, Winter L, Özerdem C, Hezel F, **Fuchs K**, Pfeiffer H, Hoffmann W, Niendorf T. A Two-dimensional 16 Channel Dipole Transceiver Array for Cardiac MR at 7.0T: Design, Evaluation of RF Shimming Behavior and Application in CINE Imaging. *4th Annual Scientific Symposium, Ultrahigh Field Magnetic Resonance: Clinical Needs, Research Promises and Technical Solutions*, 2013, Berlin, Germany.

Dieringer M, Deimling M, **Fuchs K**, Winter L, Kraus O, von Knobelsdorff Brenkenhoff F, Schulz-Menger J, Niendorf T, Blood/myocardium contrast-to-noise ratio for cardiac morphology and function imaging increases with field strength. *11th International Congress on Cardiovascular Magnetic Resonance (EuroCMR Florenz)*, 2013, Florenz, Italy.

Hezel F, Kellman P, **Fuchs K**, Winter L, Kraus O, Niendorf T. Towards Myocardial T2* Mapping at 7.0 T: Assessment and Implications of Static Magnetic Fields Variations. *21st Annual Meeting of the International Society of Magnetic Resonance in Medicine (ISMRM)*, 2013, Salt Lake City, Utah, USA.

Hezel F, Kellman P, **Fuchs K**, Winter L, Kraus O, Niendorf T. Coronary MR Angiography at 7.0 Tesla Using 3D Fat-Water Separated Imaging and an 8 Channel Cardiac Array of Bowtie Dipole

Transceivers. *21st Annual Meeting of the International Society of Magnetic Resonance in Medicine (ISMRM)*, 2013, Salt Lake City, Utah, USA.

Oezerdem C, Winter L, **Fuchs K**, Niendorf T. Towards Ultimate SNR: Combination of a Multi-Element TX/RX Dipole Antenna Array with Nested and Meander Shaped RX Dipole Antenna at 7.0 Tesla. *21st Annual Meeting of the International Society of Magnetic Resonance in Medicine (ISMRM)*, 2013, Salt Lake City, Utah, USA.

Tovar E, **Fuchs K**, Hezel F, Dieringer M, Wuerfel J, Niendorf T. Assessment of multiple sclerosis at 7.0 T using high spatial resolution, fluid attenuated inversion recovery prepared susceptibility weighted fast spin echo imaging. *21st Annual Meeting of the International Society of Magnetic Resonance in Medicine (ISMRM)*, 2013, Salt Lake City, Utah, USA.

Dieringer M, Deimling M, **Fuchs K**, Winter L, Kraus O, von Knobelsdorff-Brenkenhoff F, Schulz-Menger J, Niendorf T. Blood/myocardium contrast-to-noise ratio for cardiac morphology and function imaging increases with field strength. *21st Annual Meeting of the International Society of Magnetic Resonance in Medicine (ISMRM)*, 2013, Salt Lake City, Utah, USA.

Tovar E, Hezel K, **Fuchs K**, Wuerfel J, Paul F, Sobesky J, Niendorf T. High spatial resolution susceptibility weighted fast spin echo brain imaging at 3.0 T and 7.0 T. *20th Annual Meeting of the International Society of Magnetic Resonance in Medicine (ISMRM)*, 2012, Melbourne, Australia.

Frauenrath T, **Fuchs K**, Hezel F, Dieringer M, Rieger J, Niendorf T. Improved Cardiac Triggering by Combining Multiple Physiological Signals: A Cardiac MR Feasibility Study at 7.0 T. *20th Annual Meeting of the International Society of Magnetic Resonance in Medicine (ISMRM)*, 2012, Melbourne, Australia.

von Knobelsdorff-Brenkenhoff F, Dieringer M, **Fuchs K**, Hezel F, Renz W, Niendorf T, Schulz-Menger J. Physiological stress during cardiovascular magnetic resonance – handgrip exercise induced hemodynamic effects. *15th Annual SCMR Scientific Sessions*, 2012, Orlando, Florida, USA.

Invited Talks

Whither Ophthalmic MR: Technical Advances and Emerging Cinical Applications of Imaging the Eye, the Orbit and the Optical Nerve at 7.0 T. 6th *Annual Scientific Symposium on Ultrahigh Field Magnetic Resonance: Clinical Needs, Research Promises and Technical Solutions*, 2015, Berlin, Germany.

Speed Saves: Advances in Rapid Acquisition with Relaxation Enhancement (RARE) Imaging - Methodology and Clinical Applications. *5th Annual Scientific Symposium on Ultrahigh Field Magnetic Resonance: Clinical Needs, Research Promises and Technical Solutions*, 2014, Berlin, Germany.

Artifact Identification & Elimination Game Show. *Joint Annual Meeting ISMRM-ESMRMB 2014*, 2014, Milan, Italy.

Artifact Identification & Elimination Game Show. *ISMRM 21st Annual Meeting & Exhibition*, 2013, Salt Lake City, Utah, USA.

Alternative Cardiac Gating/Triggering Techniques for High Field CMR. SCMR/ISMRM Jointly Sponsored Workshop on New Horizons in High Field Cardiovascular MR: Promises and Progress, 2013, San Francisco, California, USA.

Magnetohydrodynamischer (MHD) Effekt in der MRT. *48. Arbeitskreissitzung, Arbeitskreis Magnetresonanzverfahren der deutschen Gesellschaft für Medizinische Physik e.V. (DGMP)*, 2011, Berlin, Germany.